NASA Contractor Report 3241

Thermal Elastohydrodynamic Lubrication of Spur Gears

K. L. Wang and H. S. Cheng

NASA

NASA Contractor Report 3241

Thermal Elastohydrodynamic Lubrication of Spur Gears

K. L. Wang and H. S. Cheng
Northwestern University
Evanston, Illinois

NASA

National Aeronautics
and Space Administration

**Scientific and Technical
Information Office**

1980

TABLE OF CONTENTS

I. INTRODUCTION

1.1. Description of the Problem

For several decades, gears have been known to be the simplest and most efficient mechanical component in transmitting power. Yet, the basic mechanisms which govern the major failure modes in gears, particularly those of lubrication origin, are not satisfactorily understood. In industrial applications,long life in gears is usually attained by overdesign at the sacrifice of cost, material, and compactness. However, in aerospace or military applications, where the weight is at a premium, gears are often designed under conditions very close to the failure limits with considerable uncertain life expectations. From the standpoint of material conservation and mechanical reliability, a better understanding in gear lubrication, particularly in the light of recent developments in elastohydrodynamic lubrication, is badly needed.

Gear failure can be generally classified into structural failures, which include case crushing, flexure fatigue, and tooth breakage, and lubrication failures which include abrasive or corrosive wear, surface pitting, and scuffing (or scoring).

Structural failures are usually attributed to poor material, improper design or unexpected overloading. These failures are not directly related to lubrication and can be circumvented by better geometrical design and improved material selections.

Since the basic lubrication process between gear teeth is not fully understood, the lubrication failures, in particular surface pitting and scuffing, are much more difficult to predict and to prevent. There is a general consensus that current gear design practice against lubrication failures, based mainly on empiricism, is not satisfactory. Any improvements

in design criteria against surface pitting and scuffing must depend on a more thorough understanding of the film thickness and surface temperature in the gear teeth contact because it has been shown in failure tests with rollers that both failure modes are influenced critically by these two quantities.

The present research is concerned mainly with developing a comprehensive analysis in predicting the mean film thickness and the surface temperature in spur gear teeth contacts under given dynamic loads. The analysis also includes, in the first part, a new procedure for determining the dynamic load between gear teeth contacts having a contact ratio greater than unity, and considering a variable stiffness along the line of action. The analysis of transient film thickness and temperature along the line of action is based on the most recent theories on film thickness and traction in elastohydrodynamic contacts.

1.2. Previous Study

1.2.1. Dynamic Load

One of the main uncertainties in gear lubrication analysis is the load imposed on the gear teeth at high speeds where the inertia forces of the gear wheels become significant. Dynamic load in gears has received continuous attention in the past. Notable contributions in this area include Refs. 1 to 4.

More recent work was contributed by Attia (Ref. 5) and by Houser and Seireg (Ref. 6) in which the dynamic load variations for a pair of spur gears along the action line were analyzed and measured experimentally. However, their results were restricted to special sets of gear geometry under limited operating conditions, and, therefore, do not have a wide

applicability. Hirano (Ref. 7), and Ishihawa et al (Ref. 8)
developed analytical models based on the torsional vibrations of two
gear wheels, and obtained results which agree well with dynamic loads
measured with strain gages at the root of a gear tooth. The close
agreement in Refs. 7 and 8 suggests that their analytical approach
can be refined to give an accurate method in determining the dynamic
loads for the present lubrication analysis.

1.2.2. Film Thickness

Papers concerning the lubricant film thickness in gear teeth can be
dated as early as 1916 (Ref. 9) when the lubricant film thickness
estimated by representing the gear teeth contacts with equivalent con-
tacts between two rigid cylinders. Using the same approach, McEween (Ref.
10),in 1952, developed an analysis for the lubricant film between gears
including both the sliding and rolling motion of contacting surfaces.
The results of these analyses have served to inspire further activities
in gear lubrication. However, they failed to yield an accurate model
for prediction of the film thickness because factors such as the elastic
deformation of the surface, pressure and temperature viscosity dependence,
thermal effects from the heat generated in the contact, as well as the
squeeze film effect along the line of action were all disregarded in
the analysis.

In searching for a better approximation, Redzimovsky and his co-
workers (Refs. 11 and 12) have used actual gear tooth profiles and
motions to solve for the lubricant film thickness variation governed by
the time-dependent Reynolds Equation. However, their papers suffer from
the drawback of neglecting the effects of surface deformation and the

3

pressure and temperature dependent viscosity of the lubricant. In a more recent paper (Ref. 13), they have included the effect of elastic deformation in the model, but still ignored the important effect of variable viscosity at high pressures. These assumptions seem to limit the application of their analyses to a fairly narrow range of lightly loaded gears.

In 1965, Dowson, and Higginson (Ref. 14) applied their isothermal elastohydrodynamic lubrication theory and developed design charts to predict the film thickness between gear teeth contacts at the pitch point. Their procedures remain to date as the best method in estimating the lubricant film thickness in spur gears, provided the bulk surface temperatures of the gear teeth are known before hand. Later, Gu (Ref. 15) extended Dowson and Higginson's approach to determine the film thickness variation along the entire line of action. However, Gu's analyses still assumes that the bulk surface temperature is known, and also ignores the squeeze film effect.

1.2.3. Flash Temperature

The surface temperature increase (or flash temperature) within a sliding Hertzian contact is a topic which has been extensively investigated in the past (Refs. 16 to 18). The first successful prediction of flash temperature was due to Blok (Ref. 16) based on the heat conduction analysis in a semi-infinite body with a uniformly distributed moving heat source.

A refined solution, which includes a local, heat partition function between a pair of disks, was derived by Cameron et al (Ref. 19). More recently Francis (Ref. 20) made a further refinement in Blok's calculation by considering a variable heat flux in the contact.

4

The above simplified analyses yield a reasonably accurate prediction of the flash temperature which can be summed together with the bulk surface temperature to yield the total temperature in the contact. It appears that the uncertainties of predictions of the failure related total temperatures are not due to any inaccuracies of the flash temperature analyses but rather due to the lack of reliable information on the bulk surface temperature and the local coefficient of friction in the contact. Thus, the gear lubrication is really a system problem which requires an iterative scheme solving for the bulk surface temperature, flash temperature, and heat flux simultaneously.

1.2.4. Failure Experiments

Past failure experiments in gears are primarily involved with finding the scuffing loads as a function of speed. Among these, the most intriguing one is the series of tests performed by Borsoff (Ref. 21). As the speed increases initially in the low speed range, the scuffing load shows a decreasing trend which confirms the previous results on gear scuffing tests. As the speed further increases, the trend reverses itself, and the scuffing load tends to rise with speed. This intrigue trend in the high speed region has not been observed in previous gear tests, and has not been explained satisfactorily by any theory. In a later experiment, Ku and Baber (Ref. 22) conducted a series of tests with a modified Ryder Gear Tester and was able to obtain a similar trend observed by Borsoff. However, the increase in scuffing load in the high speed range is much less pronounced than that found by Borsoff.

Gear experiments directly related to surface pitting are quite scanty. The effect of lubricant properties on surface pitting in gears was investigated by Neiman, G., Rettig, H., and Batsch, H., (Ref. 23).

5

More recently, the effects of material properties and tip relief were studied by Townsend and Zaretsky (Ref. 24). The effects of lubricant film thickness as well as the surface temperature on surface pitting have not been examined directly by pitting experiments.

1.3. Present Study

In the present study, the combined effects of gear kinematics, dynamics, frictional heating as well as the elastohydrodynamics on the lubrication performance between gear teeth is systematically treated.

In Chapter II, descriptions are first given to the involute geometry and the definition of coordinate systems used in this work, and then to the qualitative aspects of gear dynamics, film thickness and thermal reactions for a pair of spur gears in operation.

In Chapter III, the kinematic relations and the coordinates used in the analyses are described. They are followed by the analysis of the dynamics of two meshing gears and a numerical method for predicting the dynamic load.

Chapter IV, deals with the solution of time-dependent isothermal elastohydrodynamic film thickness along the line of action using the time-dependent Reynolds equation in which the squeeze-film effect due to the change of dynamic load, contact radii and velocity are all considered.

A rheology model proposed by Dyson (Ref. 25) based on the concept of limiting shear stress is used in Chapter V for the traction analysis. The heat generation due to viscous shear and the instantaneous temperature rise caused by solid-fluid interaction are analyzed.

In Chapter VI, the finite element method is used to develop an algorithm for predicting the equilibrium surface temperature distribution along the tooth profiles of meshing gears.

The entire numerical iterative procedures for the interdependent film thickness, and the flash temperature are described in Chapter VII. Results in terms of dynamic load, film thickness, and flash temperature for various dimensionless design parameters are presented in Chapter VIII.

II. PROBLEM FORMULATION

2.1. Spur Gear Geometry

The basic geometry of involute spur gears is briefly reviewed here in order to provide the necessary background to formulate the gear lubrication analysis.

Figure 2.1 shows the geometry of a pair of involute gears in contact at the pitch point 0. The lower gear is the driving member commonly known as the pinion and the upper driven member is referred to as the gear. R_1 and R_2 are the pitch radii of the pinion and the gear. Through the pitch point 0 and tangent to two base circles a_1, a_2, one may draw a straight line inclined at an angle ϕ to the common tangent of the pitch circles. ϕ is known as the pressure angle because the force is acting at an angle ϕ inclined to the common tangent.

The involute tooth profile of the pinion can be obtained by tracing the location of 0 while a taut string $a_1 0$ is being unwrapped around the pinion base circle. The gear tooth profile can be obtained in the same manner. It can be readily demonstrated that during the engagement of the teeth, the point of contact always lies on the line $a_1 a_2$, which is known as the line of action. The engagement begins at b_1, where $a_1 a_2$ intersects with the outer radius R_{o2} of the gear, and ends at b_4, where $a_1 a_2$ intersects with R_{o1}. The depth of tooth beyond the pitch point, $R_{o1} - R_1$, is known as the addendum, and below the pitch point, $R_1 - R_{r1}$ is called the deddendum. The addendum and deddendum are inversely proportional to the diametrical pitch D_p, which is defined as the number of teeth per inch of diameter.
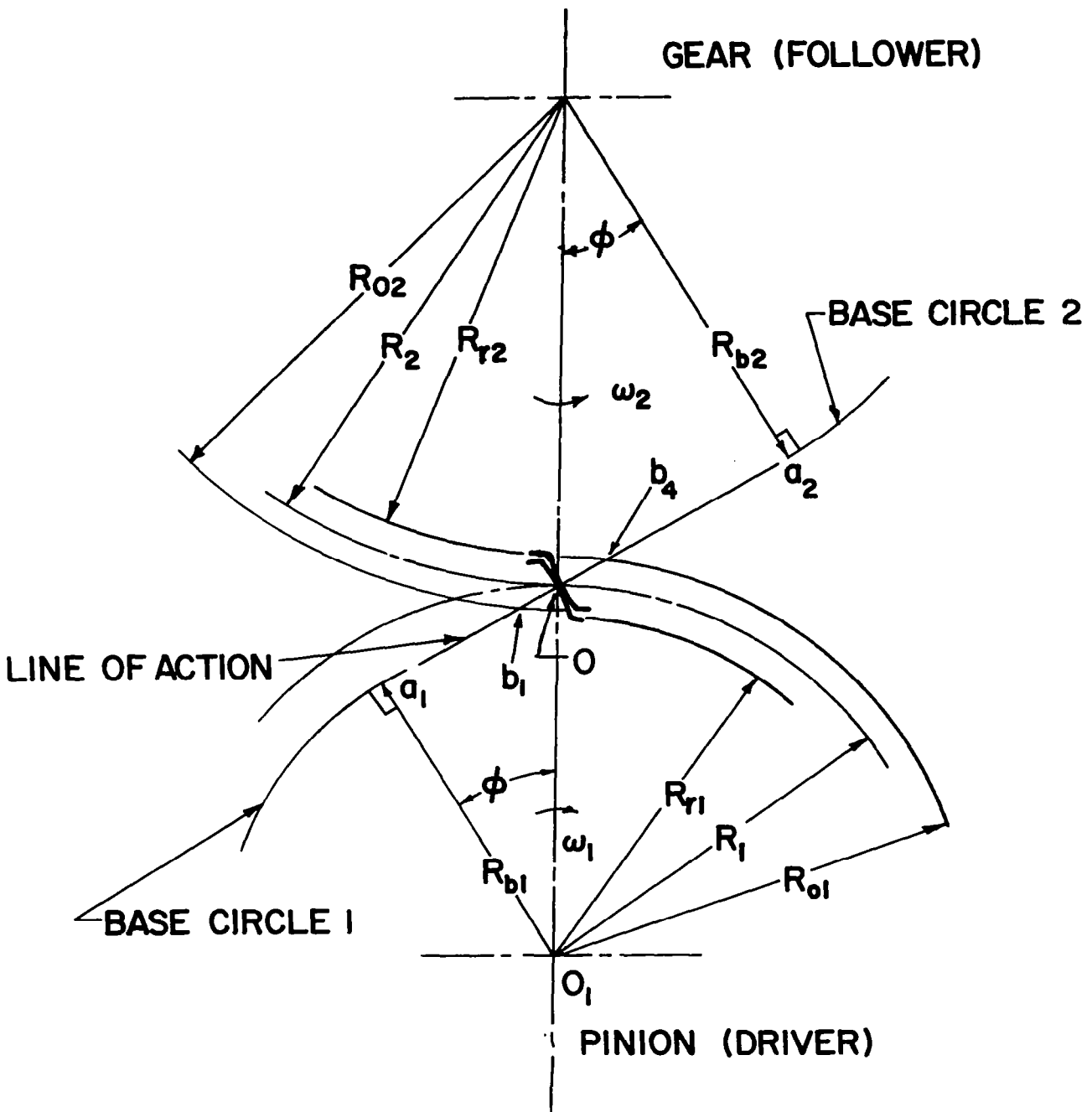
Fig. 2.1.   Geometry of Spur Gears

2.2. Coordinate Systems

Since the nature of each individual analysis in the present study is different it is difficult to employ a single coordinate throughout the entire formulation. The analytical efforts are much reduced if the following two separate coordinates are introduced.

The first set of coordinates, shown as X, Y, and Z in Fig. 2.2, is a set of fixed Cartesian coordinates with its origin at the pitch point and the X-axis along the path of contact. The coordinate X is the distance between the contact point and the pitch point. The teeth are engaging when X is negative, and disengaging when it is positive. In the analyses, the dynamic load, transient film thickness, and flash temperature are all expressed as functions of X instead of functions of time.

The second set of coordinates, shown as x, y, z, in Fig. 2.2, is fixed to one of the gears with its origin at the gear center. The y-axis extends radially along the center line of a typical tooth, the z-axis is parallel to the shaft, and the x-axis is perpendicular to both. This set of axes is used in analyzing the bulk surface temperature of the gears.

2.3. System Characteristics

As stated earlier, the main objectives in this study are to determine the dynamic load, lubricant film thickness, and the flash temperature along the line of action between two meshing gear teeth. Before the details of each analysis is presented, it is desirable to study the qualitative features of each of the above variables.
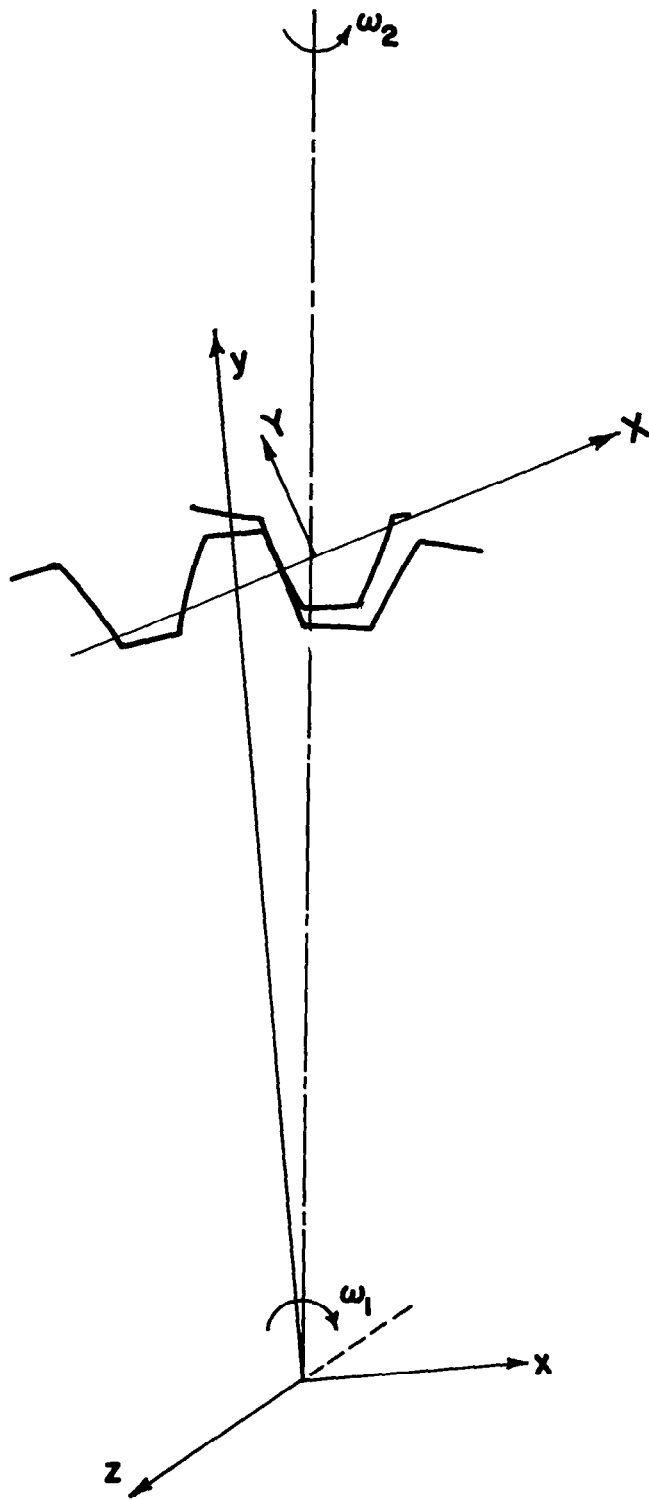
Fig. 2.2.   Coordinate Systems

11

2.3.1. Dynamic Load

When more than one pair of teeth is in contact, the load is shared among the pairs. Figure 2.3a illustrates the load sharing characteristics between two pairs of teeth in contact. Along the line of action, the contact points of two pairs of teeth are always spaced at a distance equal to $\cos \phi$ times the circular pitch or known as the base pitch. As pair 2 begins to contact at b_1, it shares a load less than half of the total load with the preceeding pair 1. Since at this instant the combined stiffness of pair 1 is much greater than the stiffness of pair 2, pair 1 takes a larger share of the total load. As the contact point of pair 2 moves to b_2, pair 1 is out of the contact at b_4 and the entire load is transferred to pair 2. As pair 2 reaches b_3, a new pair begins to contact at b_1 and the load is again shared between two pairs.

Figure 2.3b shows qualitatively a variation of load for a pair of teeth as a function of the coordinate along the line of action. This is a static load variation because the inertia forces of the gear wheels are ignored. If these inertia forces are included, the load variation then includes additional oscillations superimposed on the static load curve. The frequency and amplitude of these oscillations would depend on the speed and the error profile, i.e. the deviation of the tooth profile from the true involute profile. A typical variation of the dynamic load variation is also shown in Fig. 2.3b.

The mathematical modelling of the statically indeterminate system including two pairs of gear teeth and the inertia of the gears along with a numerical solution of the governing equation for the dynamic load is the main topic in Chapter III.
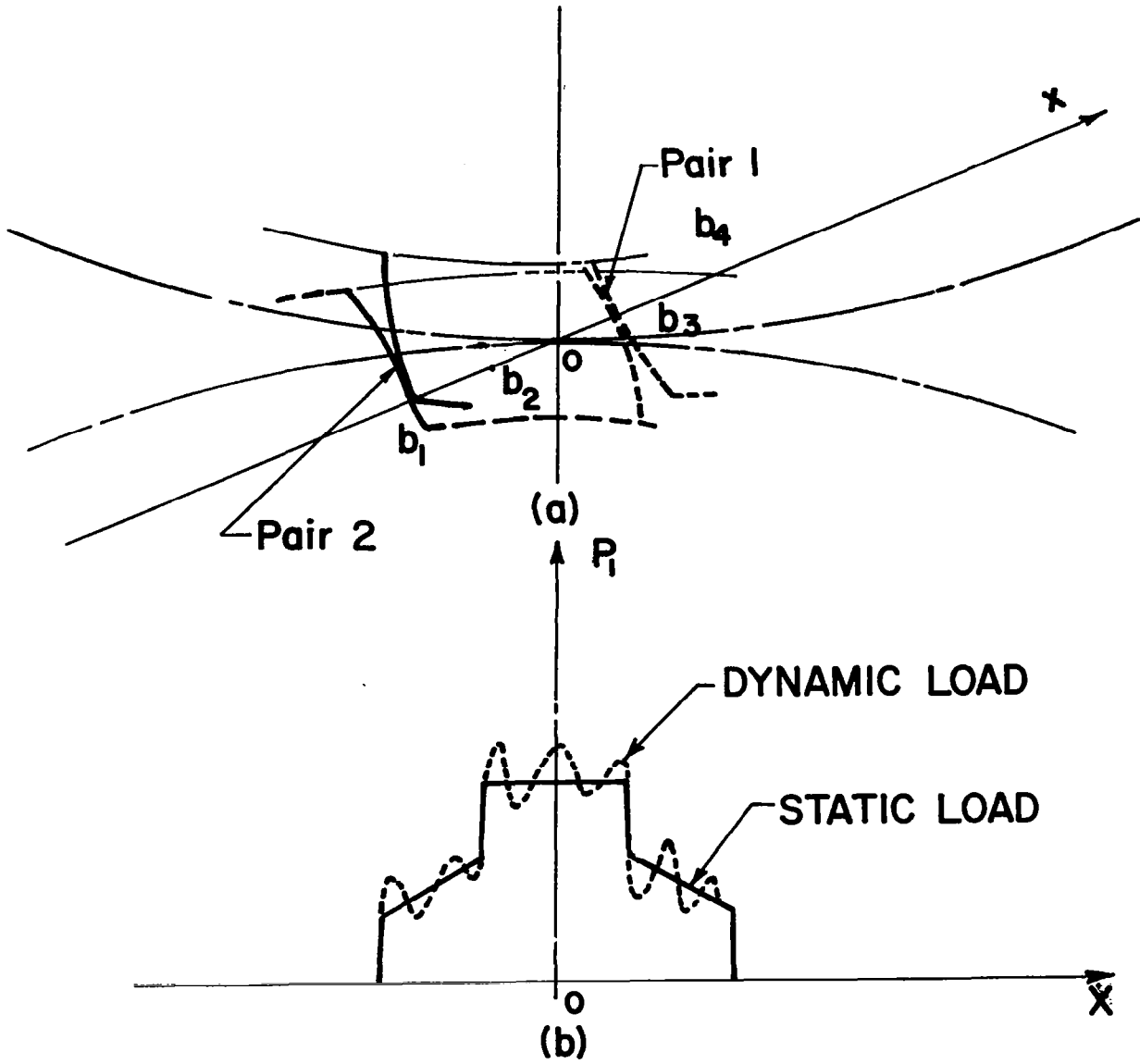
Fig. 2.3(a&b)   Load Sharing Characteristics

2.3.2. Film Thickness

The film thickness between gear teeth at any point along the line of action can be predicted from the existing theories of elastohydrodynamic lubrication provided the local rolling velocity, maximum Hertzian contact stress, relative radius, and the local viscosity corresponding to the local surface temperature at that point are known. With these known quantities, the film thickness can be estimated from the following general formula

$$h = C(\alpha E')^{n_1} \left(\frac{\mu_o u}{E'R}\right)^{n_2} \left(\frac{p_{Hz}}{E'}\right)^{n_3} \tag{2.1}$$

where

α = pressure viscosity coefficient

μ_o = viscosity at the inlet of the contact. μ_o is a function of the local equilibrium surface temperature[*]

u = rolling velocity

R = relative radius

p_{Hz} = maximum Hertzian contact pressure

c, n_1, n_2, n_3 = constant or exponents derived from various EHD theories

E' = Equivalent Youngs modulus.

It is important to note that μ_o, u, R, and p_{Hz} all vary along the line of action. u and R depend only on the kinematics, and can be readily derived. p_{Hz} depends strictly on the dynamic load which is determined from the analysis in Chapter III. μ_o is strongly dependent upon the local static surface temperature which is in turn influenced by the local film thickness through the frictional heating. Thus, the film thickness and static surface temperature are mutually dependent, and are

---

[*]the definition of equilibrium surface temperature is given in section 2.3.3.

14

solved as a coupled system in the present work. However, the dynamic load is assumed not to be influenced by h or μ_o, and therefore, is solved separately.

It should be noted that predictions of h using Eq. (2.1) ignore the squeeze-film effect due to the rapid change of h along the line of action. To include this effect, one must include the term $\partial h/\partial t$ in the Reynolds equation. In Chapter IV, the extension of present EHD theories to include the transient effects for gears is accomplished based on a recent analysis by Vichard (Ref. 26).

2.3.3. Equilibrium Surface Temperature

When a pair of gears is running under a given load, the time-averaged surface temperature over one revolution at any point on the facing of a tooth gradually increases and finally reaches an equilibrium value after many revolutions. This steady state, time-independent temperature distribution is referred to as the equilibrium surface temperature, which directly governs the lubricant film thickness and the maximum surface temperature within the Hertzian contact. Figure 2.4 shows typical variations of the equilibrium temperature along the profiles of a pair of engaging teeth. These curves can be calculated by a finite element numerical method for the steady-state heat conduction analysis within a typical wedge of a gear wheel. The details of this analysis for the equilibrium temperature distribution are described in Chapter VI.

2.3.4. Flash Temperature

As discussed in Chapter I, the flash temperature is the increment in temperature above the equilibrium surface temperature within the Hertzian
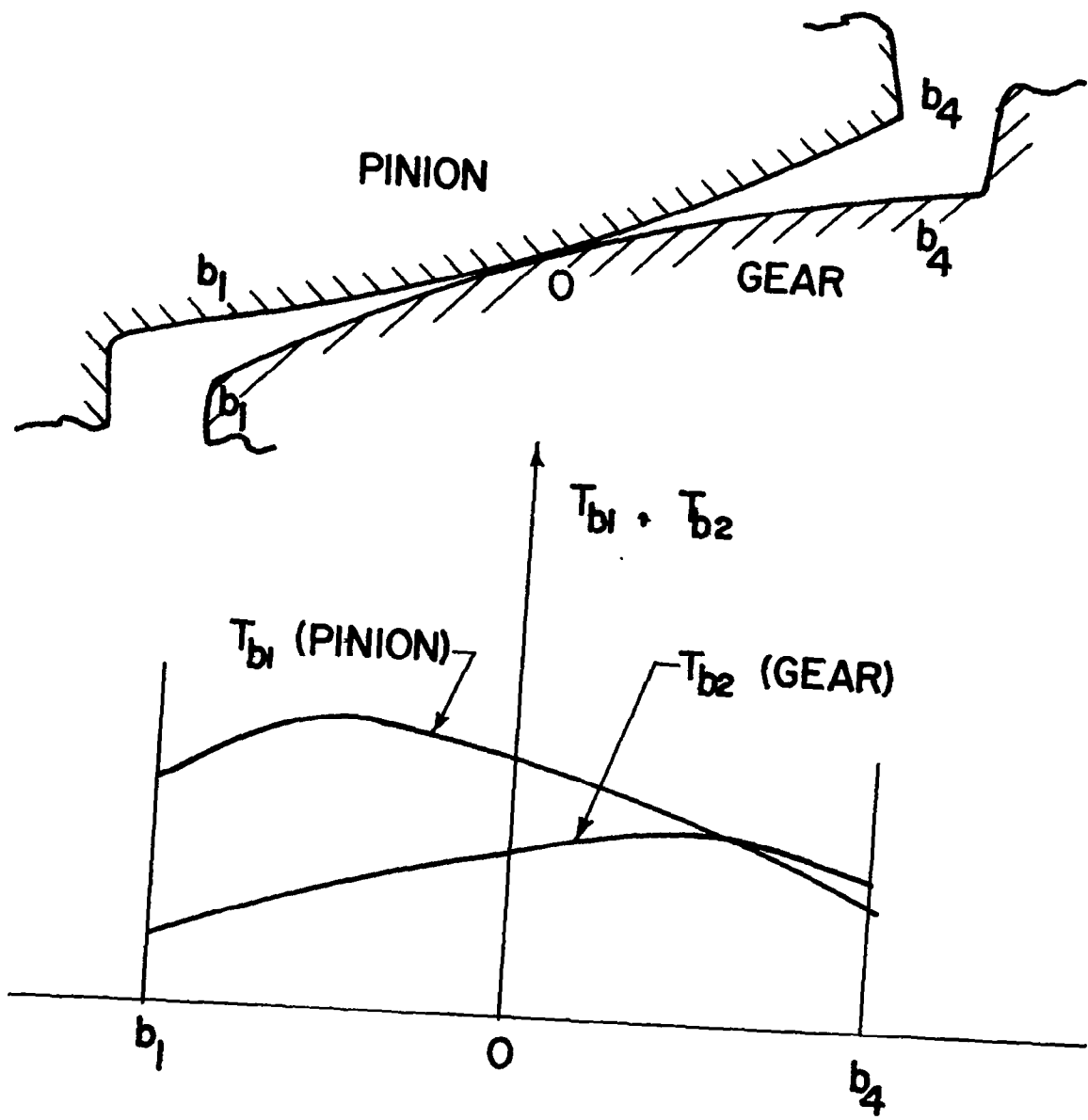
Fig. 2.4.   Characteristics of Equilibrium Surface Temperature

contact due to the sliding frictional heating. The rising or decaying
rate of this flash temperature is a function of speed and material
properties of the solids. For steel gears operating at even fairly
slow speeds, the decaying rate at any contacting point is still very
rapid so that it only takes a very small fraction of a full revolution
for the surface temperature to return to its static value. Figure 2.5
shows qualitatively the rise and decay of instantaneous surface profiles
for a pinion at various contacting points along the line of action.
The flash temperature is most pronounced at the root and tip where the
sliding speed is the highest.

The calculation of flash temperature is based on a simplified thermal
analysis of the lubricant film in the Hertzian contact, and on the Blok-
Jeager type analysis of surface temperature for a fast moving heat
source. Details of the flash temperature analysis are given in Chapter V.

2.3.5. System Solution

The solution to the spur gear system in question is accomplished
numerically in two parts. First, the dynamic load along the line of
action is assumed to be independent of the lubricant film thickness and
flash temperature, and it is determined by directly integrating the
equation of motion with the Runge-Kutta method. The dynamic load is
then used in the second part to determine the lubricant film thickness
and flash temperature iteratively based on the analyses given in
Chapters IV to VI. Details of the numerical procedures and block diagram
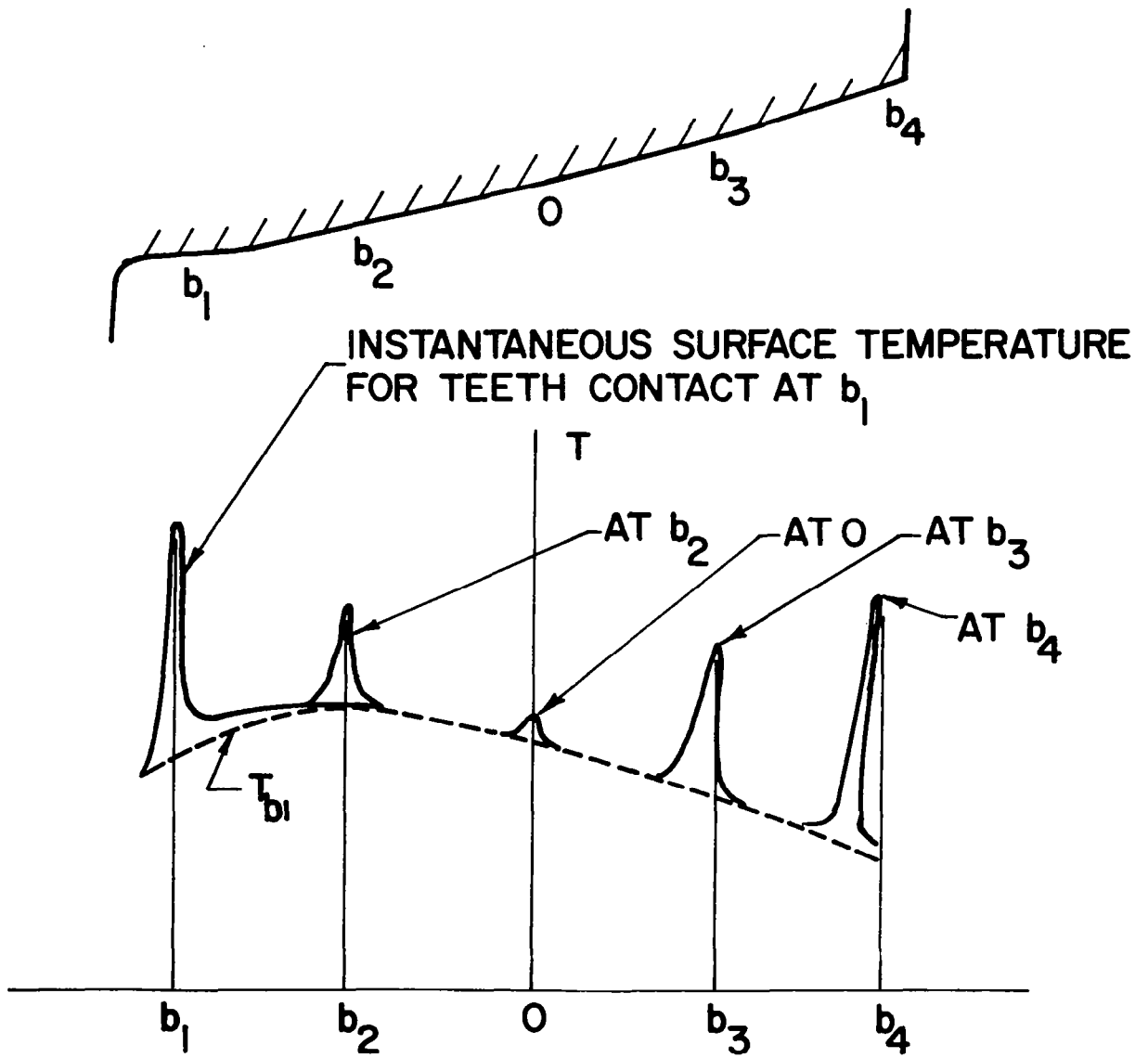for the computer program are given in Chapter VII.

17

Fig. 2.5.   Characteristics of Flash Temperature

18

III. DYNAMIC LOAD

3.1. Gear Kinematics

In order to develop the analysis of dynamic load and lubricant film thickness, it is necessary to use the kinematic relations for the local radius and the surface velocities as functions of X, the distance between the contact point and the pitch point, along the line of action. These relations were given by Gu (Ref. 15) as:

$$r_1 = R_{b_1} \tan \phi + X \tag{3.1}$$

$$r_2 = R_{b_2} \tan \phi - X \tag{3.2}$$

$$u_1 = V \left(\frac{X \cos \phi}{R_{b_1}} + \sin \phi \right) \tag{3.3}$$

$$u_2 = V \left(- \frac{X \cos \phi}{R_{b_2}} + \sin \phi \right) \tag{3.4}$$

From these, the relative radius becomes

$$
R(X) = \frac{r_1 r_2}{r_1 + r_2}
$$

$$
= \frac{\left(R_{b_1} \tan \phi + X \right)\left(R_{b_2} \tan \phi - X \right)}{\left(R_{b_1} + R_{b_2} \right) \tan \phi} \tag{3.5}
$$

The rolling and sliding velocities at the contact become

$$
u(X) = \frac{1}{2} \left(u_1 + u_2 \right)
$$

$$
= V \sin \phi + \frac{V \cos \phi}{2} \frac{\left(R_{b_2} - R_{b_1} \right) X}{R_{b_1} R_{b_2}} \tag{3.6}
$$

19

$$u_s(X) = u_1 - u_2$$

$$= V \cos \phi \left(\frac{R_{b_2} + R_{b_1}}{R_{b_1} R_{b_2}} \right) X \qquad (3.7)$$

The contact ratio C_r is a very useful quantity in spur gear kinematics and is defined as the length of contact along the line of action $b_1 b_2$ divided by the base pitch p_b. Most gears operate at a contact ratio between 1 and 2, i.e. the load is sometimes shared by a pair of gears during engagement. Referring to Fig. 2.1 , one may define the distance between the beginning of contact and the pitch point $b_1 0$ as the length of approach Z_a, and $b_4 0$ as the length of recess Z_r. From the geometry,

$$Z_a = \left(R_{o_2}^2 - R_{b_2}^2 \right)^{1/2} - R_2 \sin \phi \qquad (3.8)$$

$$Z_r = \left(R_{o_1}^2 - R_{b_1}^2 \right)^{1/2} - R_1 \sin \phi \qquad (3.9)$$

By definition of the contact ratio,

$$C_r = \frac{b_1 b_2}{p_b}$$

$$= \frac{Z_a + Z_r}{p_c \cos \phi} \qquad (3.10)$$

Typical variations of R, u, and u_s along the line of action are shown in Figs. 3.1 to 3.3.

3.2. Tooth Deflection

For most gear applications, the contact ratio is greater than one, that is, during the engagement there will be, at times, more than one
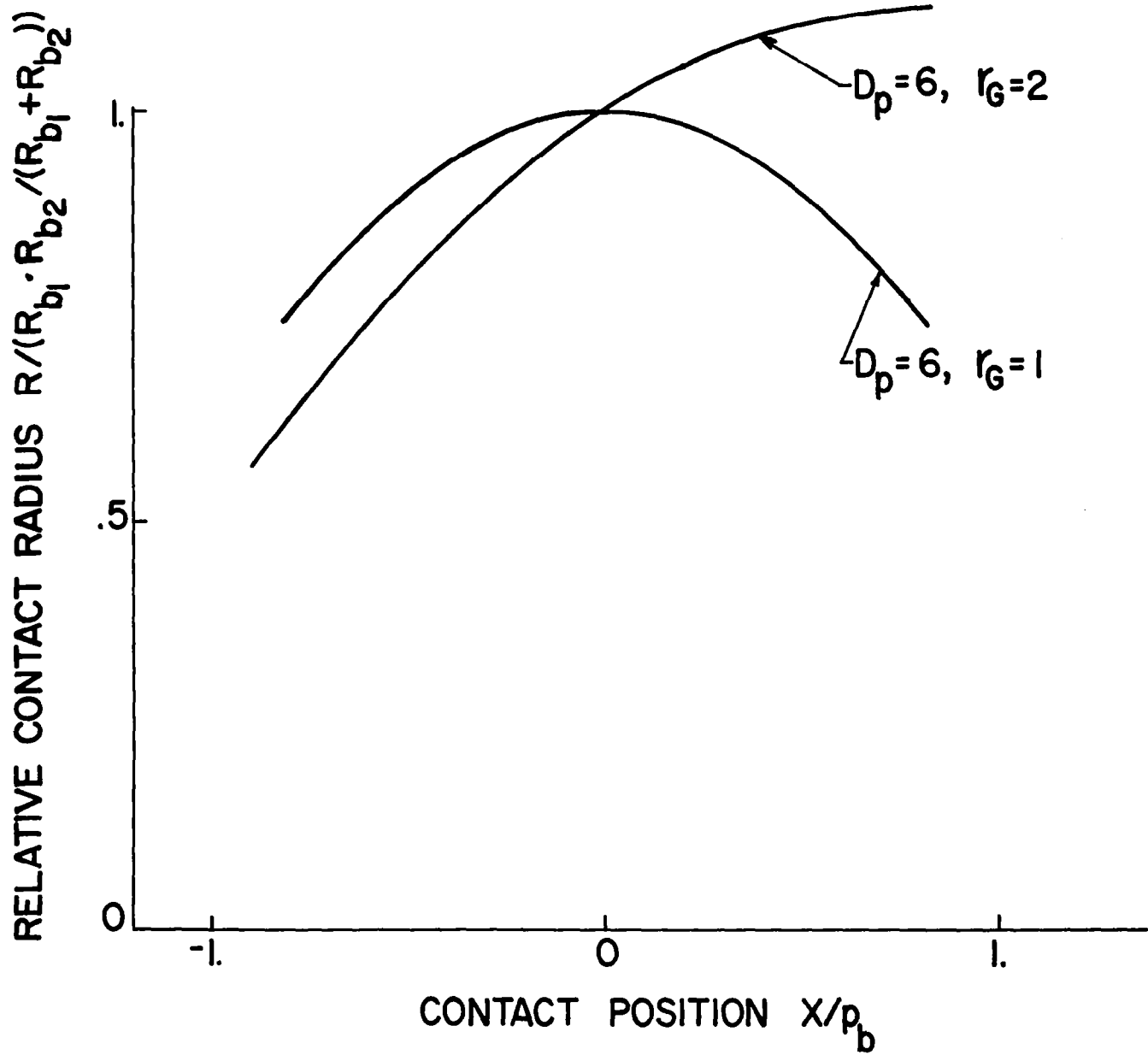
Fig. 3.1.   Variation of Relative Contact Radius with the Contact Position
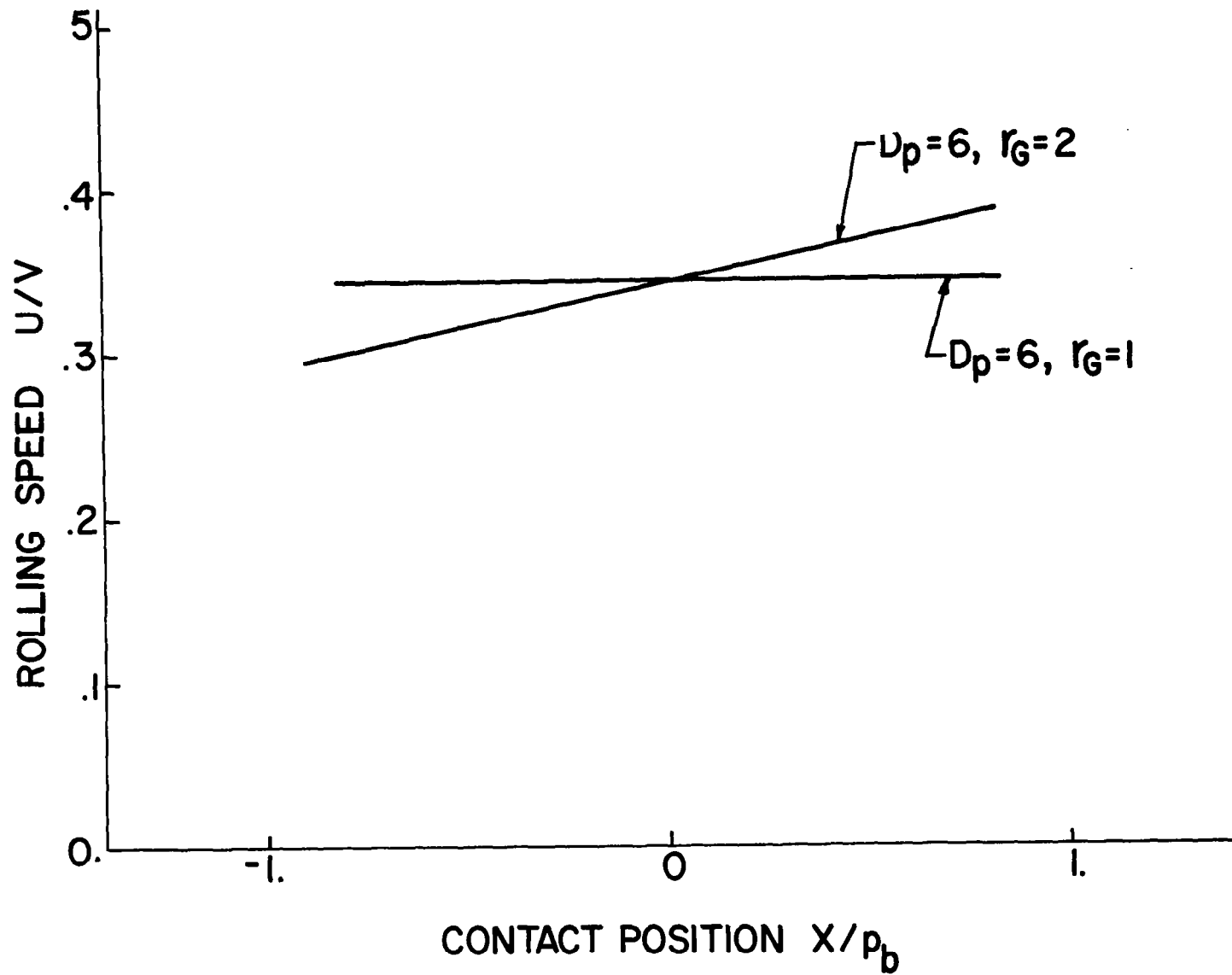
Fig. 3.2.   Variation of Rolling Speed with the Contact Position
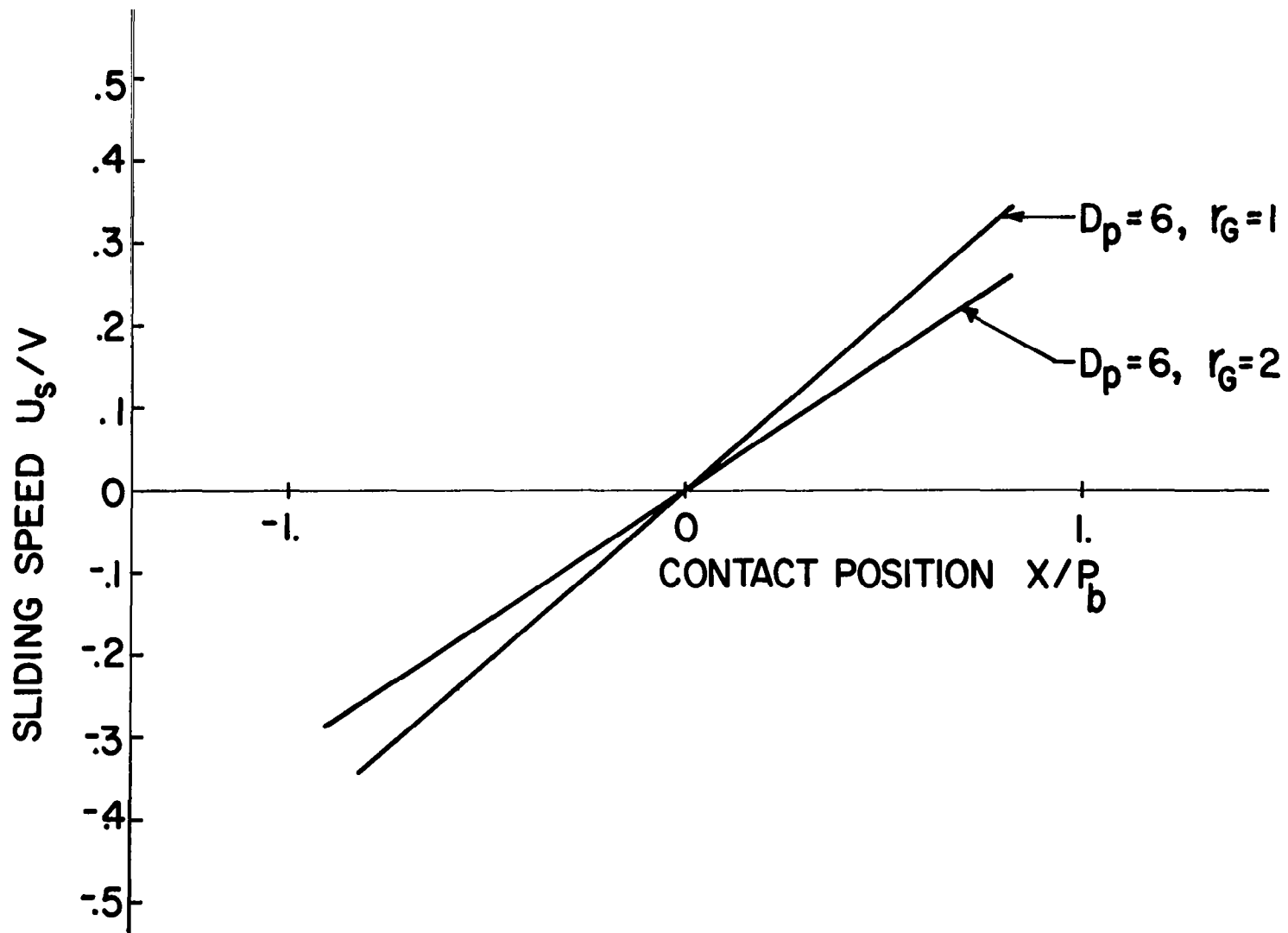
Fig. 3.3.   Variation of Sliding Speed with the Contact Position

pair of teeth in contact. Under this condition, it can not be assumed that the load is equally shared among the pairs of teeth in contact because this is a statically indeterminate case. Therefore, one must consider the tooth deflection under load for each pair in order to determine the load sharing characteristics among the pairs.

Considering a single tooth under a load per unit face width P at a point T as shown in Fig. 3.4, the defection δ is defined as the displacement of that point in the direction of load and the stiffness E_b is defined as the ratio of P to δ. The values of E_b of the tooth as it undergoes the engagement are determined by two independent methods. The first is a simplified variable cross-section cantilever beam analysis developed by Attia (Ref. 27) and the second is a numerical solution using the finite-element method. Details of these two methods are described below.

3.2.1. <u>Deflection Based on Beam Theory</u>

The deflection of a single tooth under a load P is approximated by treating it as a tapered cantilever beam. Attia considered the equivalence of virtual work on the tooth to the strain energy from bending as well as from shear and arrived at the following expression for the deflection.

$$\delta = \frac{P}{E} \cos^2\theta \left[12 \int_0^{y_P} \frac{(y_P - y)}{(2x)^3} \, dy + 3.12 \left(1 + \frac{\tan^2\theta}{3} \right) \int_0^{y_P} \frac{dy}{2x} \right]$$

$$= \frac{P}{E_b}$$

In the above, θ is the horizontal angle of the load and y_p is the ordinate of the intersection point from the load vector and y-axis, as shown in Fig. 3.4. The tooth involute profile can be described by a
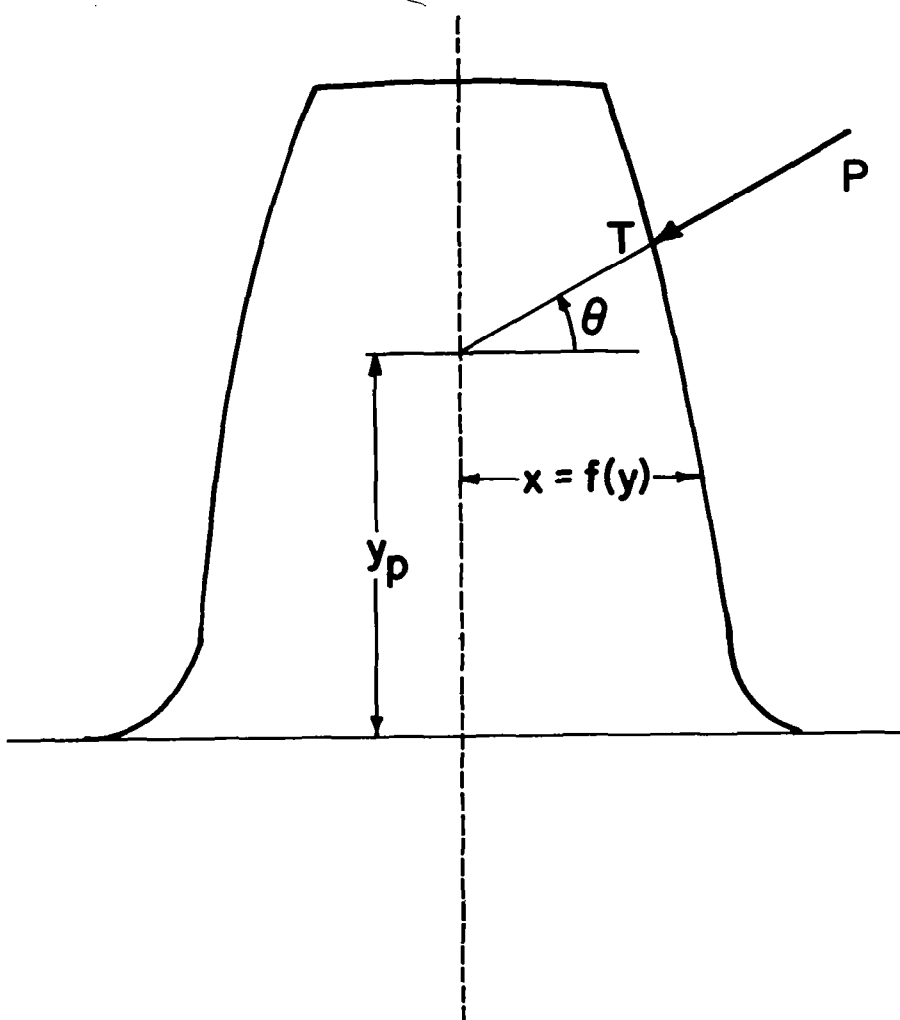
Fig. 3.4.   Configuration of a Single Tooth Under Load

mathematical function $x = f(y)$. This involute profile can be further

approximated by a symmetric trapezoid. Substituting values of y_p and

θ during actual contact, one can evaluate this integral.

3.2.2. Deflection Based on Finite-Element Method

A more accurate method in determining the deflection of a gear tooth

under a given load is the finite element method, which has been employed

recently by Chabert (Ref. 28). Unfortunately, his results for gears

cover only a few cases and cannot be readily used for the present gear

lubrication analysis. Therefore, it was necessary to generate a set

of new results by using an existing finite-element computer code for

the present investigation.

Figure 3.5 shows a typical quadrilateral element grid pattern for a

single tooth attached to the rim of a gear wheel. Using these grids as the

input, one can readily compute the deflection δ under a load P applied

at any point along the tooth profile. For this analysis, the boundaries

are considered to be fixed along the inside radius, and free along the

outside radius. The relation in linear elasticity gives rise to a

linear relationship between the dimensionless deflection, $\bar{\delta} = \dfrac{\delta}{R_r}$, and

the dimensionless load $\bar{P} = \dfrac{P}{ER_r}$, where

R_r = root radius of gear

P = load per unit face width

E = Young' modulus of gear material

The proportional constant $\bar{P}/\bar{\delta}$ can be called the dimensionless stiff-

ness $\bar{E}_b$, which only depends upon the shape of the configuration in Fig. 3.6,

and the loading position, and does not depend upon the size or the radius of the gear. Thus, one can represent the dimensionless stiffness as a function of the number of teeth, which reflects the change in shape, and the loading position. The values of $1/\overline{E}_b$ are plotted against these two variables in Fig. 3.6.

The results of bending stiffness E_b along the tooth profile computed from the finite-element method are compared with that computed from the beam theory in Fig. 3.7. The agreement is fair between the two methods for gears with small number of teeth. For gears with a larger number of teeth, the agreement becomes poor because in the method based on beam theory the deformation of the rim is not accounted. For this reason, the results based on the finite-element analysis have been adopted later in the gear lubrication analysis because they give more accurate results through the entire range of variables.

3.3. Dynamic Load Distribution

As the contact point of two teeth moves along the line of action, the contact load does not stay constant. The load variation is mainly caused by the following factors:

1. The transition from single to double and from double to single pair of contacts

2. The variation of bending stiffness along the line of action

3. The deviation of tooth profile from the true involute profile (This deviation is known as tooth profile error.)

To determine the variation of contact load as a function of the contact position X, it is necessary to derive the equations of motion governing the angular displacement θ_1 and θ_2 of two gears in mesh as shown in Fig. 3.8 . Considering the free body diagrams of each gear, the equations of motion are

27

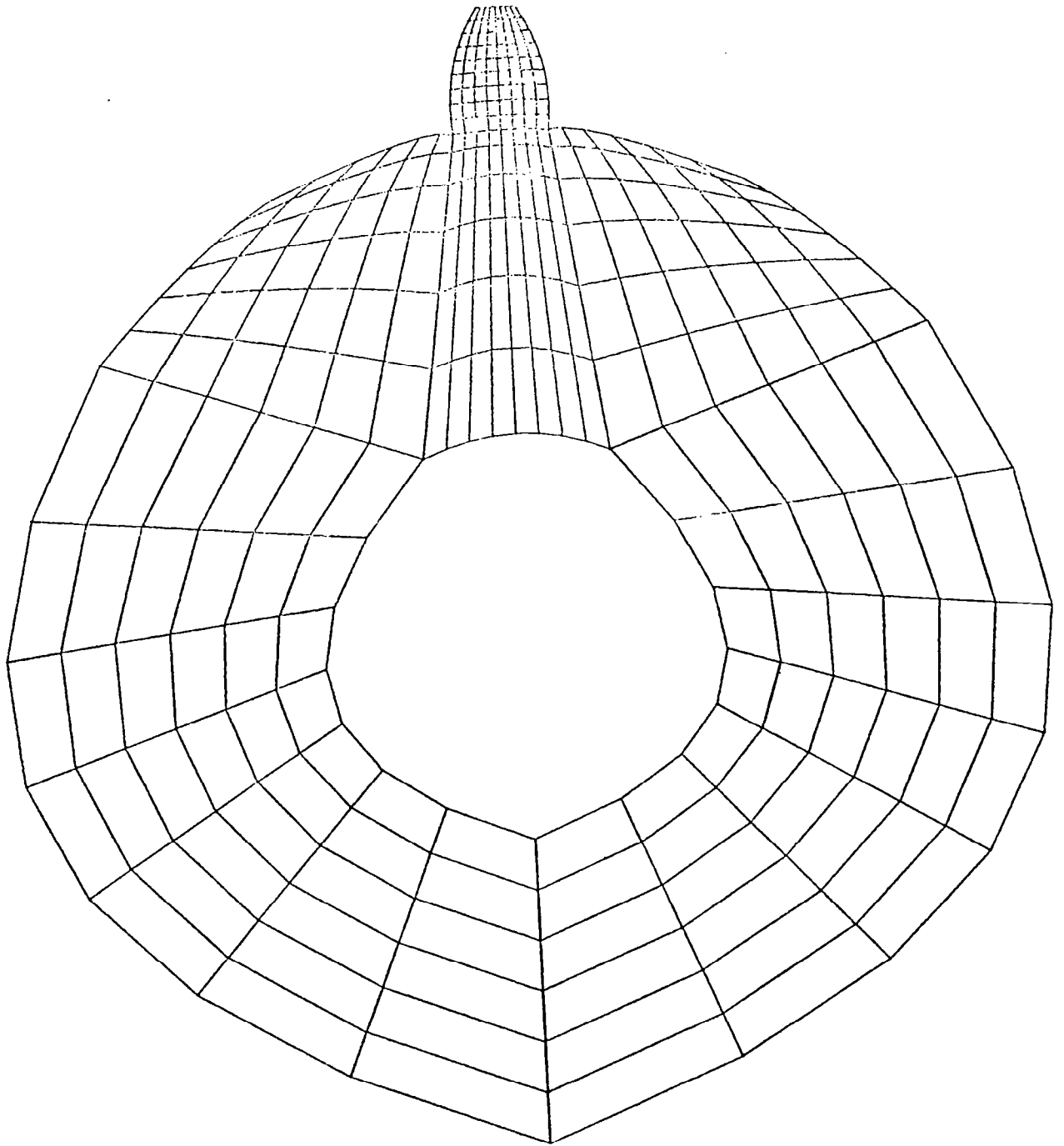Fig. 3.5.   Finite Element Mesh for a Single Tooth with Rim
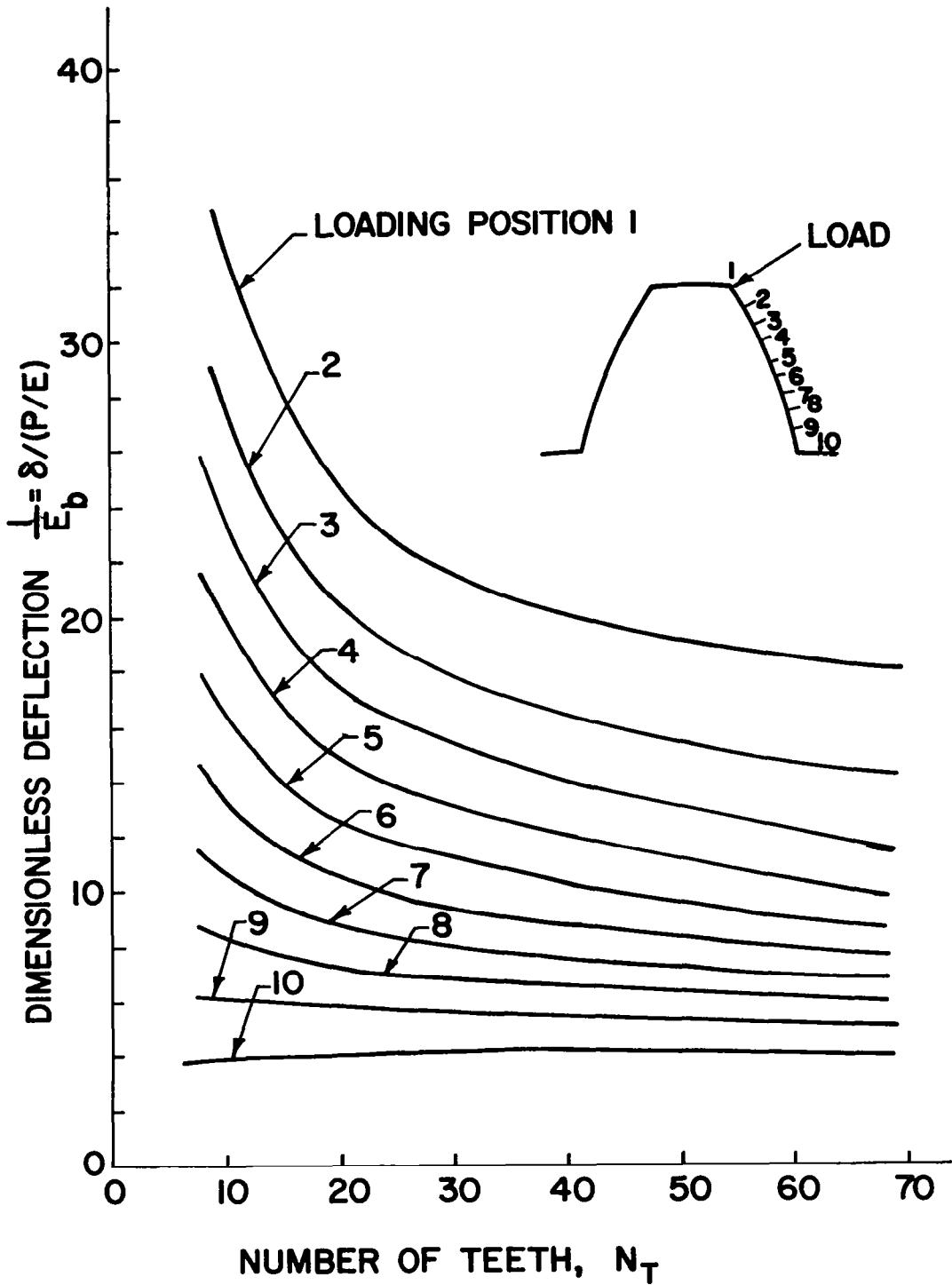
Fig. 3.6.   Dimensionless Deflection as a Function of Gear Teeth Number
and Loading Position

29
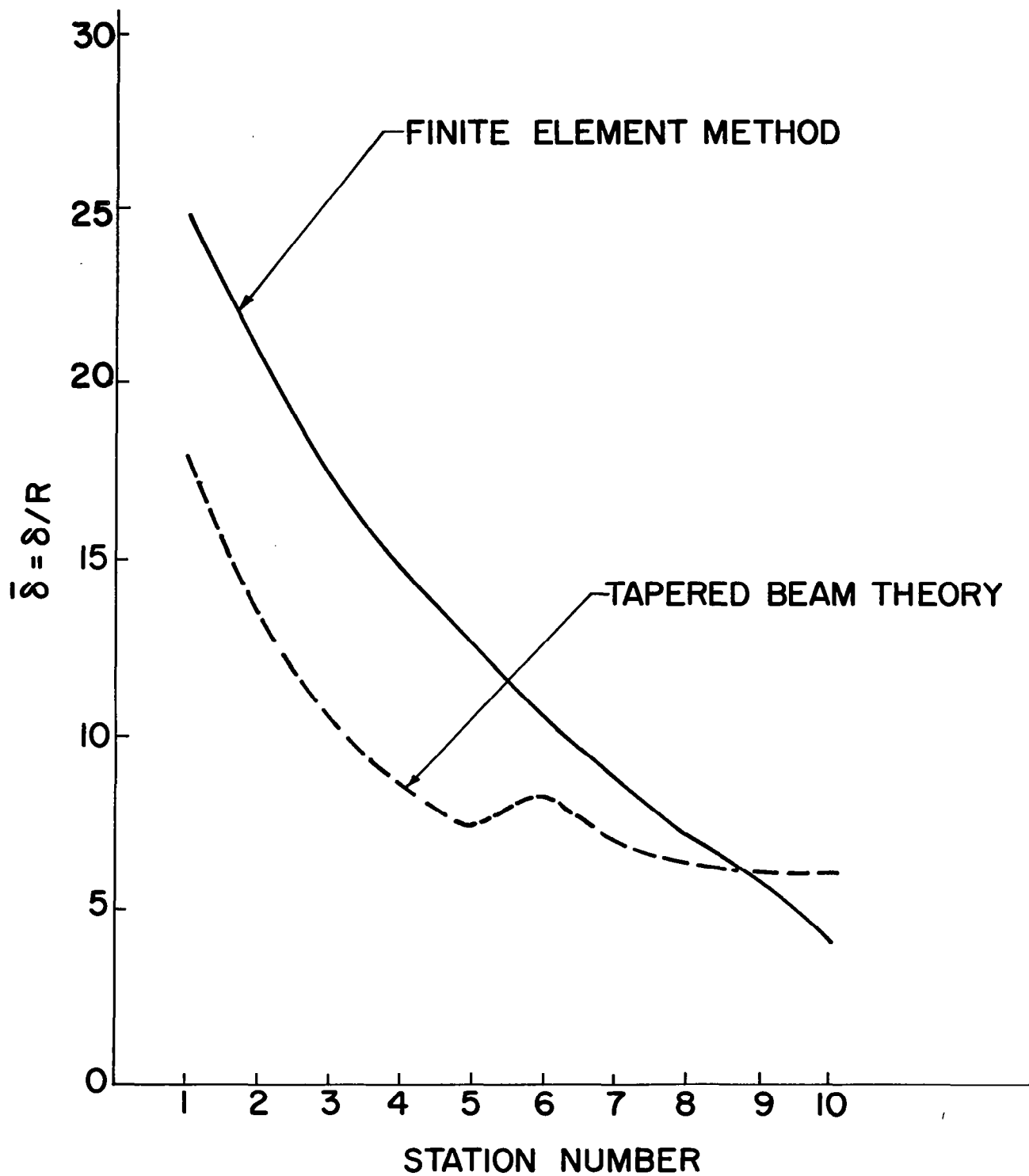
Fig. 3.7.　Comparison of Tooth Deflection Between Finite-Element Method and Attia's Tapered Beam Theory (No. of Gear Teeth = 20)

30
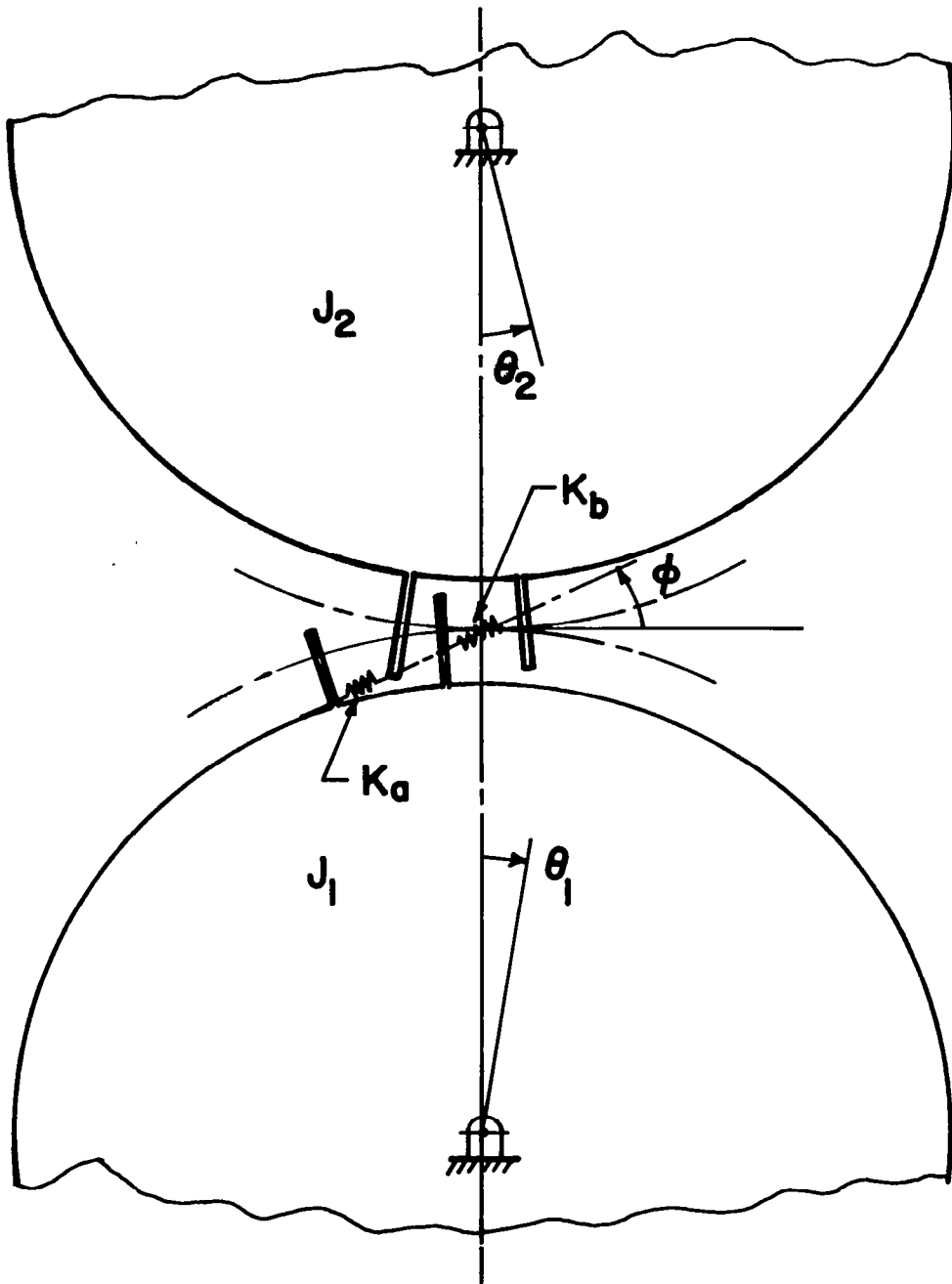
Fig. 3.8   A Dynamic Model of Meshing Gears

$$J_1 \ddot{\theta}_1 = R_{b_1} P_s - R_{b_1} P_d \qquad (3.12)$$

$$J_2 \ddot{\theta}_2 = R_{b_2} P_d - R_{b_2} P_s \qquad (3.13)$$

where J_1 and J_2 are the polar mass moment of inertia for pinion and gear, P_s is a steady state force resulted from the driving torque, and P_d is the unknown dynamic load. It is convenient to convert the angular coordinate into the coordinate along the line of action X. By virtue of the involute geometry,

$$X_1 = R_{b_1} \theta_1 \qquad (3.14)$$

$$X_2 = R_{b_2} \theta_2 \qquad (3.15)$$

where X_1, X_2 represent the displacement of undeformed tooth profiles along the line of action. Using the above relations, the equations of motion become

$$m_1 \ddot{X}_1 = P_s - P_d \qquad (3.16)$$

$$m_2 \ddot{X}_2 = P_d - P_s \qquad (3.17)$$

where m_1 and m_2 are the reduced mass,

$$m_1 = J_1 / R_{b_1}^2$$

$$m_2 = J_2 / R_{b_2}^2 \qquad (3.18)$$

Similar to the vibratory system of two masses connecting with a spring, the equations of motion can be reduced to a single equation by introducing an equivalent mass

$$M = \frac{m_1 m_2}{m_1 + m_2} \qquad\qquad (3.19)$$

and a relative displacement

$$X_R = X_1 - X_2 \qquad\qquad (3.20)$$

The reduced equation of motion, which can also include a viscous damping force, takes the following form

$$M\ddot{X}_R + C_o \dot{X}_R + P_d = P_s \qquad\qquad (3.21)$$

The total dynamic load P_d is the sum of the forces exerted by all contacting pairs of teeth along the line of action. For a single contacting pair with true involute profiles, the contacting load is simply the product of the combined stiffness and the relative displacement X_R.

$$P_d = KX_R \qquad\qquad (3.22)$$

where

$$K = \frac{E_{b_1} \cdot E_{b_2}}{E_{b_1} + E_{b_2}} \qquad\qquad (3.23)$$

E_{b_1} and E_{b_2} are the stiffnesses of the pinion and the gear, which vary with the contact position X.

If the tooth profile error is included in the analysis, the dynamic load becomes

$$P_d = K(X_R - e) \qquad\qquad (3.24)$$

where e is the sum of profile errors of both teeth, $e_1(X)$ and $e_2(X)$. e_1 is considered to be negative when the profile is extended beyond the true involute curve.

33

For double pairs of teeth in contact, the dynamic load becomes the sum of the load on each pair. Thus

$$P_d = \sum_{i=a,b} K_i (X_R - e_i) \tag{3.25}$$

where subscripts a and b denote the variable pertaining to either the preceding or the following pair of teeth.

At any instant, if the term $X_R - e_i$ is less than zero, the teeth separation is occurred. There should be no load acting on this pair of teeth at the time of separation and therefore K has a zero value.

Given the profile error e_1 and e_2 from the measurement and the variable bending stiffness E_{b_1} and E_{b_2}, the resultant equation can be treated as a second order differential equation with a state dependent coefficient. This equation is solved numerically by Runge-Kutta's method. The unknown initial conditions $X_R(0)$ and $\dot{X}_R(0)$ can be iterated by taking the previous calculated X_R and $\dot{X}_R$ at the end point of the single pair teeth contact as a new trial. The results of this calculated dynamic load for cases of different gear geometry and operation conditions are discussed in Chapter VIII.

IV. TRANSIENT ISOTHERMAL LUBRICANT FILM THICKNESS

4.1. Introduction

The film thickness between gear teeth based on steady
state EHD theory is questionable since the load P, relative radius
of curvature R and speed U are all varied along the line of action. An
improved approach must therefore consider the time-dependent equation
for the fluid flow between the two contacting surfaces and include the
time-dependent parameters.

The generalized theory for predicting the transient effect in the
lubrication of Hertzian contact was developed by Vichard [Ref. 26].
His analysis is extended and used for gear lubrication in this chapter.
The result of film thickness from this calculation is also compared with
that from the quasi-steady state theory.

4.2. Transient Reynolds' Equation

The equation governing the local fluid film thickness h and pressure
p between two contacting surfaces, as shown in Fig. 4.1 , is the well
known Reynolds' equation,

$$\frac{\partial}{\partial \xi}\left(\frac{\rho h^3}{\mu}\frac{\partial p}{\partial \xi}\right) = 6\left[\frac{\partial}{\partial \xi}\left(\rho h(u_1 + u_2)\right) + 2\frac{\partial}{\partial t}(\rho h)\right] \qquad (4.1)$$

where u_1 and u_2 are the speed of contacting surfaces. The assumptions
used in deriving this equation are the usual one associated with analysis
of concentrating contact except the following.

i) Time dependent term $\partial(\rho h)/\partial t$ is retained in order to solve for
the dynamic response of film to the rapid changes of load and surface
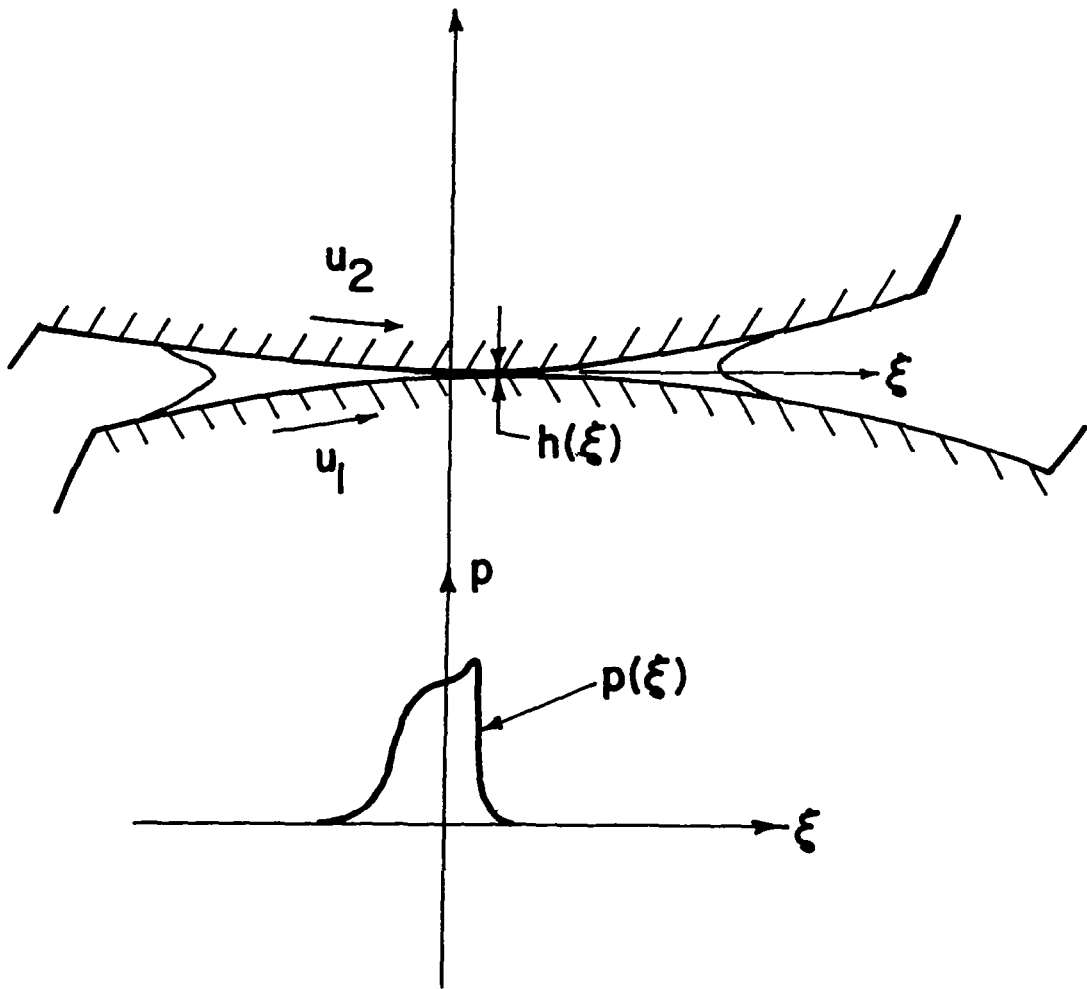curvatures.

Fig. 4.1.   Film Thickness and Pressure Profiles Between Gear Teeth

ii) One dimensional approximation is used since the side flow is very small compared with the flow in main direction of motion.

iii) Inertia forces are small compared with the magnitude of viscous shearing terms, therefore they can be neglected. It is further assumed that the viscosity response of lubricant to pressure change under iso-thermal condition can be represented by

$$\mu = \mu_T e^{\alpha p} \tag{4.2}$$

where μ_T is the lubricant viscosity based on inlet temperature T at the inlet region and α is the pressure viscosity coefficient.

If the effect of compressibility on lubricant is negligible, then the equation becomes

$$\frac{\partial}{\partial \xi} \left(h^3 e^{-\alpha p} \frac{\partial p}{\partial \xi} \right) = 12 \, \mu_T \left(u \frac{\partial h}{\partial \xi} + \frac{\partial h}{\partial t} \right) \tag{4.3}$$

where U is the mean rolling velocity and it is defined as $u = (u_1 + u_2)/2$. After normalization, Eq. (4.3) becomes

$$\frac{\partial}{\partial \xi} \left(H^3 \frac{\partial Q}{\partial \xi} \right) = N \left(A \frac{\partial H}{\partial \xi} + S \frac{\partial H}{\partial \tau} \right) \tag{4.4}$$

where $\quad H \;=\; \dfrac{h}{R_i}$

$$Q \;=\; \frac{1 - e^{-\alpha p}}{G}$$

$$N \;=\; \frac{12 \, \mu_T u}{E'R}$$

$$A = \frac{R}{R_i}$$

$$S = \frac{\omega R}{u}$$

$$G = \alpha E'$$

$$R = \frac{r_1 r_2}{r_1 + r_2}$$

$$R_i = \frac{r_1 r_2}{r_1 + r_2} \quad r_1 \text{ and } r_2 \text{ evaluated at pitch point}$$

r_1, r_2= local radii of curvature of the two contacting surfaces

$$E' = \pi / \left(\frac{1 - \nu_1^2}{E_1} + \frac{1 - \nu_2^2}{E_2} \right)$$

ν_1, ν_2= Poisson ratios of the two material

E_1, E_2= Young's modulsus of the two material

ω = time base

$\bar{\xi}$ = ξ / R_i

τ = ωt dimensionless time

and load

$$\bar{P} = - \int \frac{\ell n(1 - GQ)}{G} d\bar{\xi} \tag{4.5}$$

4.3. Solution of Reynolds' Equation with Hertzian Boundary

For heavily loaded lubricated contacts the surface deformation of the solid can be assumed to conform to the Hertzian dry contact. Accordingly, the film thickness is equal to the sum of uniform level H_o and the Hertzian deformation H_d. Thus

$$H(\bar{\xi}, \tau) = H_o(\tau) + H_d(\bar{\xi}, \tau) \tag{4.6}$$

38

where

$$H_d = 0 \quad \text{for} \quad |\bar{\xi}| \leq 2\sqrt{\bar{P}A} \qquad (4.7)$$

and

$$H_d = 2\bar{P}\left[\frac{|\bar{\xi}|}{2\sqrt{\bar{P}A}}\sqrt{\frac{\bar{\xi}^2}{4\bar{P}A} - 1} - \ell n\left(\frac{|\bar{\xi}|}{2\sqrt{\bar{P}A}} + \sqrt{\frac{\bar{\xi}^2}{4\bar{P}A} - 1}\right)\right] \qquad (4.8)$$

for

$$|\bar{\xi}| > 2\sqrt{\bar{P}A}$$

After integrating Eq. (4.4) twice with boundary conditions

$$\frac{\partial Q}{\partial \bar{\xi}}\bigg]_{0,\tau} = 0 \quad \text{and} \quad Q(0,\tau) = \frac{1}{G}$$

and substituting the relations in Eq. (4.6) to (4.8) for H, one obtains

$$\frac{2}{GN}\sqrt{\left(\frac{\bar{P}}{A}\right)^3} - G_4 = \frac{S}{\sqrt{\bar{P}A}}\left[\frac{2}{3}\frac{\bar{P}\dot{A}}{A}G_1 + 2\dot{\bar{P}}G_2 - \dot{H}_o\left(G_3 + \frac{4\bar{P}^3}{H_o^3}\right)\right] \qquad (4.9)$$

with

$$\dot{A} = \frac{dA}{d\tau}$$

$$\dot{\bar{P}} = \frac{d\bar{P}}{d\tau}$$

$$\dot{H}_o = \frac{dH}{d\tau}$$

$$G_1 = \int_0^1 \eta(1 - \eta^2)^{1.5}\frac{d\eta}{\lambda} \qquad (4.10)$$

$$G_2 = \int_0^1 \eta^3\left[\ell n\left(\frac{1 + \sqrt{1-\eta^2}}{\eta}\right) - \sqrt{1-\eta^2}\right]\frac{d\eta}{\lambda} \qquad (4.11)$$

$$G_3 = \int_0^1 \eta^3\frac{d\eta}{d\lambda} \qquad (4.12)$$

39

$$G_4 = \int_0^1 \left[\eta^2 \sqrt{1-\eta^2} - \eta^4 \ln \left(\frac{1 + \sqrt{1-\eta^2}}{\eta} \right) \right] \frac{d\eta}{\lambda} \tag{4.13}$$

and with

$$\lambda = \left[\frac{\beta \eta^2}{2} + \sqrt{1-\eta^2} - \eta^2 \ln \left(\frac{1 + \sqrt{1-\eta^2}}{\eta} \right) \right]^3 \tag{4.14}$$

$$\beta = \frac{H_o}{\bar{P}}$$

η = dummy variable for integration

The left hand terms in Eq. (4.9) governs the steady state film thickness, whereas the right hand terms measure the squeeze film. As suggested in Vichard's analysis, the four G_i functions in Eq. (4.9) can be approximated by the following exponential functions of β

$$G_i = a_i \beta^{-b_i} \tag{4.15}$$

where the constant a_i's and exponent b_i's are taken from Ref. 26 and are tabulated in Table 4.1.

4.4. Film Thickness Between Gear Teeth

When solving Eq. (4.9) for the dynamic lubricant film thickness between a pair of engaging teeth, the kinematic relations derived in Chapter III must be used. Defining $\widetilde{X} = X/R_i$, where X is the position of contact in the line of action and R_i is the relative radius of curvature for the tooth contacting surfaces at the pitch point. The variable $\widetilde{X}$ becomes the natural choice for representing the dimensionless time τ in Eq. (4.9) since all the kinematic variations are defined in terms of this dimensionless contact position $\widetilde{X}$. Using the previous obtained kinematic relations for R and U, the parameters $\dot{A}$, S and $\dot{\bar{P}}$ in Eq. (4.9) become
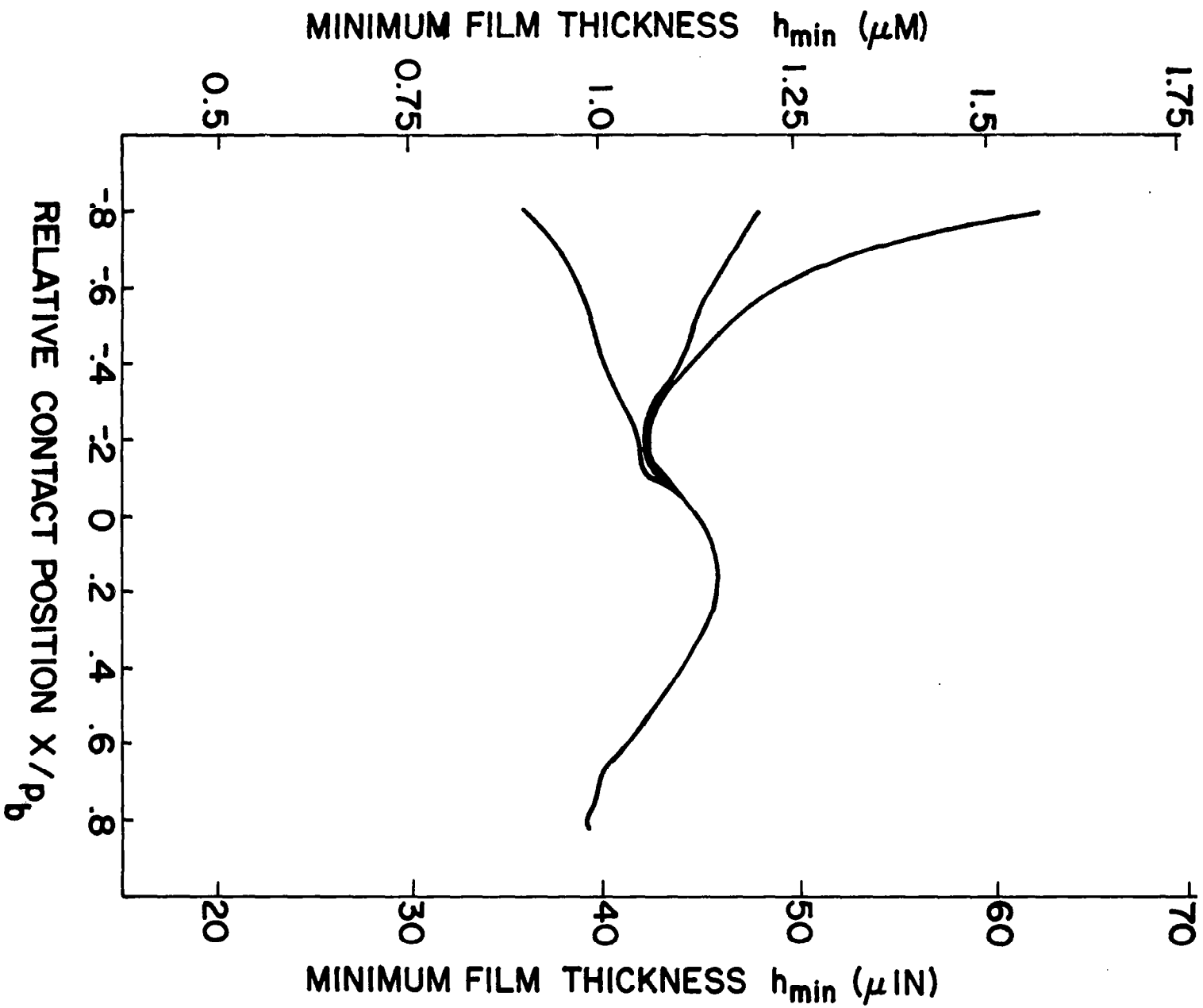
Fig. 4.2. Influence of the Initial Film Thickness on Dynamic Film
Thickness Variation

41

$$\dot{A} = \frac{dA}{d\tau} = \frac{\left(R_{b_2} - R_{b_1}\right) \tan \phi - 2X}{\left(R_{b_1} + R_{b_2}\right) \tan \phi} \qquad (4.16)$$

$$S = \frac{\omega R}{U} = \frac{V \cos \phi}{R_i} \frac{R}{U} = \frac{R \cos \phi}{R_i} \bigg/ \left(\sin \phi + \frac{\cos \phi}{2} \cdot \frac{\left(R_{b_2} - R_{b_1}\right) X}{R_{b_1} R_{b_2}}\right)$$

$$\dot{\bar{P}} = \frac{d\bar{P}}{d\tau} \approx \frac{\Delta \bar{P}}{\Delta X}$$

These expressions for $\dot{A}$, S and $\dot{\bar{P}}$ in conjunction with known R, U, μ, G, can be substituted into Eq. (4.9) for determining the dynamic film thickness.

In solving Eq. (4.9), the line of action is divided into 100 uniformly spaced grid points. The dynamic load P and load change $\Delta \bar{P}/\Delta \bar{X}$ is obtained from the analysis in Chapter III. The equation is then solved numerically by Runge-Kutta method for discrete film thickness at these grids. The initial film thickness $H_o(0)$ depends on how the tip of the gear and the root of the pinion come in contact. The effect of $H_o(0)$ on the subsequent film distribution along the line of action has been examined by using three arbitrary chosen $H_o(0)$ for a given run. As shown in Fig. 4.2 , it was found that the influence of $H_o(0)$ only penetrates into a small region near the entrance of action line. For the most part the film thickness is not affected by this choice of $H_o(0)$. For the subsequent runs, the value $H_o(0)$ is chosen to be equal to the quasistatic value multiplied by a constant factor of 1.5.

The deviation of dynamic film thickness from the steady film thickness is shown in Fig. 4.3 for a pair of 28-tooth, 8-pitch gears. In this figure, the squeeze film effect only causes a phase shift of the
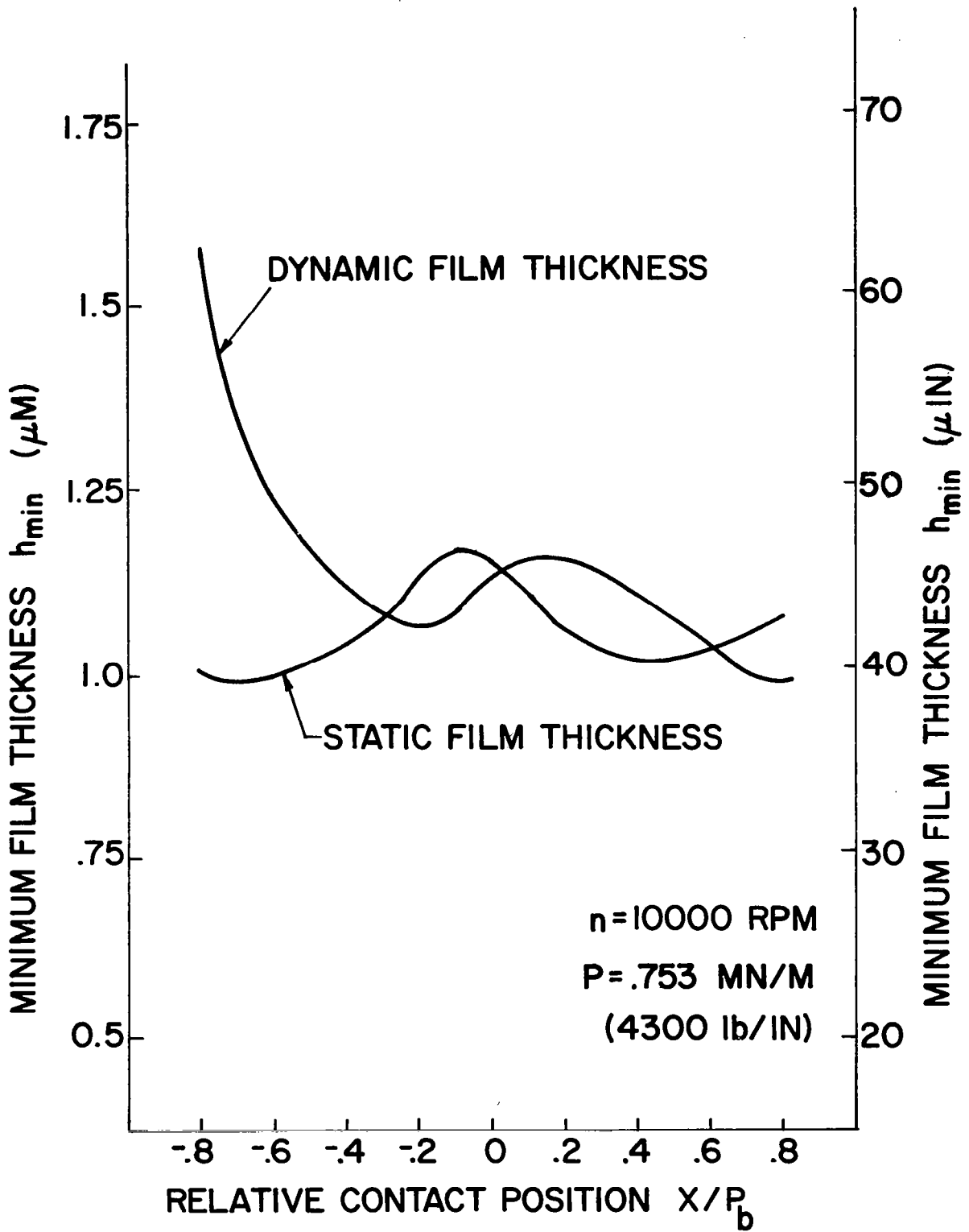
Fig. 4.3. Comparison Between the Steady State and Dynamic Film
Thicknesses

43

TABLE 4.1

NUMERICAL VALUES FOR G FUNCTIONS

$$G_i = a_i \beta^{-b_i} \qquad i = 1,2,3,4$$

	a_4	b_4	a_3	b_3
$\beta < 6.66$	0.394	1.387	2.0965	2.247
$\beta > 6.66$	0.4747	1.476	1.378	2.0496

	a_2	b_2
$\beta < 1$	0.181	1.408
$1 < \beta < 20$	0.1883	1.52
$20 < \beta < 220$	0.2948	1.667
$\beta > 220$	0.5135	1.781

	a_1	b_1
$\beta < 1$	0.833	1.249
$1 < \beta < 22$	0.799	1.1285
$\beta > 22$	0.581	1.0224

minimum film thickness and it has little effect on the level of the minimum film thickness. Also, from Eq. (4.9) the squeeze number S is independent of the operating speed u. Thus, the squeeze film effect is also independent of the operating speed.

V. ANALYSIS OF FRICTIONAL HEAT GENERATION AND FLASH TEMPERATURE

5.1. Introduction

As discussed earlier, the lubricant film thickness, the equilibrium surface temperature and the flash temperature are all mutually dependent quantities, and are solved together by an iterative procedure to be given in Chapter VII.

In the last Chapter, the analysis of film thickness for given surface temperatures is presented. This Chapter is devoted to the analysis of the flash temperature as well as the frictional heat generation in the contact.

The heat generation is assumed to be solely due to the shear of lubricant, which is modelled as a non-Newtonian liquid with a limiting shear stress under high pressure.

Equations of heat balance due to conduction are formulated in the lubricant film as well as in the two bounding solids at discrete points along the contact region. These equations are solved numerically for the heat generation and the flash temperature. Details of the liquid model and the formulation of heat balance are given in the ensueing sections.

5.2. A Non-Newtonian Viscosity Model

It has been demonstrated (Ref. 29) that the use of Newtonian viscosity model for lubricant flow in high speed, heavily loaded lubri-cated contacts can yield friction and heat generation far greater than those measured experimentally. It is believed that, under these severe conditions, the lubricant ceases to be Newtonian and one must seek a suitable non-Newtonian model for a more accurate prediction of friction in the contact.

46

The frictional coefficient in EHD sliding contacts was investigated in detail first by Crook (Ref. 30) with a two disk machine. The measured frictional coefficient was found to vary with the sliding velocity as shown in Fig. 5.1. The same trend has since been observed by many other researchers (Refs. 31, 32). Dyson (Ref. 25) interpreted this behavior of sliding friction by dividing the friction curve vs. speed into three regions. These are a linear ascending region at low sliding speed, a non-linear transitional region till it has passed the peak of friction curve, and finally a thermal descending region at very high sliding speeds. The level of this frictional curve was found to increase with load and to decrease with temperature.

In an attempt to interpret these features, Dyson (Ref. 25) employed a fluid viscoelastic model, originally proposed by Barlow and Lamb (Ref. 33), to explain the fluid behavior in the linear and thermal region. As a modification of Dyson's analysis, Trachman (Ref. 29) used a unified theory of transient viscosity and hyperbolic limiting shear models to predict the values of frictional coefficient in all three regions on this curve. Close correlation between the predicted results and his measured values appear to lend considerable credence to these models.

The descending region of the frictional curve deserves special attention since most of the high speed gears operate in this region. The model developed by Dyson for predicting the friction at high sliding speed is used here in high speed gear analysis.

Fluids exhibit viscoelastic properties when subject to oscillatory shear. When the frequency for applied shear is very high, the ratio of shear stress τ_S to strain ϵ_S is called limiting shear modulus G_∞ for
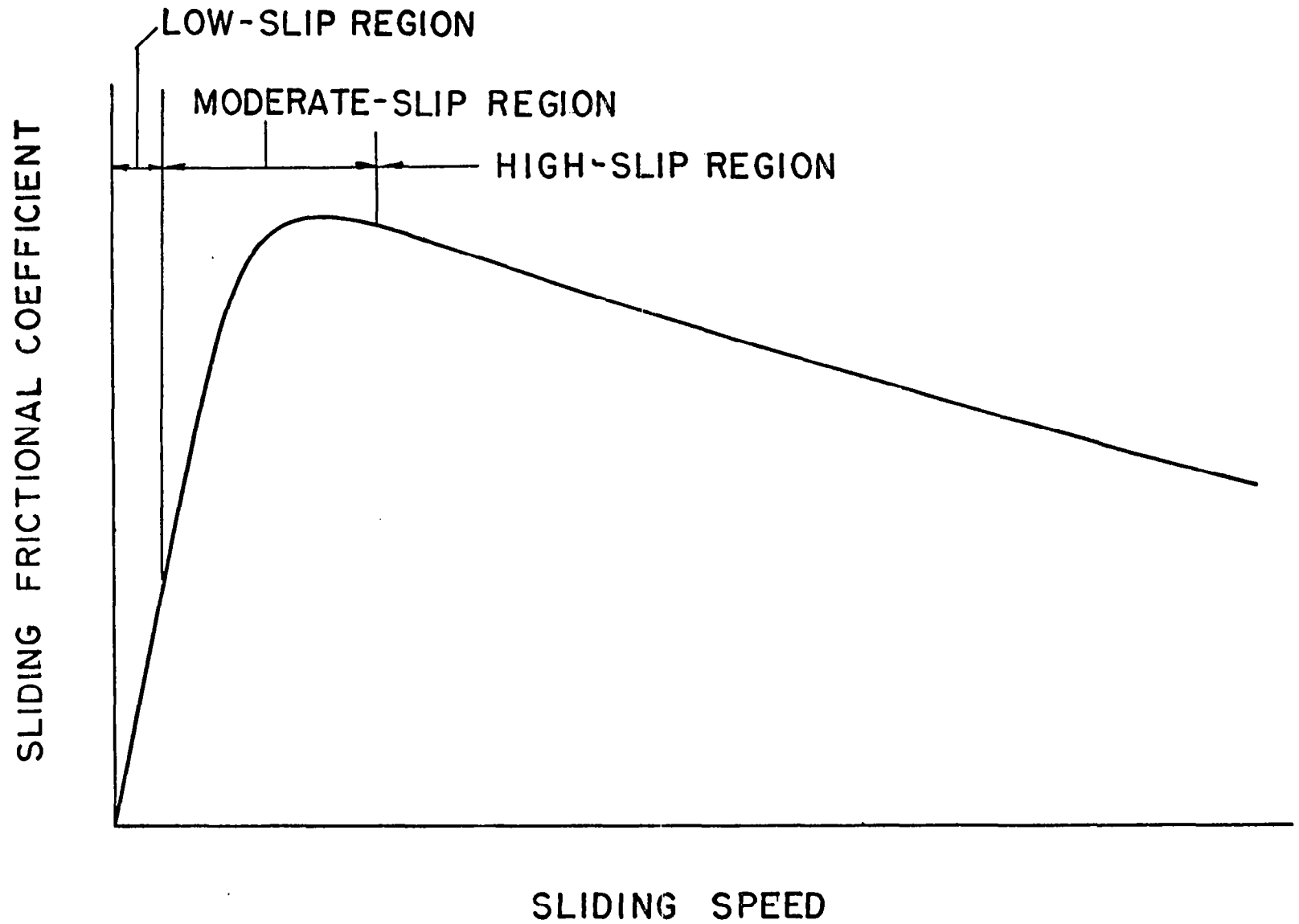
47

Fig. 5.1. Variation of Frictional Coefficient With Sliding Speed

oscillatory shear. Extending this modulus for continuous shear for application in elastohydrodynamic lubrication, Dyson found that the inclusion of a simplified Oldroyd parameter $k_S = 7.5$, such that $\overline{G}_\infty$ for continuous shear is equal to G_∞/k_S, shows a good correlation with Smith's (Ref. 31) experimental data at high loads.

It is hypothesized that similar to the yield stress in solids, the liquid can have a ceiling stress when subjected to a high pressure at a high strain rate. Dyson suggested that the limiting shear stress $\tau_{Smax.}$ is proportional to the aforementioned limiting shear modulus $\overline{G}_\infty$ by the relation $\tau_{Smax.} = C \cdot \overline{G}_\infty$. In evaluating this limiting shear modulus $\overline{G}_\infty$ as a function of temperature and pressure, Hutton (Ref. 34) determined experimentally the variation of $\overline{G}_\infty$ with temperature at atmospheric pressure for high viscosity index mineral oil as

$$\frac{1}{\overline{G}_\infty} = 2.52 + 0.025\ T \tag{5.1}$$

where $\overline{G}_\infty$ is in GN_m^{-2} (10^{10} dyne/cm^2) and T is in $^\circ$C. Since the direct measurement of this modulus at high pressure is difficult, Dyson arrived at a relation between the modulus and pressure based on frictional measurements by Smith (Ref. 31). He proposed

$$\overline{G}_\infty(p,T) = 0.4 \left[\frac{3p}{2.52 + 0.024T} \right] - 10^8 \tag{5.2}$$

converting into English units. Equation (5.2) becomes

$$\overline{G}_\infty(p,T) = \frac{1.2p}{2.52 + .0133(T-492)} - 1.45 \times 10^4 \tag{5.3}$$

where $\overline{G}_\infty$ is in psi, p is also in psi, and T is in $^\circ$R Eq. (5.3) can only be used for high pressures. For low pressure the $\overline{G}_\infty(P,T)$ predicted

using this equation can become lower than that calculated from Eq. (5.3).
Whenever this condition occurs, $\overline{G}_\infty$ is taken to be that corresponding to
the atmospheric pressure in the present analysis.

5.3. Surface Temperature Rise

Heat is generated by viscous shearing of lubricant between the sliding
contact surface, This heat is either carried away by the lubricant
through convection or transferred into the surfaces by conduction; the
relative importance between these two modes of heat transfer in EHD
contacts was examined by Trachman (Ref. 29). He showed that the con-
vective mode is only important at extremely high rolling speeds. For
gears, even for most of the high speed gears current in practice, the
heat convected by lubricant is still negligible in comparison to the
heat diffused into the solids.

If the heat generation at each point along a Hertzian sliding con-
tact is known, the surface temperature can be readily determined by
using the one-dimensional transient heat conduction analysis for a semi-
infinite plane subjected to an arbitrarily distributed fast moving heat
source. However, the heat generation is dependent upon the lubri-
cant film temperature which is in turn dependent upon the surface tem-
perature. The system variables are, therefore, mutually dependent, and
must be solved as a coupled system.

The lubricant local velocity profile and temperature profile for
the very high sliding cases were estimated by Plint (Ref. 35) and
later confirmed by Trachman's analysis (Ref. 29). Under this sliding
condition, their results show a sharp S-shaped velocity profile across
the film with a large velocity gradient at the mid-plane. The temperature

attains a maximum at the same median plane and decreases almost linearly to both surfaces. Since shearing of the lubricant occurs mainly in the mid-plane most of the heat is also generated here in this thin layer. This results into the S-shaped velocity profile as well as the triangular temperature distribution across the profile.

For gear teeth contacts, the sliding speed is generally high enough to warrant the assumption that the shear stress approaches the limiting shear stress postulated by Dyson.

$$\tau_{Smax.} = \overline{G}_\infty / 4 \tag{5.4}$$

where $\overline{G}_\infty$ is a function of p and T, given in Eq. (5.3). With this assumption, the local heat flux generated in the film becomes

$$q = \tau_{Smax.} |u_1 - u_2|$$

$$= \frac{1}{4} |u_1 - u_2| \left[\frac{1.2p}{2.52 + .0133 (T_{mid.} - 492)} - 1.45 \times 10^4 \right] \tag{5.5}$$

where q, $\tau_{Smax.}$, p, and T are functions of the contact coordinate ξ. The distribution p is assumed to be Hertzian. The heat balance equations in the lubricant film based on the assumption that all the heat generated is at the mid-film, as shown in the sketch below
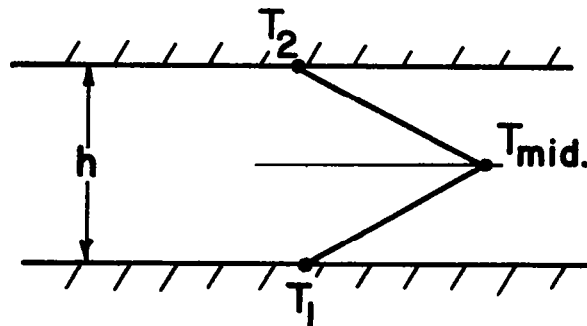
$$q_1 = \Lambda q \quad = 2k_f \frac{T_{mid} - T_1}{h} \tag{5.6}$$

$$q_2 = (1-\Lambda)q = 2k_f \frac{T_{mid} - T_2}{h} \tag{5.7}$$

where

Λ = local heat partition function

T_1, T_2 = temperature of the contacting surfaces

and

k_f = thermal conductivity of the lubricant

h = plateau film thickness, a constant in the contact region.

Equations (5.6) and (5.7) can be solved for T_{mid} and Λ to yield

$$T_{mid} = \frac{1}{2}(T_1 + T_2) + \frac{qh}{4k_f} \tag{5.8}$$

$$\Lambda = \frac{1}{2} + \frac{k_f}{hq}(T_2 - T_1) \tag{5.9}$$

Substituting Eq. (5.8) and Eq. (5.9) into Eq. (5.6) and Eq. (5.7), one obtains

$$q_1 = \frac{k_f}{h}(T_2 - T_1) + \frac{1}{2}q \tag{5.10}$$

$$q_2 = \frac{k_f}{h}(T_1 - T_2) + \frac{1}{2}q \tag{5.11}$$

The surface temperature can be calculated by using the solution of one-dimensional transient heat conduction analysis for a semi-infinite plane under an arbitrarily distributed, fast-moving heat source (Ref. 36). Thus,

$$T_1(\xi) = T_{b_1} + \left(\frac{1}{\pi \rho_1 c_1 u_1 k_1}\right)^{1/2} \frac{k_f}{h} \int_{-\infty}^{\xi} \left[T_2(\xi') - T_1(\xi') + \frac{q(\xi')}{2} \right] \frac{d\xi'}{(\xi - \xi')^{1/2}} \tag{5.12}$$

$$T_2(\xi) = T_{b_2} + \left(\frac{1}{\pi \rho_2 c_2 u_2 k_2}\right)^{1/2} \frac{k_f}{h} \int_{-\infty}^{\xi} \left[T_1(\xi') - T_2(\xi') + \frac{q(\xi')}{2}\right] \frac{d\xi'}{(\xi-\xi')^{1/2}}$$

(5.13)

Substituting Eq. (5.8) into Eq. (5.5), one obtains a relation between $q(\xi)$, $T_1(\xi)$ and $T_2(\xi)$ in the following form.

$$q(\xi) = \frac{1}{4} |u_1 - u_2| \left[\frac{1.2p(\xi)}{2.52 + .0133 \left(\left(.5(T_1(\xi) + T_2(\xi)) + \frac{q(\xi)h}{4k_f}\right) - 492.\right)} - 1.42 \times 10^4\right]$$

(5.14)

Equations (5.12), (%.13), and (5.14) are a non-linear system governing q, T_1, and T_2 in the contact region.

Equations (5.12) and (5.13) are recognized as Volterra's integral equation of the second kind (Ref. 37). These equations can be readily integrated numerically by dividing the contact zone into ten uniform intervals. The resulting equations for calculating temperatures at the grid point i+1 becomes

$$T_{1,i+1} = I_1 + J_1\left(T_{2,i+1} - T_{1,i+1}\right) + K_1 \cdot q_{i+1}$$

(5.15)

$$T_{2,i+1} = I_2 + J_2\left(T_{1,i+1} - T_{2,i+1}\right) + K_2 \cdot q_{i+1}$$

(5.16)

where

$$I_1 = \left(\frac{1}{\pi \rho_1 c_1 u_1 k_1}\right)^{1/2} \left(\frac{k_f}{h}\right) \left(\sum_{j=1}^{i} \omega_j \frac{\left(T_{2,j} - T_{1,j}\right)}{\left(\xi_{i+1} - \xi_j\right)^{1/2}} \Delta\xi + T_i \sqrt{\Delta\xi}\right)$$

$$+ \frac{1}{2} \left(\frac{1}{\pi \rho_1 c_1 u_1 k_1}\right)^{1/2} \left(\sum_{j=1}^{i} \omega_j \frac{q_j \Delta\xi}{\left(\xi_{i+1} - \xi_j\right)^{1/2}} + q_i \sqrt{\Delta\xi}\right) + T_{b,1}$$

(5.17)

53

$$I_2 = \left(\frac{1}{\pi \rho_2 c_2 u_2 k_2}\right)^{1/2}\left(\frac{k_f}{h}\right)\left(\sum_{j=1}^{i} \omega_j \frac{\left(T_{1,j} - T_{2,j}\right)}{\left(\xi_{i+1} - \xi_j\right)^{1/2}} \Delta\xi + T_i \sqrt{\Delta\xi}\right)$$

$$+ \frac{1}{2}\left(\frac{1}{\pi \rho_2 c_2 u_2 k_2}\right)^{1/2}\left(\sum_{j=1}^{i} \omega_j \frac{q_j \Delta\xi}{\left(\xi_{i+1} - \xi_j\right)^{1/2}} + q_i \sqrt{\Delta\xi}\right) + T_{b,2} \qquad (5.18)$$

$$J_1 = \left(\frac{1}{\pi \rho_1 c_1 u_1 k_1}\right)^{1/2}\left(\frac{k_f}{h}\right)\sqrt{\Delta\xi} \qquad (5.19)$$

$$J_2 = \left(\frac{1}{\pi \rho_2 c_2 u_2 k_2}\right)^{1/2}\left(\frac{k_f}{h}\right)\sqrt{\Delta\xi} \qquad (5.20)$$

$$K_1 = \frac{1}{2}\left(\frac{1}{\pi \rho_1 c_1 u_1 k_1}\right)^{1/2}\sqrt{\Delta\xi} \qquad (5.21)$$

$$K_2 = \frac{1}{2}\left(\frac{1}{\pi \rho_2 c_2 u_2 k_2}\right)^{1/2}\sqrt{\Delta\xi} \qquad (5.22)$$

where $\Delta\xi$ is the grid spacing and ω_j is the quadrature for the numerical integration.

Equation (5.15) and (5.16) combined with Eq. (5.14) form a set of three non-linear algebraic equation which can be solved for $T_{1,i}$ and $T_{2,i}$ and q_i from i equal to 1 to 10. At each grid point, the Newton-Raphson procedure is used to find the three roots of these three equations. Once T_1, T_2 and q are known, the heat flux q_1 and q_2 into the surfaces can be evaluated using Eqs. (5.10) and (5.11) respectively. These numerical calculations are accomplished in a subroutine called FLASH which includes a subroutine called SOLN for solving the non-linear algebraic equations.

54

VI. HEAT DISSAPATION AND EQUILIBRIUM TEMPERATURE

6.1. Introduction

For gear transmissions delivering sizable power the equilibrium temperature on the tooth surface can reach intolerable level even under ordinary conditions. The analysis for this equilibrium surface temperature is important because the dynamic film thickness depends on the viscosity of lubricant which in turn, depends strongly on the equilibrium surface temperature. In addition, other considerations such as the thermal degradation of lubricant, the teeth surface hardness change and life of seals are also affected by this equilibrium temperature level.

This chapter deals mainly with the analysis of the equilibrium surface temperature in a typical wedge of a spur gear subjected to an arbitrarily distributed heat flow on the tooth.

A special three-dimensional finite-element analysis, formulated specially for a more efficient computation for the gear geometry, was developed.

6.2. Thermal Modeling of The Gear System

For a pair of gears meshing at high speeds, the main cooling is usually provided by a mixture of oil mist surrounding the entire gear surface. The whole system is initially at a given reference temperature. It is gradually heated by the sliding friction between gear tooth, until it reaches a steady state distribution after many cycles of rotation. The analysis of the transient temperature history in gears requires a complicated three dimensional time-dependent heat conduction problem. Since one is primarily concerned with the equilibrium temperature distribution, the transient temperature history before the state of equilibrium is reached is of no interest to the present study.

55

For each revolution, the tooth working face of every segment is subjected to an identical heat flux when it is in contact with a mating tooth. The period of heating within each revolution is extremely small compared to the total period of revolution. Thus, at a given point on the tooth facing, the material receives a heat impulse for each revolution. This results into a typical temperature fluctuation shown in Fig. 2.5, where T_b is the equilibrium temperature, and T_f the flash temperature.

The subsequent sections give a detailed treatment of a steady-state heat conduction analysis for a typical wedge subjected to a time-averaged heat distribution along the tooth profile. The similarity of each tooth on gears and the same heating and cooling condition that each tooth experienced lead to the same repeatable temperature distribution within each tooth segment. Therefore, only one tooth segment needs to be considered for the equilibrium temperature analysis.

6.3. Heat Conduction Equation and Boundary Condition for Gears

A typical configuration for a single tooth segment along with the boundary face number are shown on Fig. 6.1 . Let the equilibrium temperature in this segment be denoted as T_b, the equation governing this temperature distribution is the Fourier heat conduction equation,

$$\frac{\partial^2 T_b}{\partial x^2} + \frac{\partial^2 T_b}{\partial y^2} + \frac{\partial^2 T_b}{\partial z^2} = 0 \qquad (6.1)$$
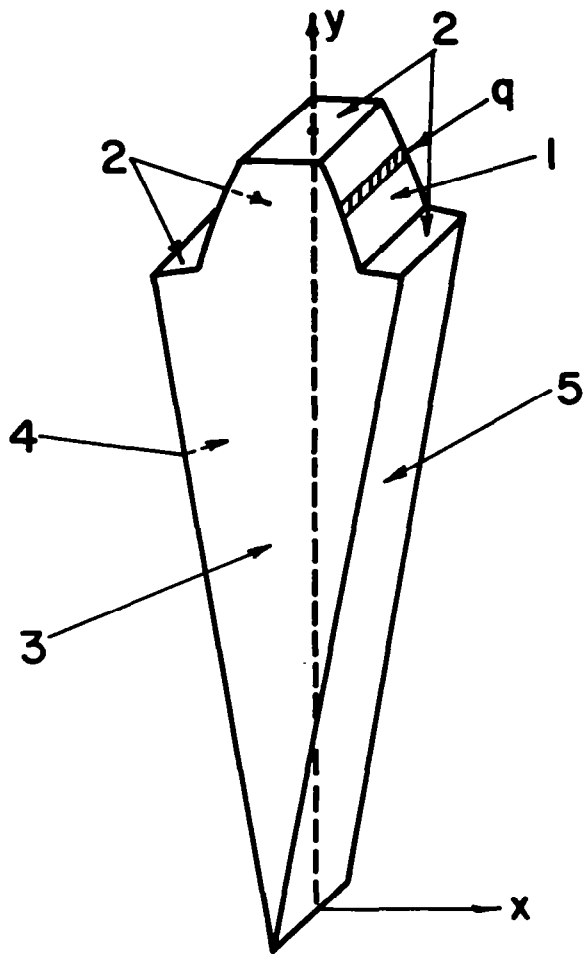
56

Fig. 6.1.   Code Numbers for Surface Boundary Conditions

and the associated boundary conditions referring to the faces on this
segment are

$$T_b)_4 = T_b)_5 \tag{6.2}$$

$$\frac{\partial T_b}{\partial n}\bigg)_4 = -\frac{\partial T_b}{\partial n}\bigg)_5 \tag{6.3}$$

$$\frac{\partial T_b}{\partial n}\bigg)_{2 \text{ and } 3} = -\gamma(T_b - T_a) \tag{6.4}$$

$$\frac{\partial T_b}{\partial n}\bigg)_1 = -\gamma(T_b - T_a) = \left(1 - \frac{\tau}{\Delta}\right) + q_{ave.}(x,y,z) \tag{6.5}$$

where

γ	$= h_s/k$
h_s	= the surface heat transfer coefficient
k	= the thermal conductivity of gear
Δ	= the period of the gear rotation
τ	= the time interval between the pair of teeth in contact
T_a	= the ambient temperature of the surroundings
$q_{ave.}(x,y,z)$	= the local heat flux per unit area averaged over the period of each revolution
n	= a length coordinate in the direction of the outward normal to the surface.

Since the time scale for the surface temperature to reach equilibrium is
several decades larger than the period of each revolution, it is reason-
able to assume a time-average uniform heat flux at each point on the con-
tacting surface even though the real heat input is actually a cyclic impulse.
Moreover, since face 1 is exposed to the ambient most of the time except
for a short instant when it is in contact with the mating tooth, a term
to account for the heat convected to the surrounding is also needed in
the boundary condition, Eq. (6.5)

58

Face 4 and face 5 are boundaries connected to the adjacent and tooth segments. Since the thermal map in every gear segment must be the same for face 4 and face 5, therefore, they must share exactly the same temperature and the same temperature slope. These give rise to boundary conditions given by Eq. (6.2) and (6.3). The non-dimensional form of Eq. (6.1) can be written as

$$\frac{\partial^2 T_b^*}{\partial \bar{x}^2} + \frac{\partial^2 T_b^*}{\partial \bar{y}^2} + c \frac{\partial T_b^*}{\partial \bar{z}^2} = 0 \tag{6.6}$$

The dimensionless quantity

$$T_b^* = \frac{k\left(T_b - T_a\right)}{U_{smax.}P_{max.}}$$

$$\bar{x}, \bar{y}, \bar{z} = \frac{x}{R_o} , \frac{y}{R_o} , \frac{z}{D}$$

$$c = (D/2 R_o)^2$$

$$D = \text{face width}$$

$$R_o = \text{outside radius}$$

$$Q^* = \frac{q_{ave.}R_o}{U_{smax.}P_{max.}}$$

and the boundary condition, become

$$\left.\frac{\partial T_b^*}{\partial N}\right)_1 = \gamma R_o T_b^* \left(1 - \frac{T}{\Delta}\right) + Q^* (\bar{x}, \bar{y}, \bar{z}) \tag{6.7}$$

$$\left.\frac{\partial T_b^*}{\partial N}\right)_2 = - \gamma R_o T_b^* \tag{6.8}$$

$$\left.\frac{\partial T_b^*}{\partial N}\right)_3 = - \gamma D T_b^* \tag{6.9}$$

$$T_b^* \big)_4 = T_b^* \big)_5 \quad \text{and} \quad \left.\frac{\partial T_b^*}{\partial N}\right)_4 = - \left.\frac{\partial T_b^*}{\partial N}\right)_5 \tag{6.10}$$

6.4. Solution for Equilibrium Temperature by Finite Element Method

The purpose of introducing the following special finite-element formulation is partly because of the unusual boundary conditions required and also for the easier connection to other parts of the analysis.

The discretized regions of a typical tooth segment is shown in Fig. 6.2 , where triangular prism elements with plane triangular element in the $\bar{x}$, $\bar{y}$ plane and rectangular element in the $\bar{x}$, $\bar{z}$ plane are used. Accordingly, the temperature T_b^* is approximated by a sum of nodal temperatures weighted by tensor shaping functions $N_i^1(\bar{x},\bar{y})$ and $N_j^2(\bar{z})$.

Thus

$$T_b^*(\bar{x},\bar{y},\bar{z}) = \left(\sum_{i=1}^{m} \sum_{j=1}^{n} N_i^1(\bar{x},\bar{y})\, N_j^2(\bar{z})\, T_{ij}^* \right) \tag{6.11}$$

where superscript 1 denotes the shaping function N on the $\bar{x},\bar{y}$ plane and superscript 2 denotes the function N in the $\bar{z}$-direction. N^1 is a standard linear shaping function in $\bar{x}$ and $\bar{y}$, and N^2 is a quadratic function in $\bar{z}$. Subscript i denotes the node number on the $\bar{x},\bar{y}$ plane, and j represents the number in the $\bar{z}$ direction. Similarly, the heating input over face 1 is also expressed as functions of nodal heating Q_{ij}^*.

$$Q^*(\bar{x},\bar{y},\bar{z}) = \sum_{i=1}^{m} \sum_{j=1}^{n} N_i^1(\bar{x},\bar{y})\, N_j^2(\bar{z})\, Q_{ij}^* \tag{6.12}$$

As shown by Zienkiewicz [38], the Galerkin's approach for forming the integral of the conduction equation with weighting functions $N_i^1 N_j^2$ can be written as,

$$\int_{\bar{z}} \int_{\bar{x},\bar{y}} N_i^1 N_j^2 \left(\frac{\partial^2 T_b^*}{\partial \bar{x}^2} + \frac{\partial^2 T_b^*}{\partial \bar{y}^2} + c\, \frac{\partial^2 T_b^*}{\partial \bar{z}^2} \right) d\bar{x}\,d\bar{y}\,d\bar{z} = 0 \tag{6.13}$$
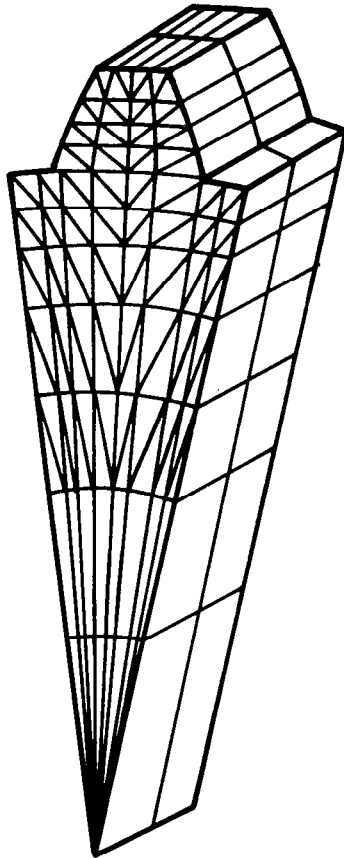
Fig. 6.2.   A Coarse Finite-Element Mesh for the Tooth Segment

$$i = 1, 2, 3, \ldots, m$$

$$j = 1, 2, 3.$$

where m is the total number of nodes in the $\bar{x}, \bar{y}$ plane. Equation (6.13) can be integrated by parts by substituting Eqs. (6.11) for T_b^* and Eqs. (6.7), (6.8), (6.9), and (6.10) for the boundary conditions. Equation (6.13) becomes

$$[A]_{11} \left\{ T_b^* \right\}_{j=1} + [A]_{12} \left\{ T_b^* \right\}_{j=2} + [A]_{13} \left\{ T_b^* \right\}_{j=3} = \{R\}_{j=1} \tag{6.14}$$

$$[A]_{21} \left\{ T_b^* \right\}_{j=1} + [A]_{22} \left\{ T_b^* \right\}_{j=2} + [A]_{23} \left\{ T_b^* \right\}_{j=3} = \{R\}_{j=2} \tag{6.15}$$

$$[A]_{31} \left\{ T_b^* \right\}_{j=1} + [A]_{32} \left\{ T_b^* \right\}_{j=2} + [A]_{33} \left\{ T_b^* \right\}_{j=3} = \{R\}_{j=3} \tag{6.16}$$

and the coefficient matrices are

$$[A]_{11} = \frac{4}{15} [\Omega]_1 + c \left(\frac{7}{6} - rD \right) [\Omega]_2 + \frac{4}{15} \gamma D [\Omega]_3 \tag{6.17}$$

$$[A]_{12} = \frac{2}{15} [\Omega]_1 - \frac{4}{3} c [\Omega]_2 + \frac{2}{15} \gamma D [\Omega]_3 \tag{6.18}$$

$$[A]_{13} = - \frac{1}{15} [\Omega]_1 + \frac{1}{6} c [\Omega]_2 - \frac{1}{15} \gamma D [\Omega]_3 \tag{6.19}$$

$$[A]_{21} = [A]_{12} \tag{6.20}$$

$$[A]_{22} = \frac{16}{15} [\Omega]_1 + \frac{8}{3} c [\Omega]_2 + \frac{6}{15} \gamma D [\Omega]_3 \tag{6.21}$$

$$[A]_{23} = [A]_{12}, \qquad [A]_{31} = [A]_{13}, \qquad [A]_{32} = [A]_{23} \tag{6.22}$$

$$[A]_{33} = [A]_{11} \tag{6.23}$$

where the $i\ell^{th}$ coefficient of the matrices, $[\Omega]_1$, $[\Omega]_2$, and $[\Omega]_3$ are

$$\left(\Omega_{i\ell}\right)_1 = \iint \left(\frac{\partial N_i^1}{\partial \bar{x}} \frac{\partial N_\ell^1}{\partial \bar{x}} + \frac{\partial N_i^1}{\partial \bar{y}} \frac{\partial N_\ell^1}{\partial \bar{y}}\right) d\bar{x}d\bar{y} \qquad (6.24)$$

$$\left(\Omega_{i\ell}\right)_2 = \iint N_i^1 N_\ell^1 \, d\bar{x}d\bar{y} \qquad (6.25)$$

$$\left(\Omega_{i\ell}\right)_3 = \oint N_i^1 N_\ell^1 \, dS \qquad (6.26)$$

The resulting ith coefficient of the vectors $\{R\}$ in Eq. (6.14) to (6.16) are

$$\left(R_i\right)_{j=1} = \gamma D \sum_\ell \left(\frac{4}{15} \oint N_i^1 N_\ell^1 Q_{\ell,1}^* dS + \frac{1}{3} \oint N_i^1 N_\ell^1 Q_{\ell,2}^* dS\right.$$

$$\left. - \frac{1}{15} \oint N_i^1 N_\ell^1 Q_{\ell,3}^* \, dS \right. \qquad (6.27)$$

$$\left(R_i\right)_{j=2} = \gamma D \sum_\ell \left(\frac{1}{3} \oint N_i^1 N_\ell^1 Q_{\ell,1}^* dS + \frac{16}{15} \oint N_i^1 N_\ell^1 Q_{\ell,2}^* dS\right.$$

$$\frac{2}{15} \oint N_i^1 N_\ell^1 Q_{\ell,3}^* \, dS \bigg) \qquad (6.28)$$

$$\left(R_i\right)_{j=3} = \left(R_i\right)_{j=1} \qquad (6.29)$$

The matrices A are known as the global stiffness matrix and they are formed by summing the contributions from each non-zero element stiffness matrix. The boundary conditions on face 4 and 5 are resolved by adding the boundary element stiffness by the corresponding boundary element stiffness on the opposite side.

Since the heat generated in the contact is in general symmetric with respect to the mid-plane of the gear, the temperature distribution is, therefore, also symmetric. Because of the symmetry, Eqs. (6.14) to (6.16) can be further simplified by virtue of the fact that

63

$$\left\{T_b^*\right\}_{j=1} = \left\{T_b^*\right\}_{j=3} \qquad (6.30)$$

Thus Eqs. (6.14) to (6.16) can be reduced to

$$\left[[A]_{11} + [A]_{13}\right]\left\{T_b^*\right\}_{j=1} + [A]_{12}\left\{T_b^*\right\}_{j=2} = \{R\}_{j=1} \qquad (6.31)$$

$$2 \cdot [A]_{12}\left\{T_b^*\right\}_{j=1} + [A]_{22}\left\{T_b^*\right\}_{j=2} = \{R\}_{j=2} \qquad (6.32)$$

and finally

$$\left\{T_b^*\right\}_{j=2} = [\overline{C}]\,\{R\}_{j=1} - [\overline{B}]\,\{R\}_{j=2} \qquad (6.33)$$

where

$$[\overline{C}] = \left[[A]_{12} - \frac{1}{2}\left[[A]_{11} + [A]_{13}\right]\left[[A]_{12}^{-1}\,[A]_{22}\right]\right]^{-1}$$

and

$$[\overline{B}] = \frac{1}{2}\,[\overline{C}]\left[[A]_{11} + [A]_{13}\right][A]_{12}^{-1}$$

Assuming that the heating is uniform across the width, of the tooth, then

$$\{R\}_{j=1} = \frac{8}{19}\,\{R\}_{j=2} \qquad (6.34)$$

It follows that

$$\left\{T_b^*\right\}_{j=2} = [\overline{D}]\,\{R\}_{j=2} \qquad (6.35)$$

where

$$[\overline{D}] = \frac{8}{19}\,[\overline{C}] - [\overline{B}]$$

Equation (6.35) represents the solution of the temperature distribution at all nodes within a typical tooth segment. However, in the actual problem one is concerned with the temperature along the contacting path only. Moreover, the heat flux at the nodes is zero everywhere except the nodes along the contacting path. Thus, one is only interested in the temperature at the nodes along the contacting path due to heating at the surface nodes, and it is only necessary to use a subset of the inverted solution given by Eq. (6.35).

Let $\{T_b^*\}_{j=2}^S$ denotes a subset of $\{T_b^*\}_{j=2}$ and contain all nodal temperatures along the contacting surface. The corresponding set of heat flux at the same nodes is denoted by $\{R\}_{j=2}^S$. Thus

$$\left\{T_b^*\right\}_{j=2}^S = [\bar{D}]^S \{R\}_{j=2}^S \tag{6.36}$$

where the matrix $[\bar{D}]^S$ is a subset of $[\bar{D}]$ pertaining only to the nodes along the contacting surface. Physically, the elements $\bar{D}_{ij}$ in $[\bar{D}]^S$ can be interpreted as the influence coefficient ij, or the temperature at ith node due to a unit heat flux at jth node.

The influence coefficients $\bar{D}_{ij}$ were found to be dependent only upon the gear geometry, surface convective coefficient, and thermal conductivity of the solid. In terms of dimensionless parameters, the values of $\bar{D}_{ij}$ were found to be functions of the following parameters:

N_T = number of teeth

$\Lambda_f = R_o/D$ = ratio of radius to face width

$B_i = h_s R_o/k$ = Biot number

A bank of data for the coefficients in the matrix $[\bar{D}]^S$ was generated to cover the following ranges of the above three parameters.

$$50 \quad < N_T < 150$$
$$6 \quad < \Lambda_f < 48$$
$$0.3 \quad < B_i < 3$$

It was found that the variations of these coefficients with all three parameters are quite well-behaved. The results also exhibit a linear relation between D with N_T. These trends suggest that one can readily use a interpolation routine to obtain the values of the influence coefficient matrix for any arbitrary value of N_T, Λ_f, and B_i within the above listed ranges. Since the coefficients depend almost lineraly on N_T, the extra-polation can also be made for $N_T < 50$. This interpolation procedure was accomplished by using the isoparametric mapping scheme suggested by Zienkiawicz (Ref. 38) and it is documented in Appendix A.

VII. COMPUTATIONAL PROCEDURES

In the previous chapters it was shown that the problem of elasto-hydrodynamic lubrication of spur gears consists essentially of the solution of the following quantities along the line of action.

1. Dynamic load $\qquad$ P_d

2. Film thickness $\qquad$ h

3. Total flash temperature $\qquad$ $T_{1,2}$

4. Equilibrium surface temperature $\qquad$ $T_{b_{1,2}}$

Since the dynamic load is practically unaffected by the film thickness or the surface temperature, it can be solved independently. The remaining three quantities are coupled, and are solved by an iterative process. The overall computational scheme can be best described by a flow diagram shown in Fig. 7.1. This is used in constructing a computer program entitled TELSGE - Thermal Elastohydrodynamic Lubrication of Spur Gears. The function of each subroutine is described as follows.

1. The scheme begins with subroutine INPU which enters all input data including gear geometry, material properties, lubricant properties, and operating conditions such as speed, load, and ambient temperature.

2. The program then excutes subroutine PICK and subroutine INVGEN which are used to obtain the matrix of influence coefficients, the matrix $[\overline{D}]^S$ in Eq. (6.36), for calculating the equilibrium surface temperature distribution along the contacting profile. This is achieved by interpolation of a stored data bank of influenced coefficients.

3. After INVGEN, the program executes subroutine COGEN which is used to generate the coordinates of a mesh of quadrilateral elements in a typical gear segment.
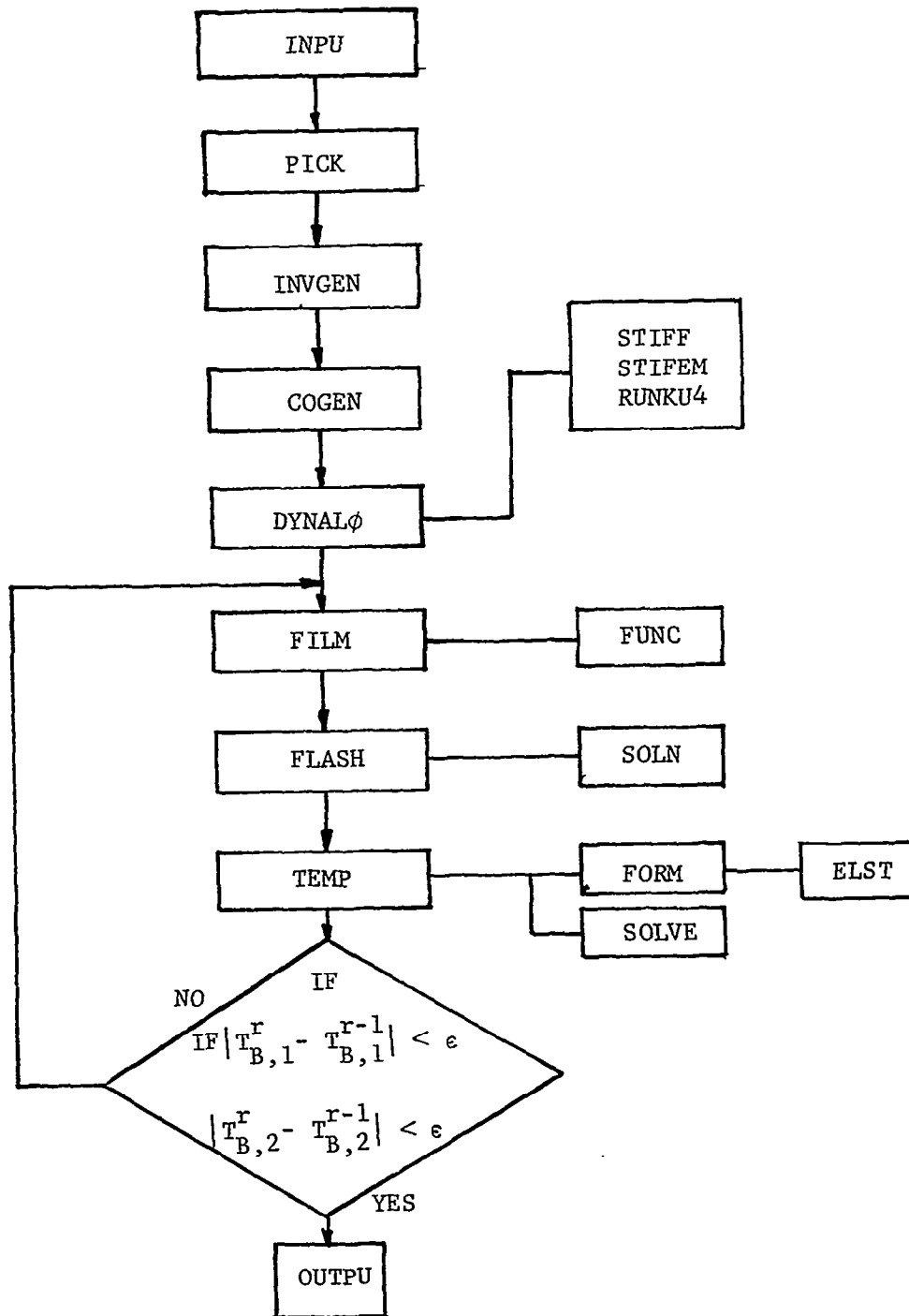
Fig. 7.1.   Flow Diagram

4. Subroutine DYNALO is then executed, and it computes the dynamic load by integrating Eq. (3.21).

5. The program then begins the iterative loop to solve for the flash temperature, and the equilibrium surface temperature. Subroutines FILM is first executed, and it calculates the film thickness by integrating Eq. (4.9).

6. The flash temperature on each contacting surface and the heat flux distribution are determined in subroutine FLASH by solving Eqs. (5.14), (5.15), and (5.16), at each grid within the Hertzian contact.

7. In subroutine TEMP, the equilibrium temperature distribution on the contacting surface is computed by using the influence coefficients obtained in subroutine INVGEN for the distribution of the heat flux calculated in surboutine FLASH. The newly iterated values of equilibrium temperature are compared with the values in the last iteration. If the difference at every node on the surface is within the allowable error, the iteration is considered to be converged. If not, the procedure is repeated at subroutine FILM.

8. Subroutine OUTPU prints out all the output data of the dynamic load, film thickness, flash temperature, and the equilibrium surface temperature along the contacting path.

VIII   RESULTS AND DISCUSSIONS

8.1. Introduction

An analysis of gear dynamics, lubricant film thickness, equilibrium temperature, and flash temperature was developed in Chapters II, III, IV, V, and VI. The numerical procedures developed for this analysis are detailed in Chapter VII. Series of solutions were obtained to simulate gears of different gear ratio, diametral pitch, face width and sub- jected to wide ranges of operating conditions, and these results are presented here in three parts. The first of these concerns the dynamic load only. The dynamic load distribution is plotted as a function of the contact position along the line of action for speeds below, near or above the resonance frequency of the system. The effect of tip relief as well as the effect of profile errors of the teeth on the dynamic load distribution were also examined and included in the presentation. Dynamic response is expressed by a dynamic load ratio defined as the ratio of the maximum dynamic load along the contacting path to the static load. Their ratio is plotted as a function of speed with the damping ratio and the contact ratio as parameters.

The second part concerns the lubrication performance, the distribu- tion of equilibrium temperature, film thickness, and total flash temperature along the contacting path for gears operating at speeds below or above the resonance which are shown first. It is then followed by plots of the minimum film thickness and the maximum total flash temperature as functions of width, outside radius, and diametrial pitch. The effect of tip relief on the lubrication performance is also presented.

The final part of the results contains two design charts for the purpose of estimating the equilibrium temperature on the gear facing for a known distribution of heat flux and convective heat transfer coefficient.

8.2. Gear Dynamics

8.2.1. Dynamic Load Variation

In general, the dynamic load distribution deviates drastically from the static load distribution and is found to change greatly with the operating speed. The relationship of dynamic load variation with speed as well as with gear geometrical factors are described in the following sections.

For gears with true involute profiles under normal operating conditions, the main excitation to the system originates from the periodical change in teeth stiffness due to the alternating engagement of single and double pairs of teeth. The resulting mode of vibration is therefore dependent on the frequency of this forcing excitation, and hence dependent on the operating speed. Figures 8.1 a.b. and c show dynamic load variation in three different speed regions for a pair of 28-tooth and 8 pitch gears.

In the low speed region where the excitation frequency from the change of stiffness is much lower than the resonanting frequency of the system, the dynamic load response is basically a static load sharing in phase with the stiffness change, superimposed by a oscillatory load at a frequency corresponding to the system's resonanting frequency.

As the speed increases to the neighborhood of the resonance, the typical load response as shown in Fig. 8.1b contains load variations so abrupt that it sometimes can even produce teeth separation. In this speed region, the peak dynamic load is much higher than the input static load and is very likely a source of gear noise and early surface fatigue. Operating in this region is obviously harmful. As the speed increases beyond the frequency of the resonanting frequency, the dynamic load becomes out of phase with the stiffness variation, and it has a much smoother response. The peak of this load response is much reduced, and is smaller than the static load. The shape of this load response, shown in Fig. 8.1c is usually preserved with further speed increase. The dynamic load distribution for gears with an exaggerated tip-relief
(.01 in.)
.025 cm at the same speeds are shown in Figs. 8.2a to 8.2c. As expected the tip-relief causes a delay in starting of the contact and an earlier end of the contact. The results also show that the tip relieved gears have a better load response at speeds below or near the resonating frequency. For very high speeds however, the tip-relieved gears show a peak dynamic load higher than that for gears without tip-relief.

For gears having a sinusoidal profile error with amplitude of
(.0001 in.)
.00025 cm the results of the dynamic load variation are shown in Figs. 8.3a to 8.3c . In these cases, arbitrary errors of the sinusoidal form with
(.0001 in.)
the peak amplitude of .00025 cm are introduced to describe the surface of the pinion tooth. The result of the dynamic load pattern deviates from the original load pattern with the correct involute under the same speed, and the deviation seems to be proportional to the amplitude of errors for all speeds.

DYNAMIC LØAD VARIATION

$n = 1637$ RPM

$\xi_c = .17$

P_d/P_s

X/P_b
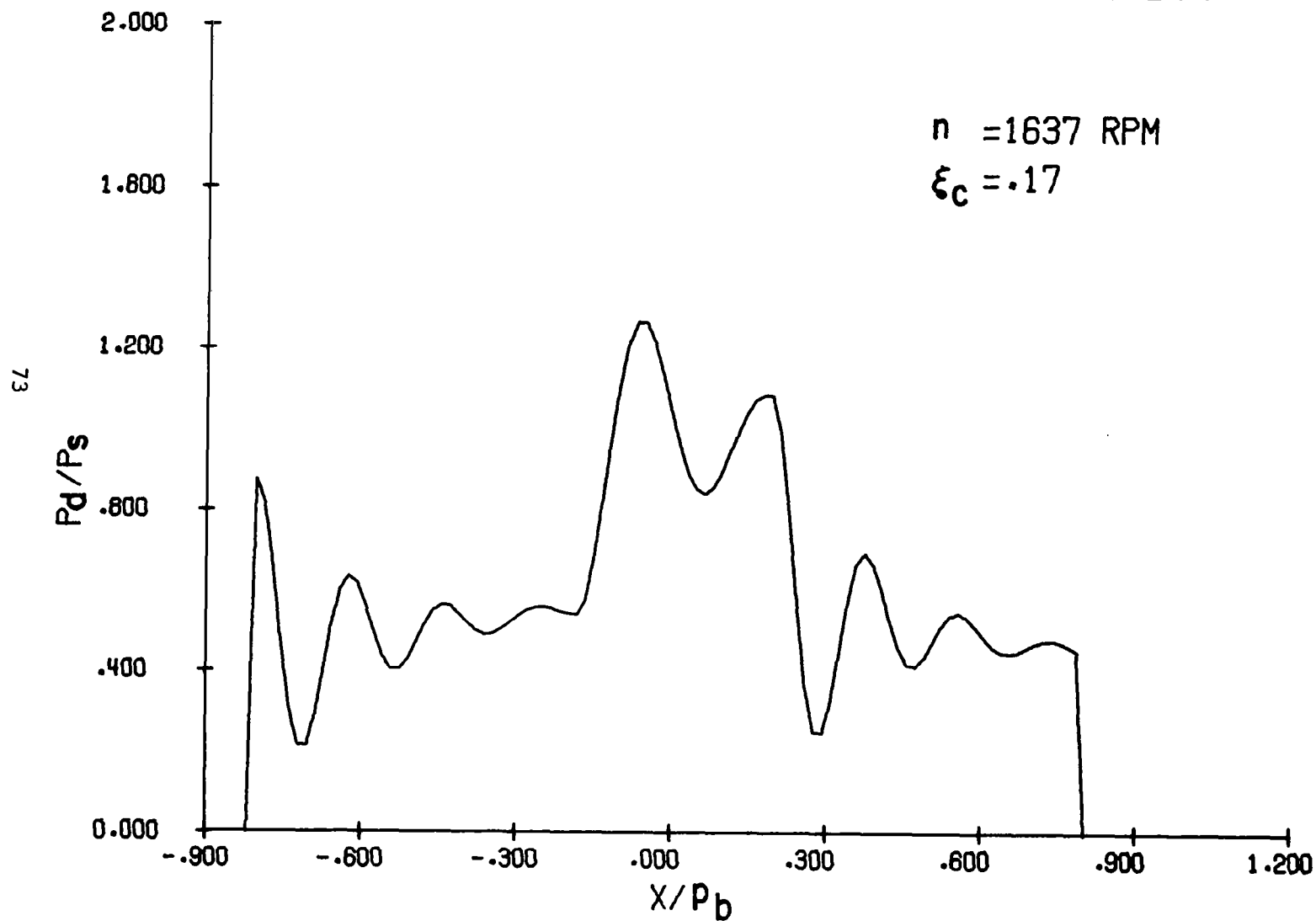
Fig. 8.1. Dynamic Load Variation. $r_G = 1$, $N_T = 28$, $D_p = 8$, $D = 0.254$ cm (0.1 in.)
(a) n = 1637 rpm

DYNAMIC LOAD VARIATION

$n = 7640$ RPM

$\xi_c = .17$
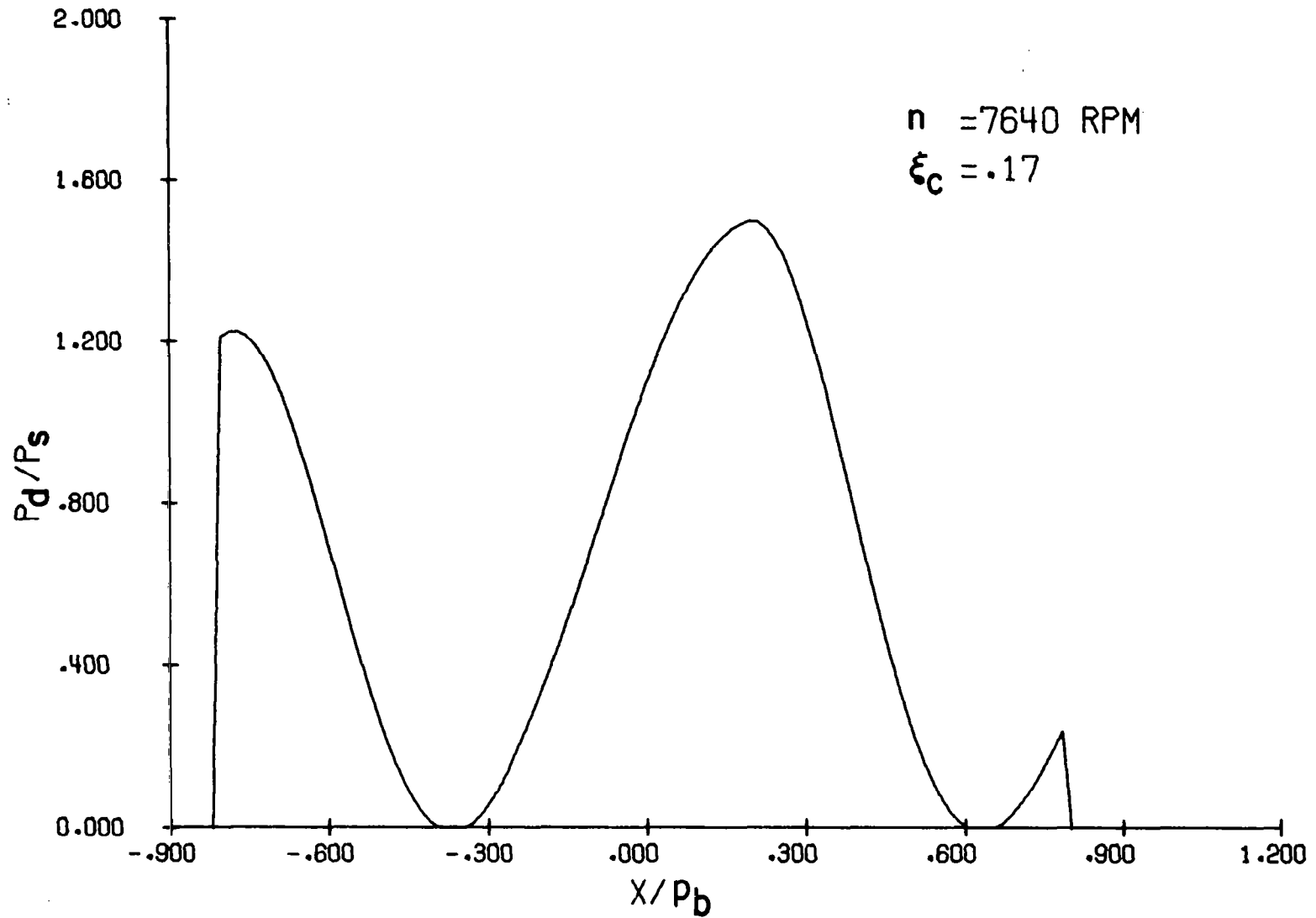
Fig. 8.1.   Continued.   (b) n = 7640 rpm

DYNAMIC LOAD VARIATION

$n = 16370$ RPM

$\xi_c = .17$
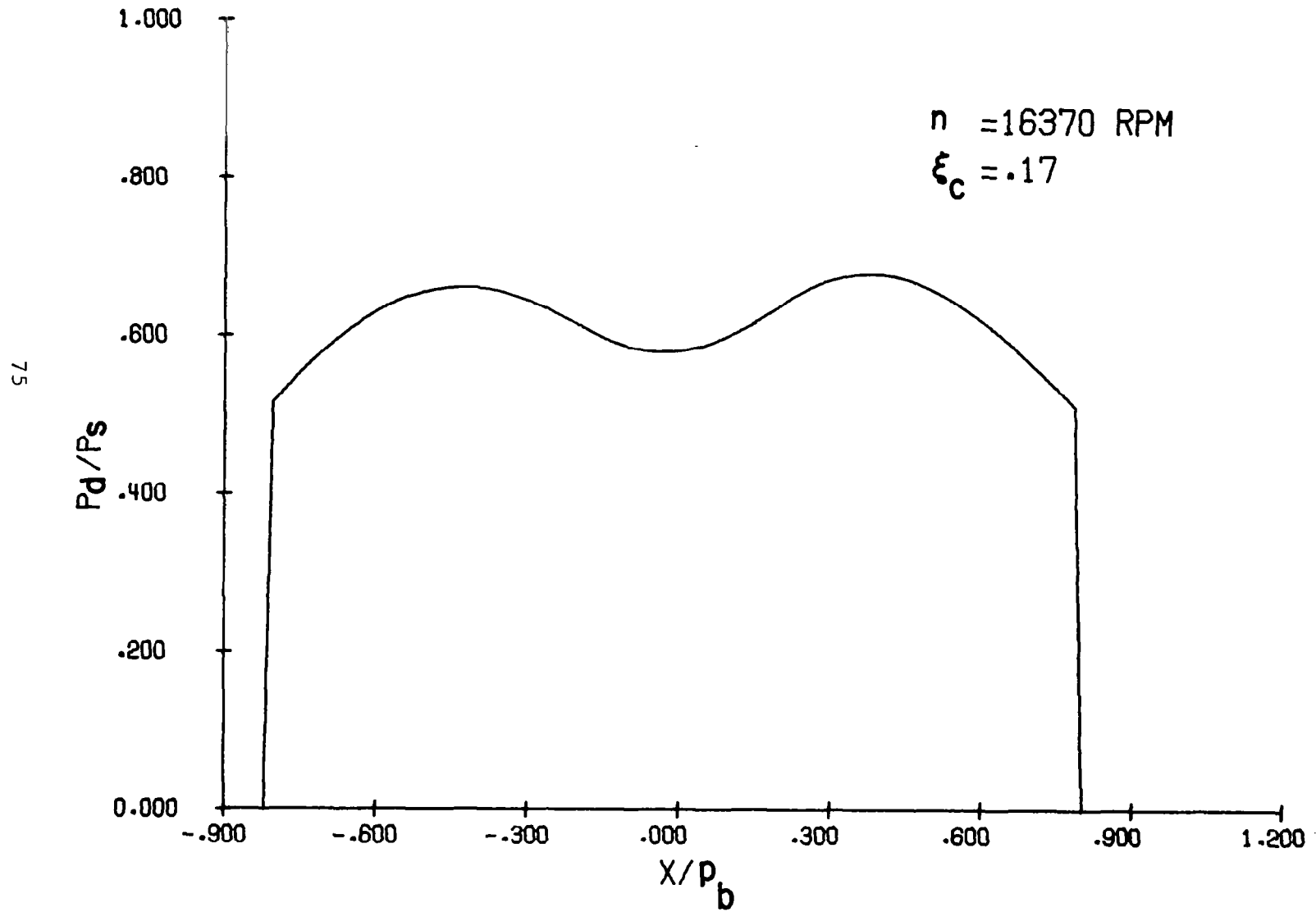
Fig. 8.1.   Concluded.   (c) n = 16 370 rpm

DYNAMIC LOAD VARIATION

WITH .01 IN. TIP-RELIEF

n =1637 RPM

$\xi_c = .17$

P_d / P_s

X/p_b
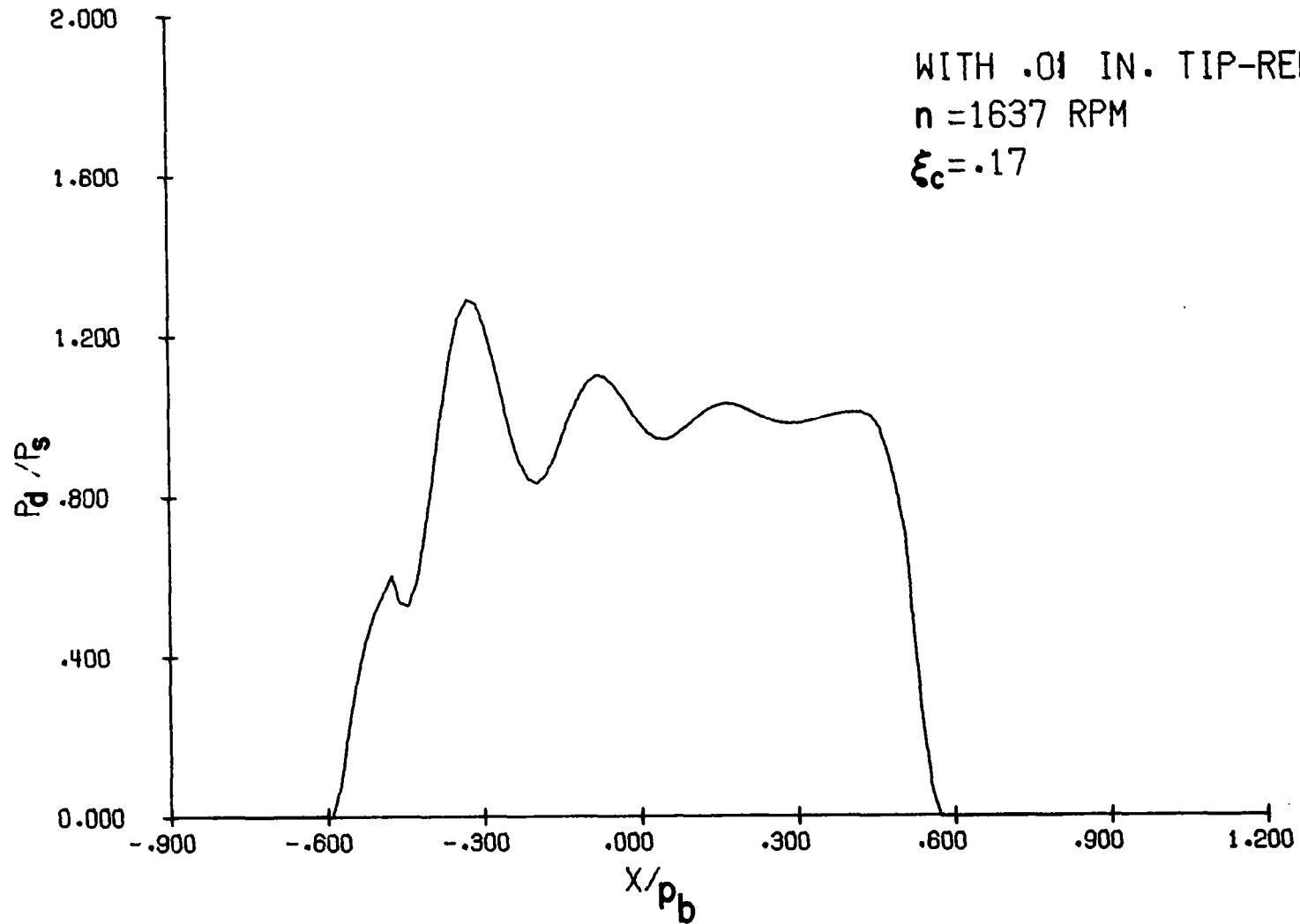
Fig. 8.2.(a) Dynamic Load Variation for Gears with a Large Tip-Relief.
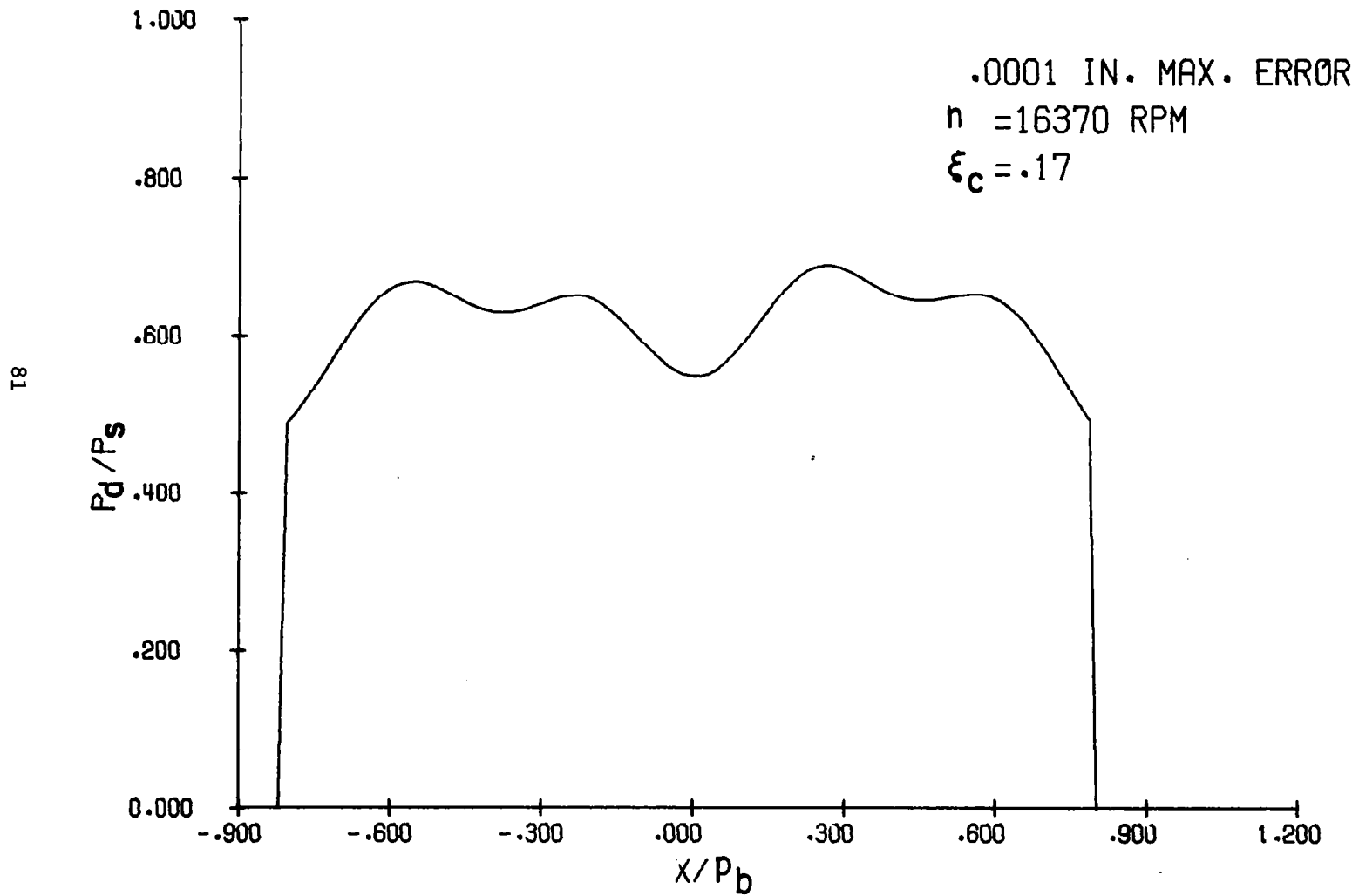Conditions Same as Those in Fig. 8.1.

DYNAMIC LØAD VARIATIØN

WITH .01 IN. TIP-RELIEF
$n = 7640$ RPM
$\xi_c = .17$

P_d / P_s

X/p_b
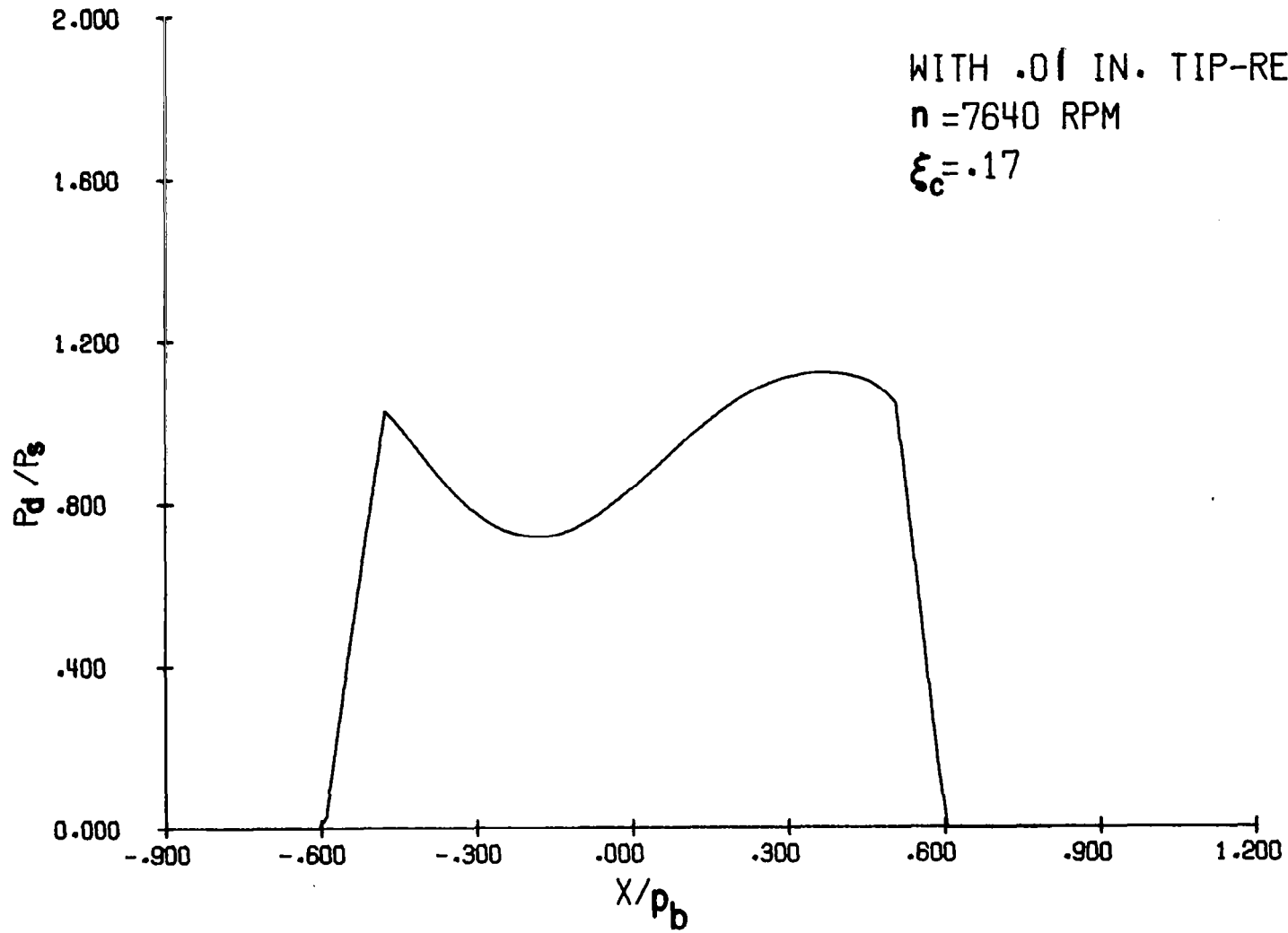
Fig. 8.2.(b) Dynamic Load Variation for Gears with a Large Tip-Relief.
Conditions Same as Those in Fig. 8.1.

77

DYNAMIC LOAD VARIATION
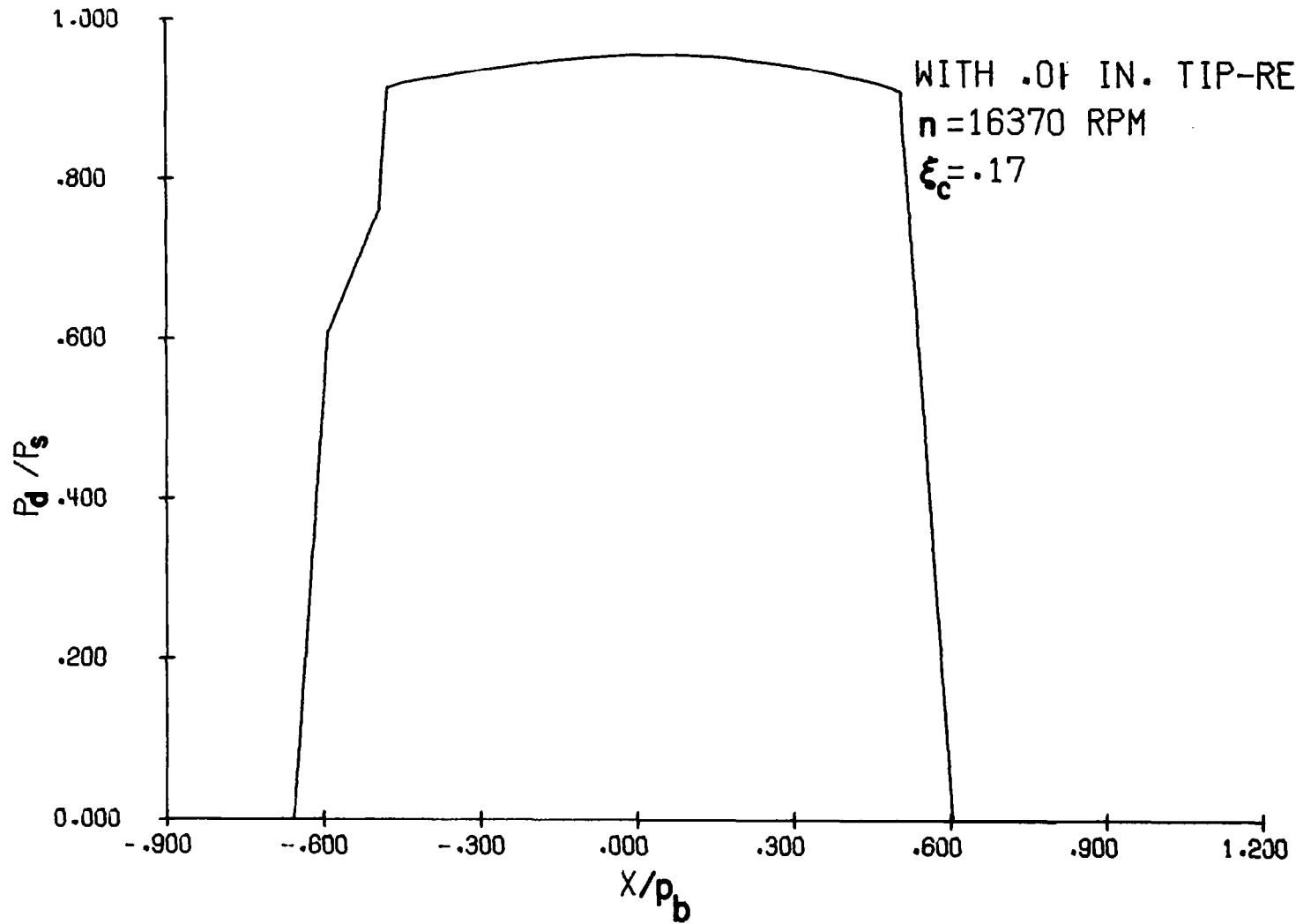
Fig. 8.2.(c) Dynamic Load Variation for Gears with a Large Tip-Relief.
Conditions Same as Those in Fig. 8.1.

DYNAMIC LOAD VARIATION

.0001 IN. MAX. ERROR

n   =1637 RPM
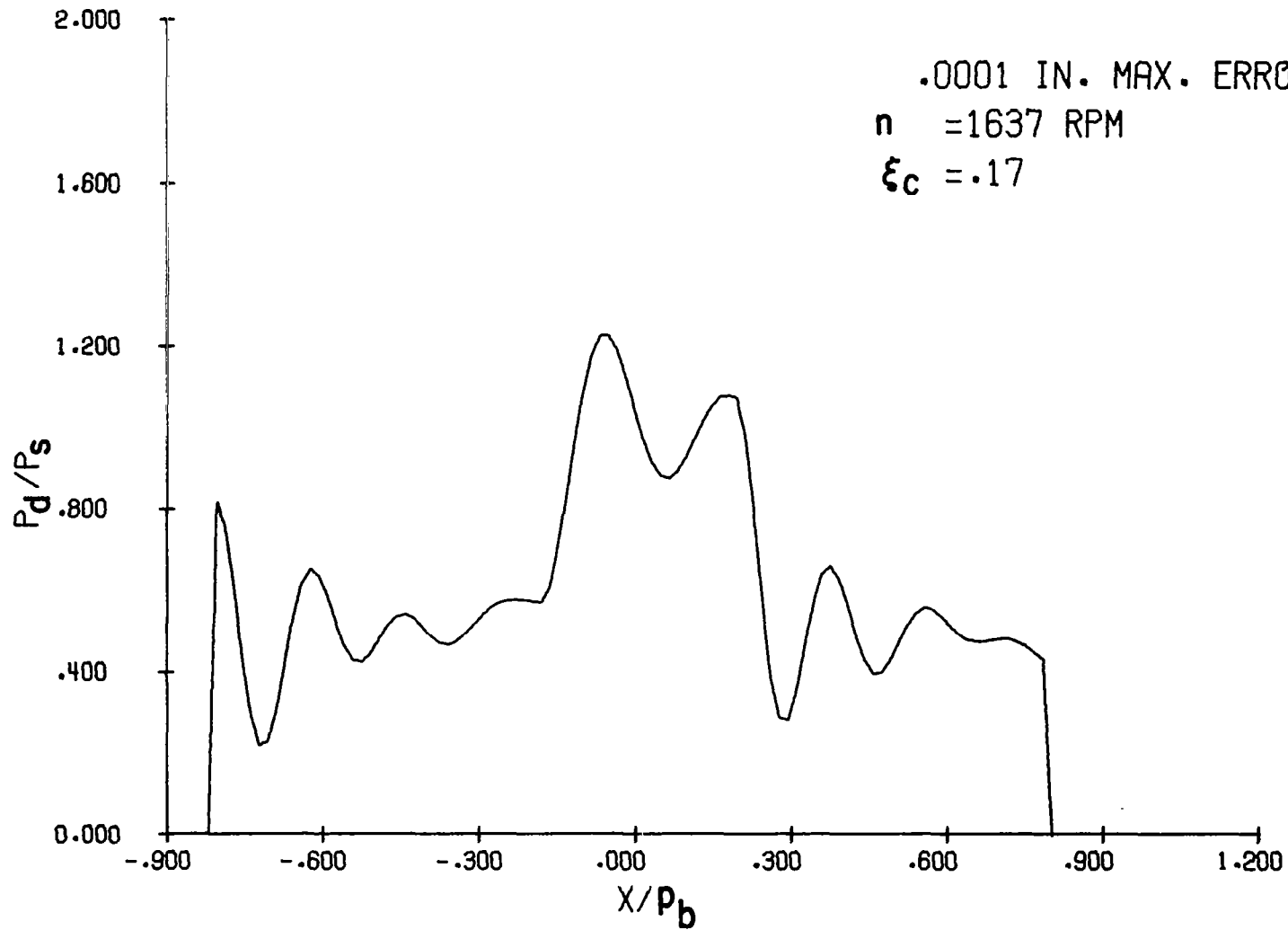
ξ_c =.17

Fig. 8.3.(a) Dynamic Load Variation for Gears with a Small Error Profile.
Conditions Same as Those in Fig. 8.1.

DYNAMIC LOAD VARIATION

.0001 IN. MAX. ERROR

n =7640 RPM

ξ_c =.17

Fig. 8.3.(b) Dynamic Load Variation for Gears with a Small Error Profile.
Conditions Same as Those in Fig. 8.1.

DYNAMIC LOAD VARIATION

.0001 IN. MAX. ERROR

$n = 16370$ RPM

$\xi_c = .17$
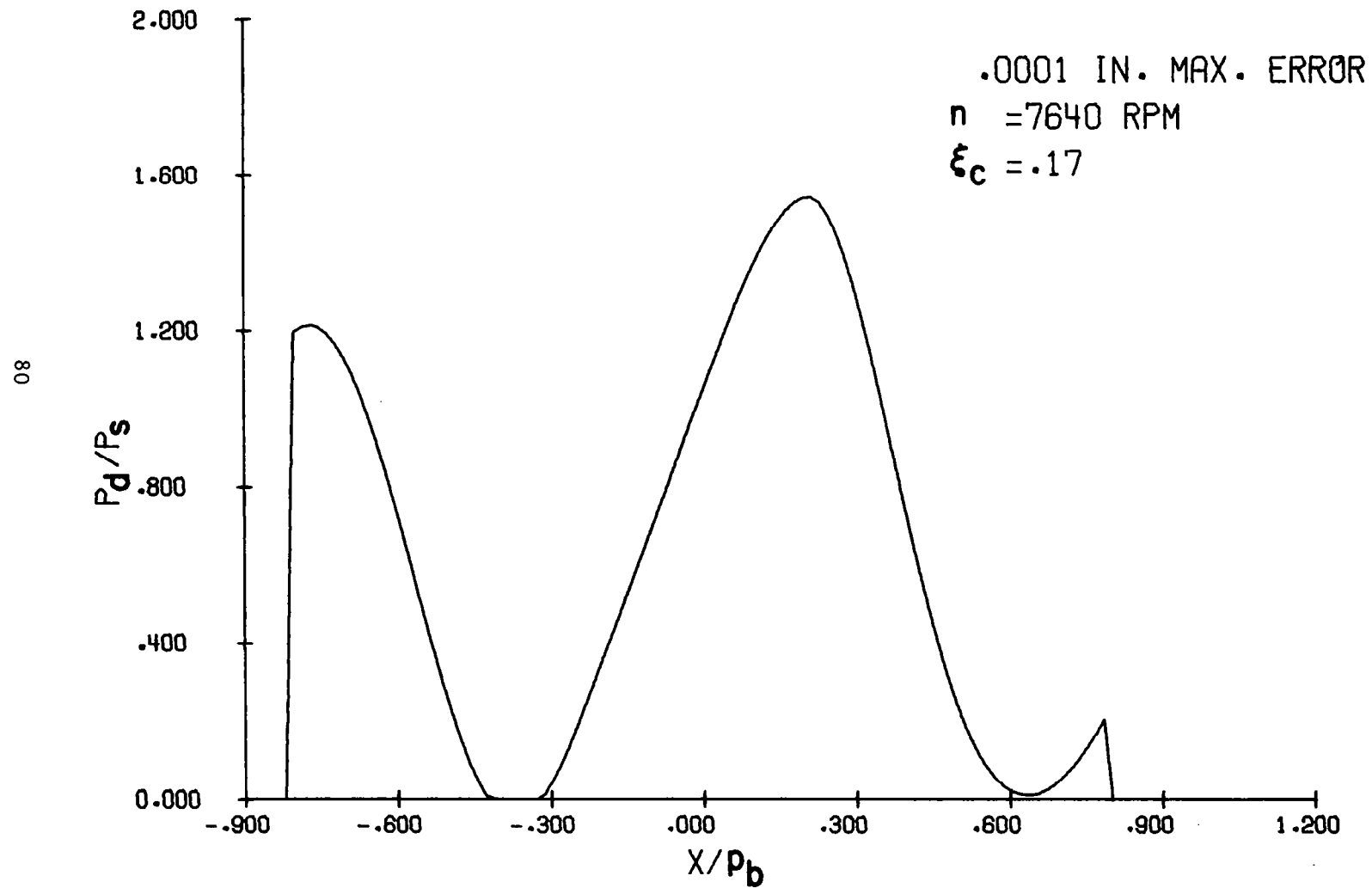
Fig. 8.3.(c) Dynamic Load Variation for Gears with a Small Error Profile.
Conditions Same as Those in Fig. 8.1.

8.2.2 Effect of Speed

One of the approaches to investigate the effects of various parameters on this dynamic load is through the use of dynamic load factor, $P_f = P_{dmax.}/P_s$, where P_s is the static load and $P_{dmax.}$ is the maximum dynamic load along the line of action or the contacting path. The effect of speed is examplified by plotting the dynamic load factor P_f against the frequency ratio $\omega_r = \omega/\omega_n$, defined as the ratio of the excitation frequency ω due to the periodical change of tooth stiffness to the systems natural frequency ω_n. The system natural frequency ω_n is taken as the frequency at which the maximum dynamic load occurs.

Figure 8.4 shows a typical curve of the dynamic load factor P_f versus frequency ratio ω_r. The general trend of the response is similar to that of a single-degree of freedom forced vibratory system except that a few secondary peaks of the dynamic load ratio exist in the region of $\omega_r < 1$. When ω_r approaches unity, the load rises rapidly exhibiting a resonating phenomenon. For speeds above the natural frequency, the dynamic load decreases steadily in the same manner as the ordinary vibratory system.

8.2.3. Effect of Damping Ratio ξ

The damping coefficient C_o in Eq. (3.21) governing the dynamic load variation depends on the viscous friction of the gear system. It is usually an unknown. The damping ratio ξ in the present analysis is defined as $\xi \doteq C_o/2\sqrt{KM}$. An arbitrary value between .1 and .2 was used in the analysis reported by Hirano [Ref. 7] and Ishikawa [Ref. 8] for the correlation between their analytical and experimental results. To explore the effect of this ratio, arbitrary values of .1, .17, and .2 were used to generate the dynamic load ratios shown in Fig. 8.5. As
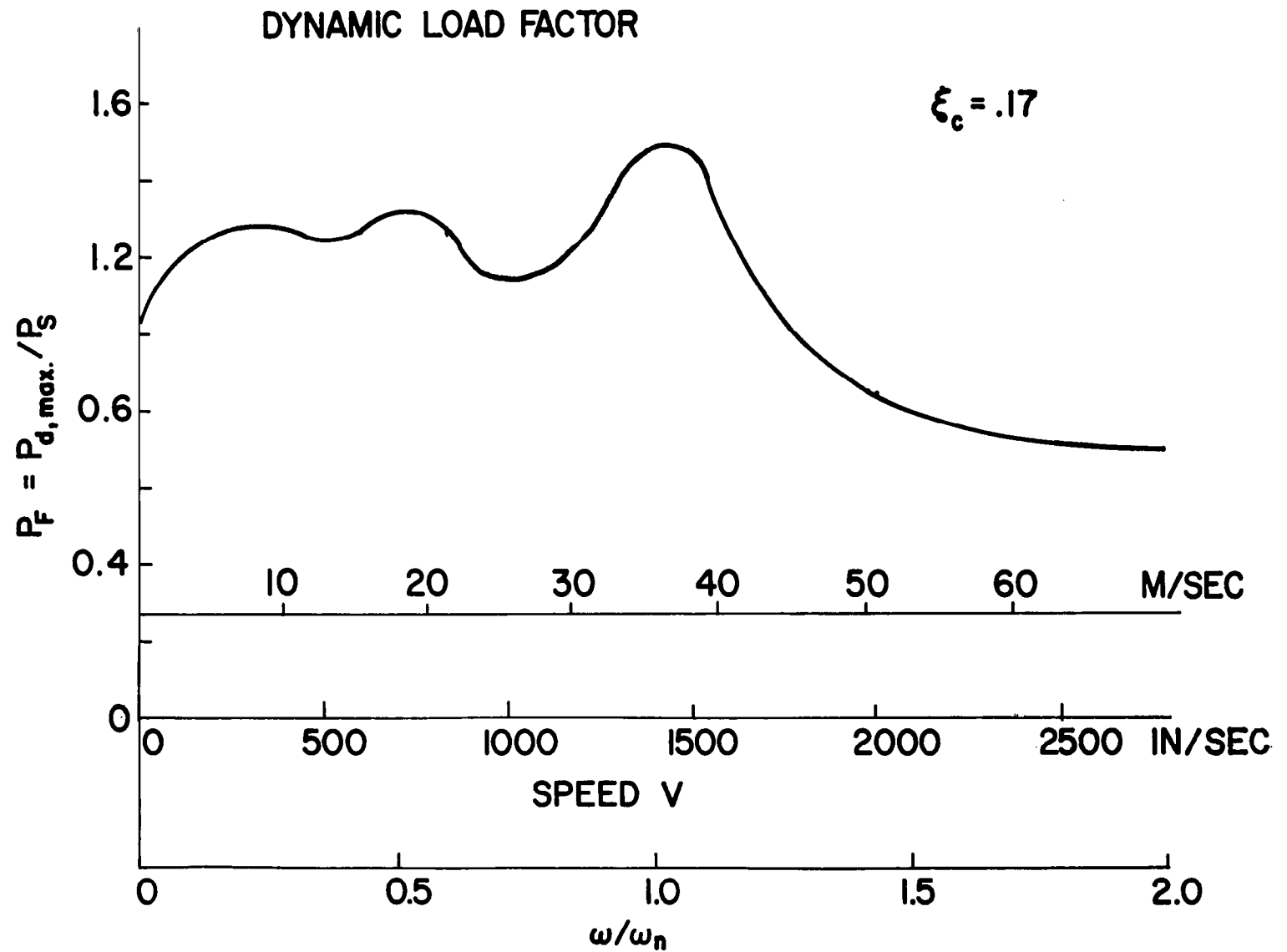
DYNAMIC LOAD FACTOR

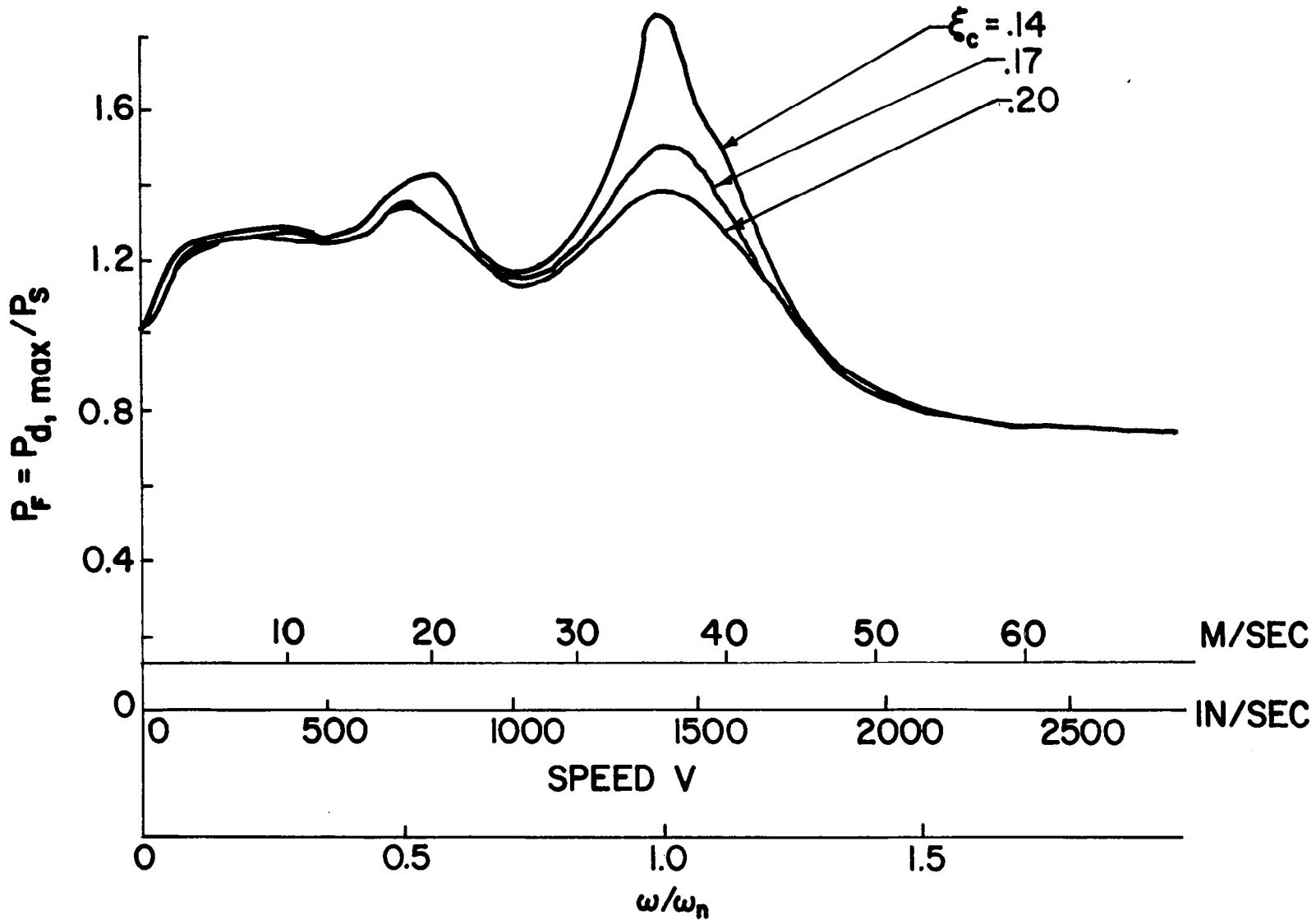Fig. 8.4. Effect of Speed on Dynamic Load Factor. $r_G = 1$, $N_T = 28$, $D_p = 8$, $D = .254$ cm (.1 in.)

Fig. 8.5.   Effect of Damping Ratio on Dynamic Load Factor. r_G= 1,
N_T= 28, D_p= 8, D = .254 cm (.1 in.)

observed in this figure, damping ratio ξ has a major influence on the load factor P_f when the operating speed is close to the resonating frequency. Away from the resonance the damping has little influence on P_f.

8.2.4. Effect of Contact Ratio

Contact ratio is defined as the ratio of the contact length to the base pitch. This ratio measures the duration of load being shared by more than one pair of teeth and it has a considerable effect on the dynamic load response. For gears with different diametral pitches, the dynamic load response is different because of the change in contact ratio. It is expected that an increase in contact ratio would have a beneficial effect on the load sharing. To verify this fact, a comparison of the dynamic load response is made between gears having 8-pitch and 16-pitch under identical operational conditions. The corresponding contact ratios for these two sets of gears are 1.64 and 1.78 respectively. As shown in Fig. 8.6, the fine pitch gears (16-pitch) having a higher contact ratio have a smaller dynamic load factor compared with that calculated for coarser gears.

8.2.5. Effect of Tooth Tip-Relief

The dynamic load factor P_f is also calculated over a wide range of speeds for a pair of 28-tooth, 8-pitch gears both having a maximum of .01 inch removed from the tip of the tooth. Figure 8.7 shows the result of the dynamic load factor P_f comparing with those obtained for the same gears without the tip-relief. It is seen that the tip-relief tends to suppress the peaks over the entire frequency range. The effect is most pronounced at speeds near the resonance. However, for speeds above the

85

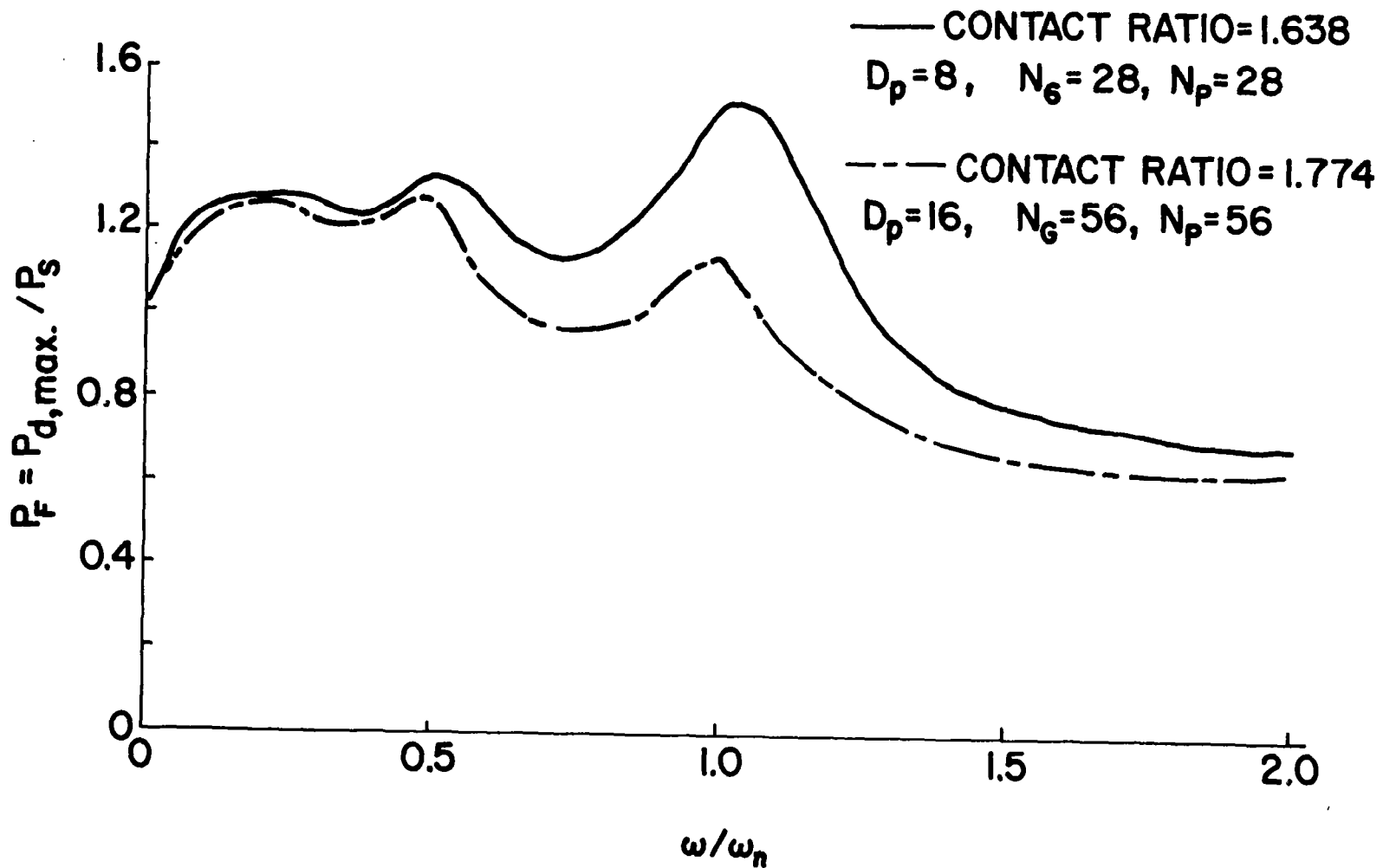# EFFECT OF CONTACT RATIO

Fig. 8.6.   Effect of Contact Ratio on Dynamic Load Factor
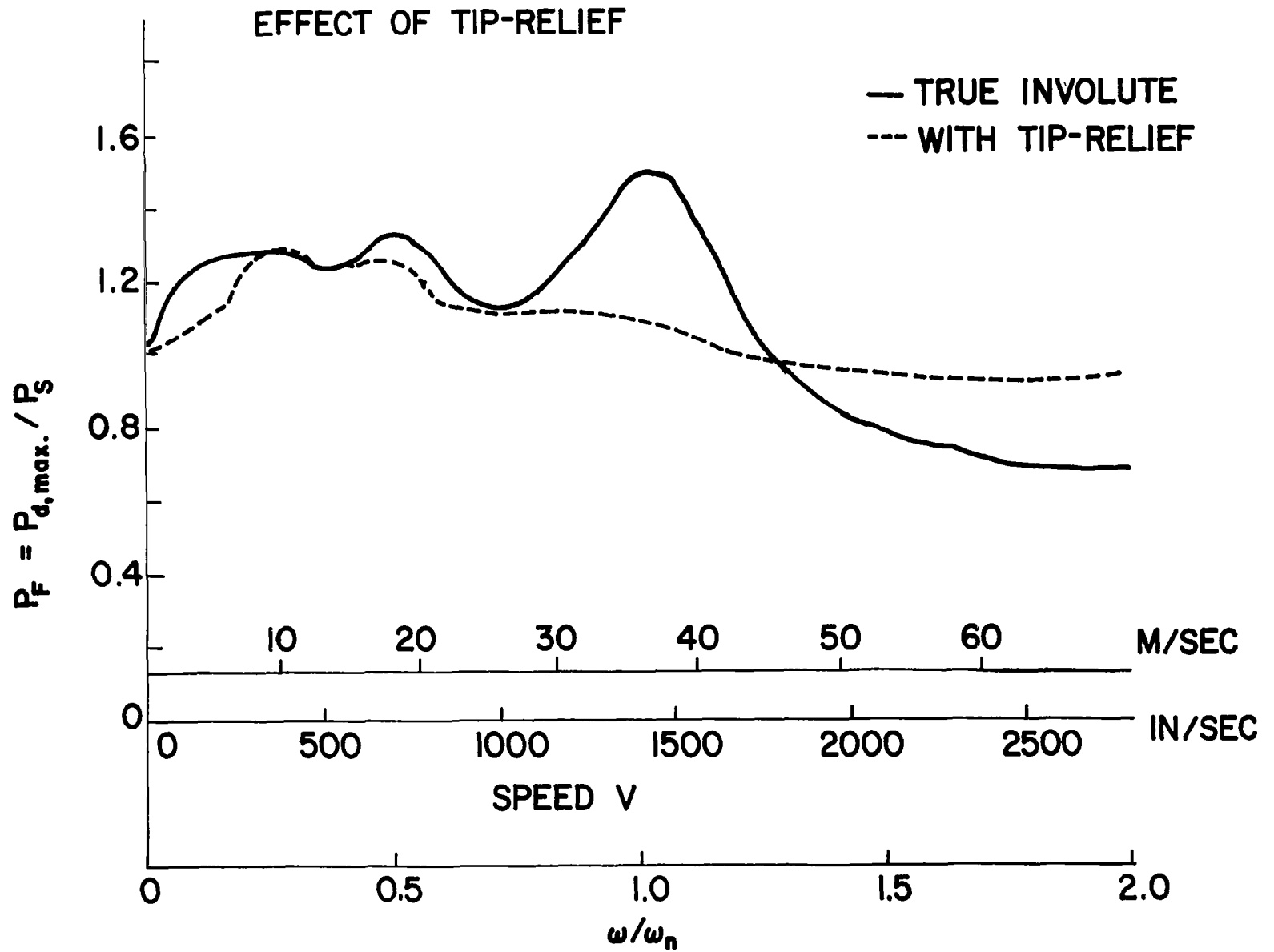
Fig. 8.7.   Effect of Tip-Relief on Dynamic Load Factor.   Conditions same as those
in Fig. 8.4.

resonanting frequency the presence of tip-relief ceases to be beneficial. In fact, the dynamic load factor is higher compared to the factor obtained without the tip-relief.

8.3. Lubrication Performance

8.3.1. Introduction

The computer program developed for spur gears in Chapter VII, is applicable for a wide range of geometric, material, and operating parameters. In this section, typical results were generated for a set of gears having a geometry similar to that used by Townsend [Ref. 24]. These results cover effects of geometrical factors including face width, gear size, diametral pitch, gear ratio and tip-relief. In addition, the effects of lubricant viscosity, heat transfer coefficient, speed, and load on the lubrication performance is also included.

8.3.2. Distribution of Equilibrium Temperature, Total Flash Temperature, and Minimum Film Thickness

In this section, detailed distributions of the minimum film thickness and temperature are plotted against the contact position for a set of gears and the lubricant used in Ref. 24. The properties of the lubricant as well as the geometry of the gears are listed in Table 8.1. In determining the distribution of minimum film thickness, it was assumed that the minimum film in a Hertzian contact is 75% of the plateau film thickness calculated from Eq. (4.9).

A contour plot for the equilibrium temperature distribution in the tooth segment is shown in Fig. 8.8. The temperature is generally higher on the contacting tooth surface and gradually decreases towards

88

TABLE 8.1

GEAR DATA, LUBRICANT DATA, AND STANDARD OPERATING CONDITIONS

GEAR DATA

Number of Teeth,	N_T	28
Diametral Pitch,	D_p	8
Pressure Angle,	ϕ	20°
Pitch Radius,	R_1, cm(in)	4.445 (1.75)
Outside Radius,	R_{o_1}, cm(in)	4.7625(1.875)

LUBRICANT DATA

Super-Refined, Naphthenic, mineral-oil

Kinematic Viscosity, cm^2/sec (cs), at

311 K (100°F)	0.73	(73)
372 K (210°F)	0.077	(7.7)

Density at 289 K (60°F) g/cm^3 0.8899

Thermal Conductivity at

311 K(100°F) J/(m)(sec)(K) (BTU/(hr)(ft)($^{\circ}$F)) 0.04(0.0725)

Specific Heat at 311 K(100°F)

J/(Kg)(K) (BTU/(lb)($^{\circ}$F) 582(0.450)

$$\mu = \mu_o \exp[\alpha p + \beta (\frac{1}{T} - \frac{1}{T_o})]$$

Pressure Viscosity Coefficient, α, m^2/MN(in^2/lb) (.00016)

Temperature Viscosity Coefficient, β, K(R) 3890(7000)

STANDARD OPERATING CONDITIONS

Load Per Unit Width, P, MN/m(lb/in)	.753	(4300)
Pitch Line Velocity, V, m/sec(in/sec)	46.55	(1832)
Ambient Temperature, T_o, C(F)	37.78	(100)
Surface Heat Transfer Coefficient, W/m^2K(B/(ft^2)(hr)(R))	341(60)	
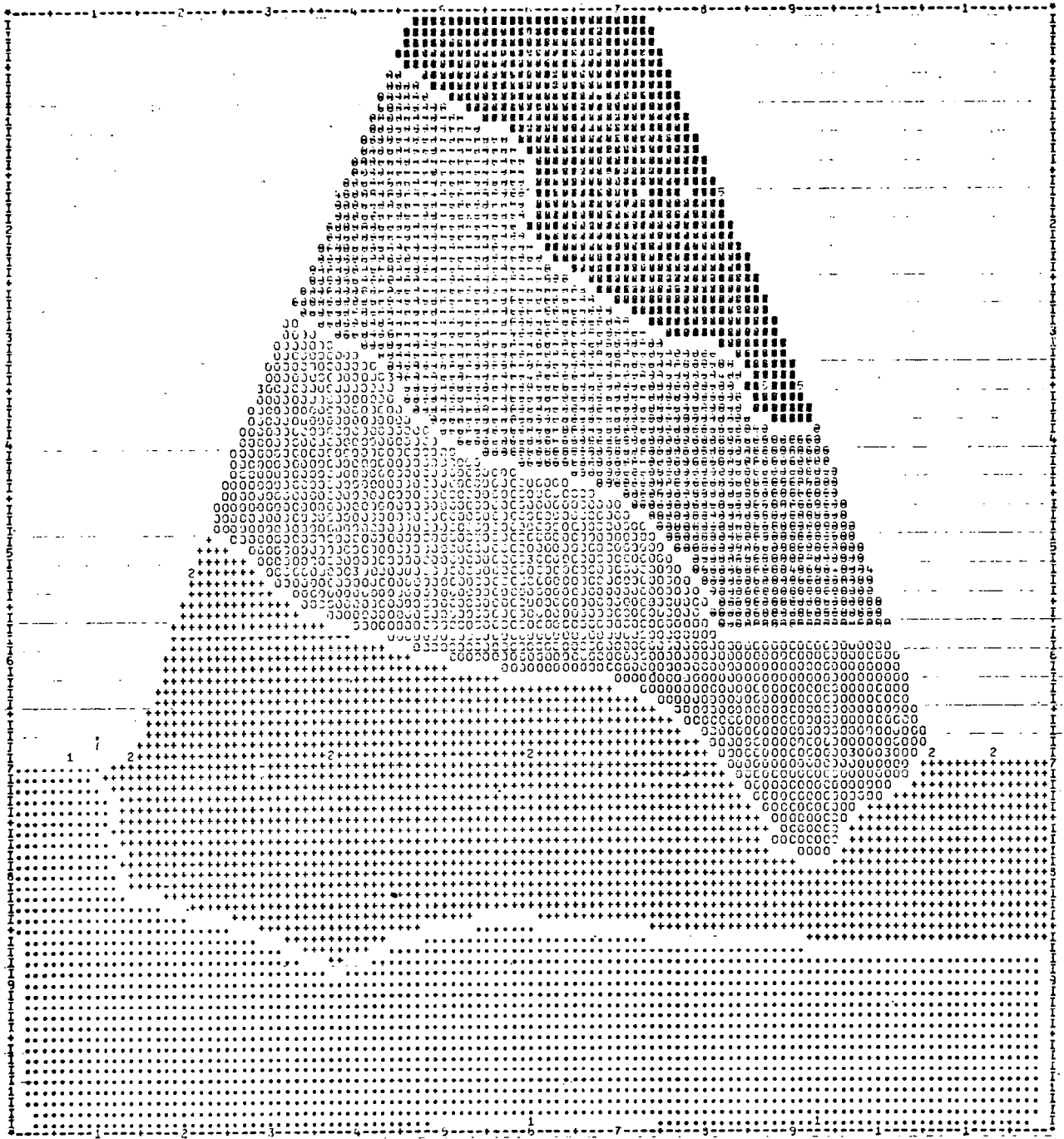
SYMAP
TIME   12.40.43.

N = 62

C   TEMPERATURE ON TWO SIDES FROM GELUT

Fig. 8.8.   A Typical Contour Plot of Equilibrium Surface Temperature
in a Tooth Segment

the interior. On the contacting face, the temperature is highest near the tip of the tooth, and gradually decreases as it approaches the root. The detailed equilibrium surface temperature on both the pinion and gear teeth contacting surfaces is shown in Figs. 8.9(a) to (c) in terms of contact position X. It is seen that the equilibrium temperature for both the pinion and the gear is higher at the tip of the tooth than at the root. This results in a pronounced temperature differential between the tooth surfaces during the beginning and the ending of the engagement.

The total flash temperatures as a function of the contacting position are plotted in Figs. 8.10(a) to (c) for three different speeds. At speeds below or near the resonance, the total flash temperature exhibits local fluctuations which are caused mainly by the dynamic load variations. Such fluctuations of total flash temperature are not found at a speed considerably above the resonance.

Figures 8.11(a) to (c) show the surface temperature within the Hertzian contact for n = 16,370 rpm at three different contact positions. In the beginning of the engagement (Fig. 8.11(a)) the pinion surface velocity, u_1 is slower and, therefore, shows a greater temperature rise. At the end of the contacting path, (Fig. 8.11(c)) the surface velocity of the pinion is faster and, therefore, the trend is reversed.

The corresponding dynamic film thickness for this case is shown in Fig. 8.12 as a function of tooth contact position. The squeeze film effect is shown to be only important at a very short period after the teeth are engaged. Examinations of the film thickness distributions for all other runs indicate that the squeeze film effect is indeed not a dominant effect on the minimum film thickness.
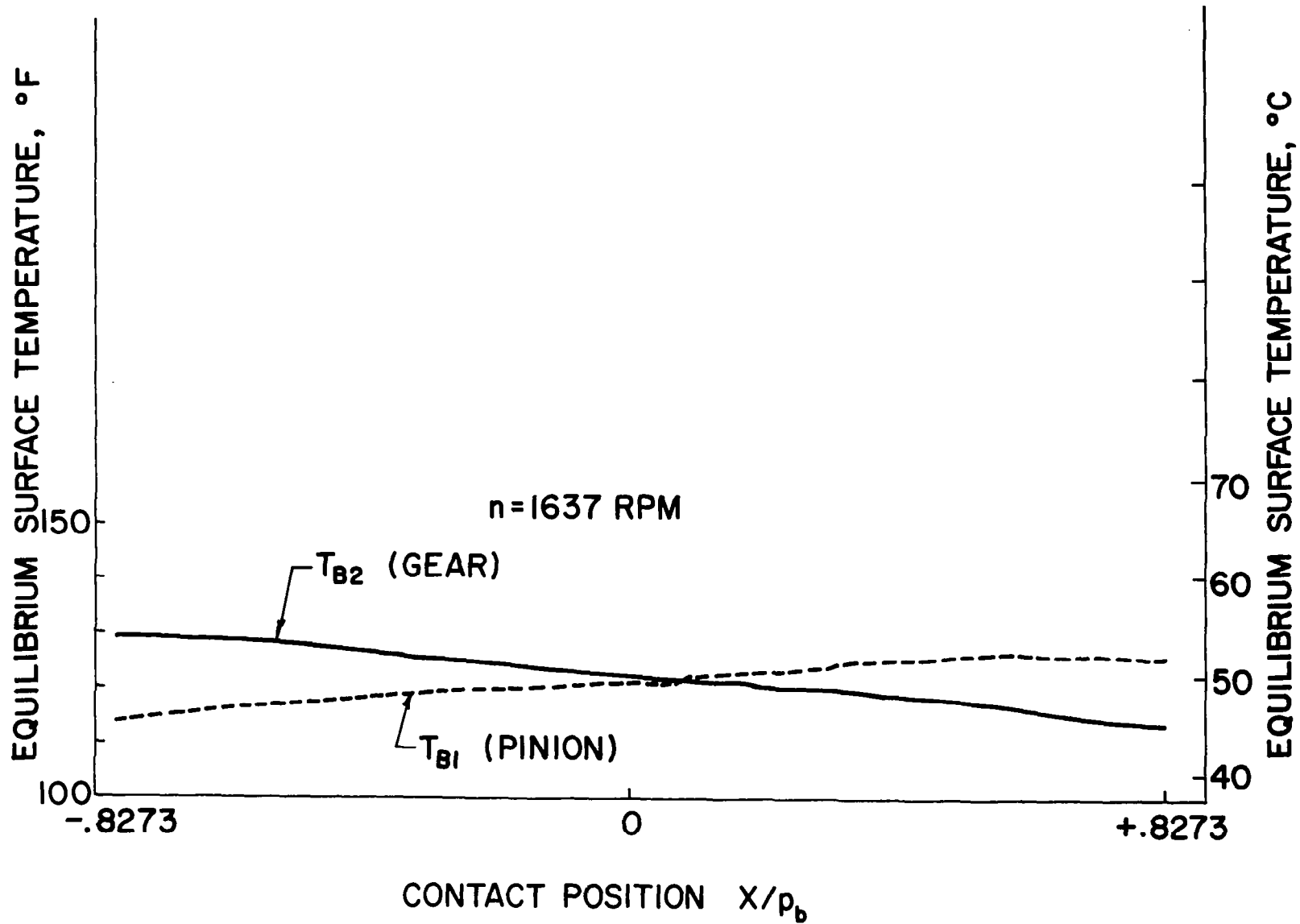
Fig. 8.9(a). Distribution of Equilibrium Surface Temperature, (a) n = 1637 rpm, r_G = 1. Other conditions are listed in Table 8.1.
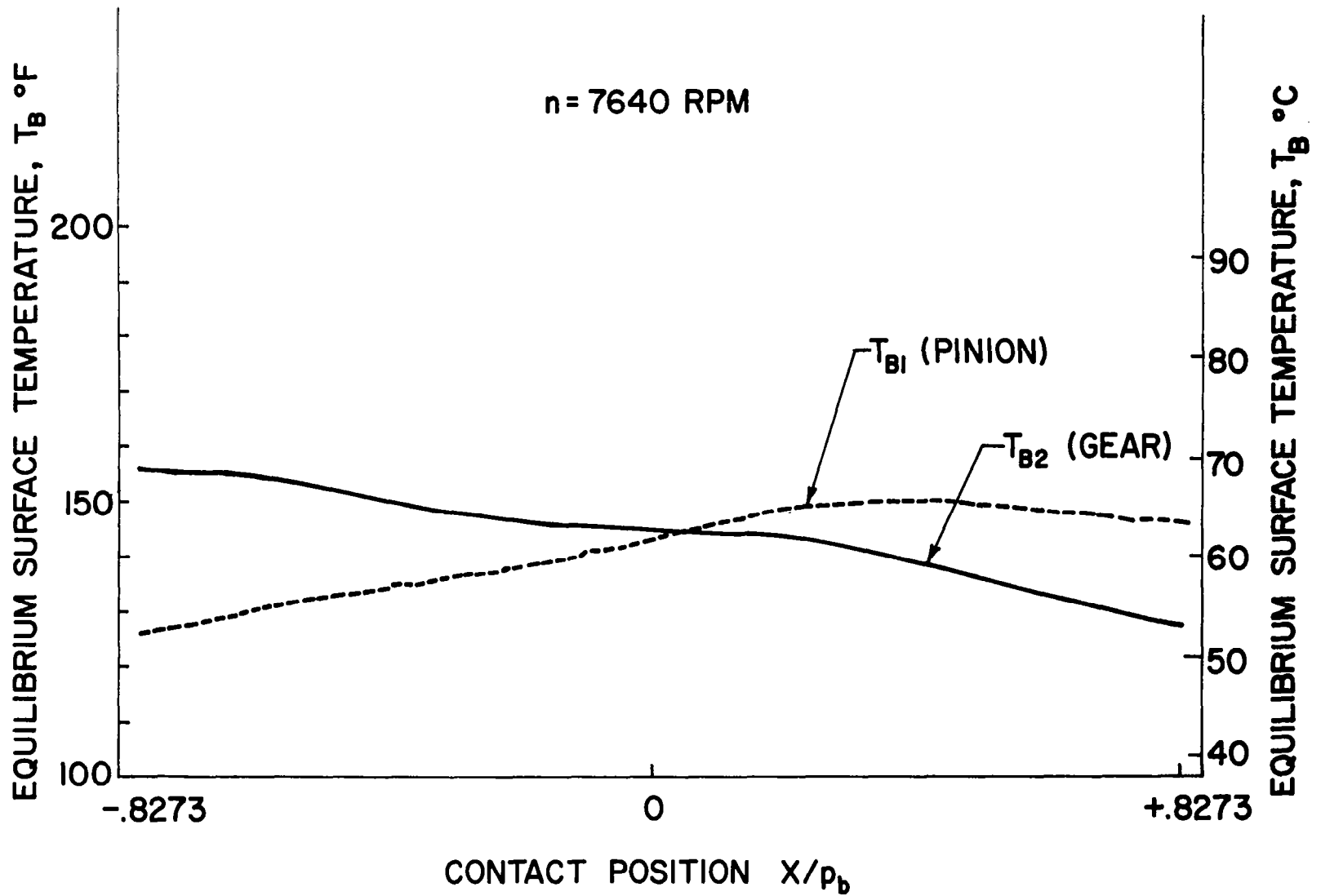
Fig. 8.9(b). Distribution of Equilibrium Surface Temperature, (b) n = 7640 rpm, r_G = 1.
Other conditions are listed in Table 8.1.

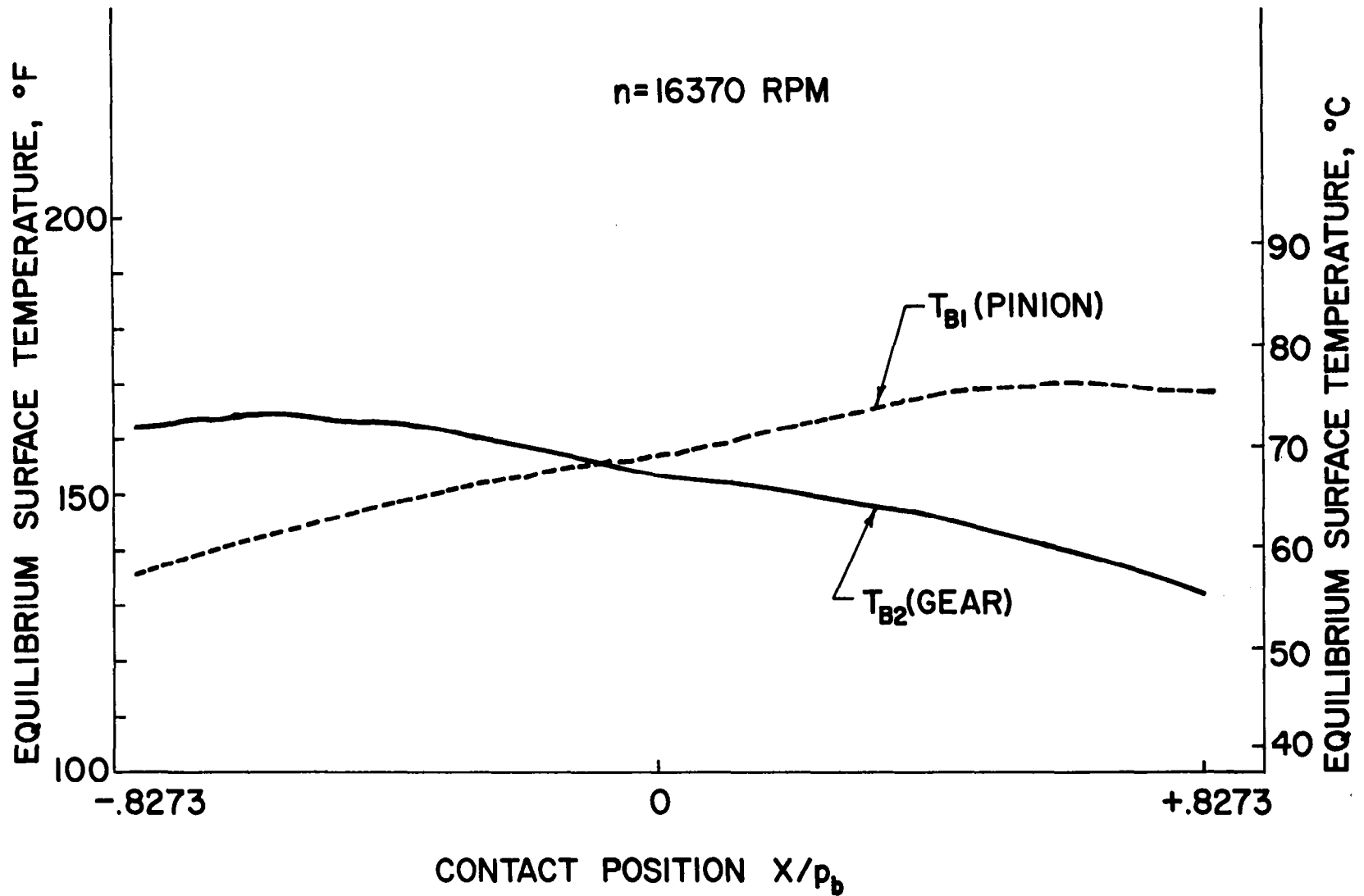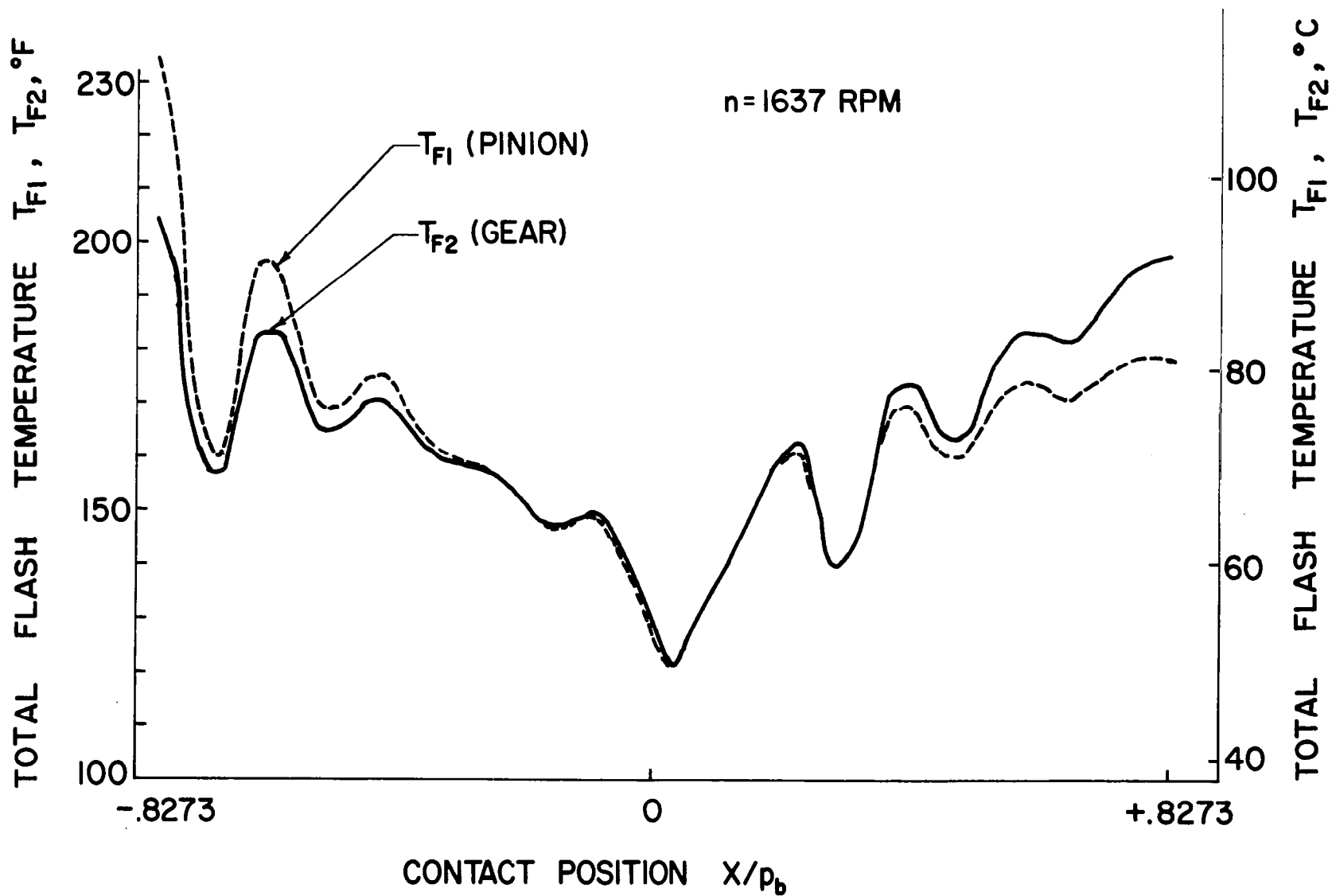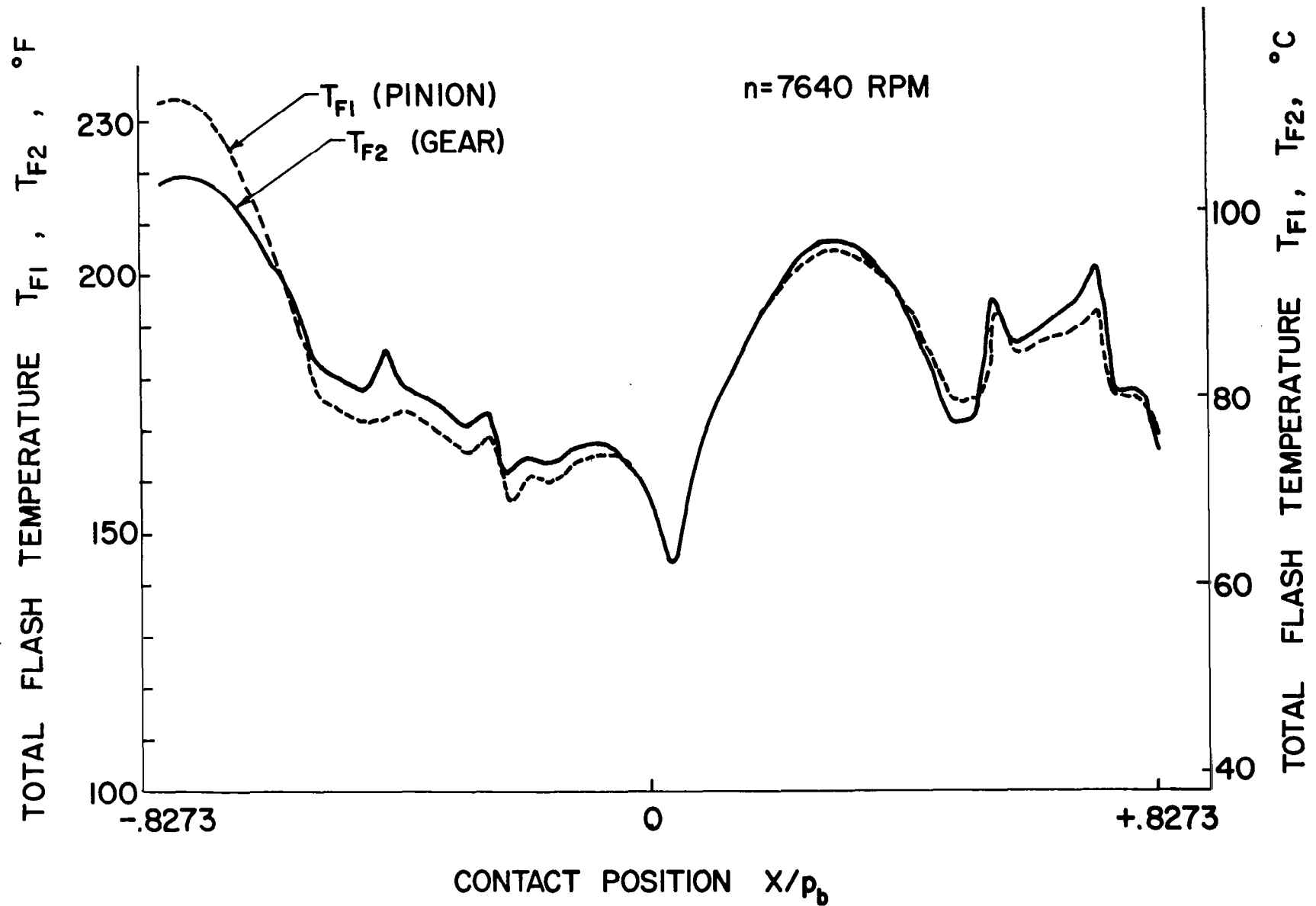Fig. 8.9(c). Distribution of Equilibrium Surface Temperature, (c) n = 16 370 rpm, r_G = 1.
Other conditions are listed in Table 8.1.

Fig. 8.10(a). Distribution of Flash Temperature, (a) n = 1637 rpm, r_G = 1. Other conditions are listed in Table 8.1.

Fig. 8.10(b). Distribution of Flash Temperature, (b) n = 7640 rpm, r_G = 1. Other conditions are listed in Table 8.1.

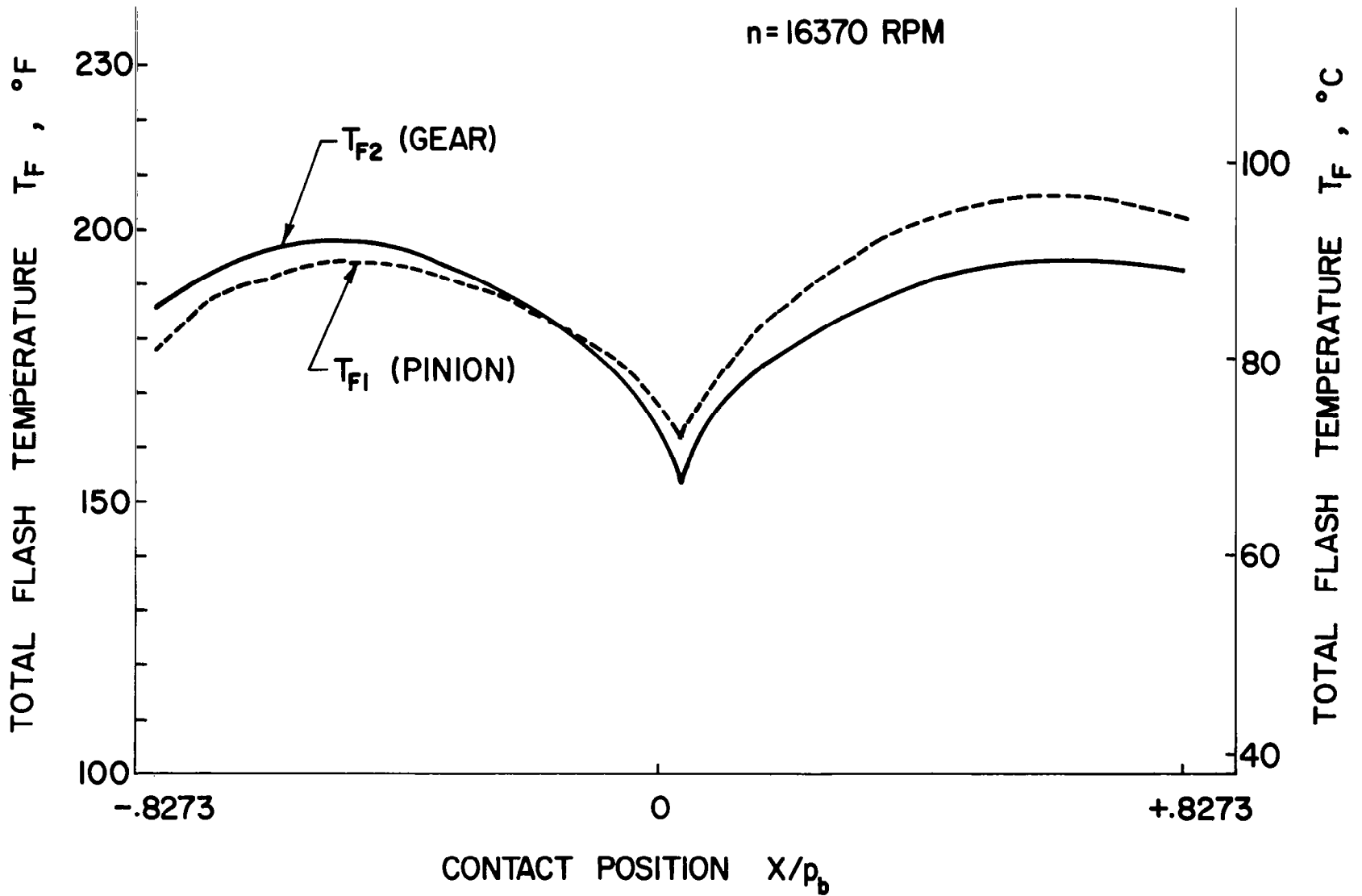Fig. 8.10(c). Distribution of Flash Temperature, (c) n = 16 370 rpm, r_G = 1. Other conditions are listed in Table 8.1.
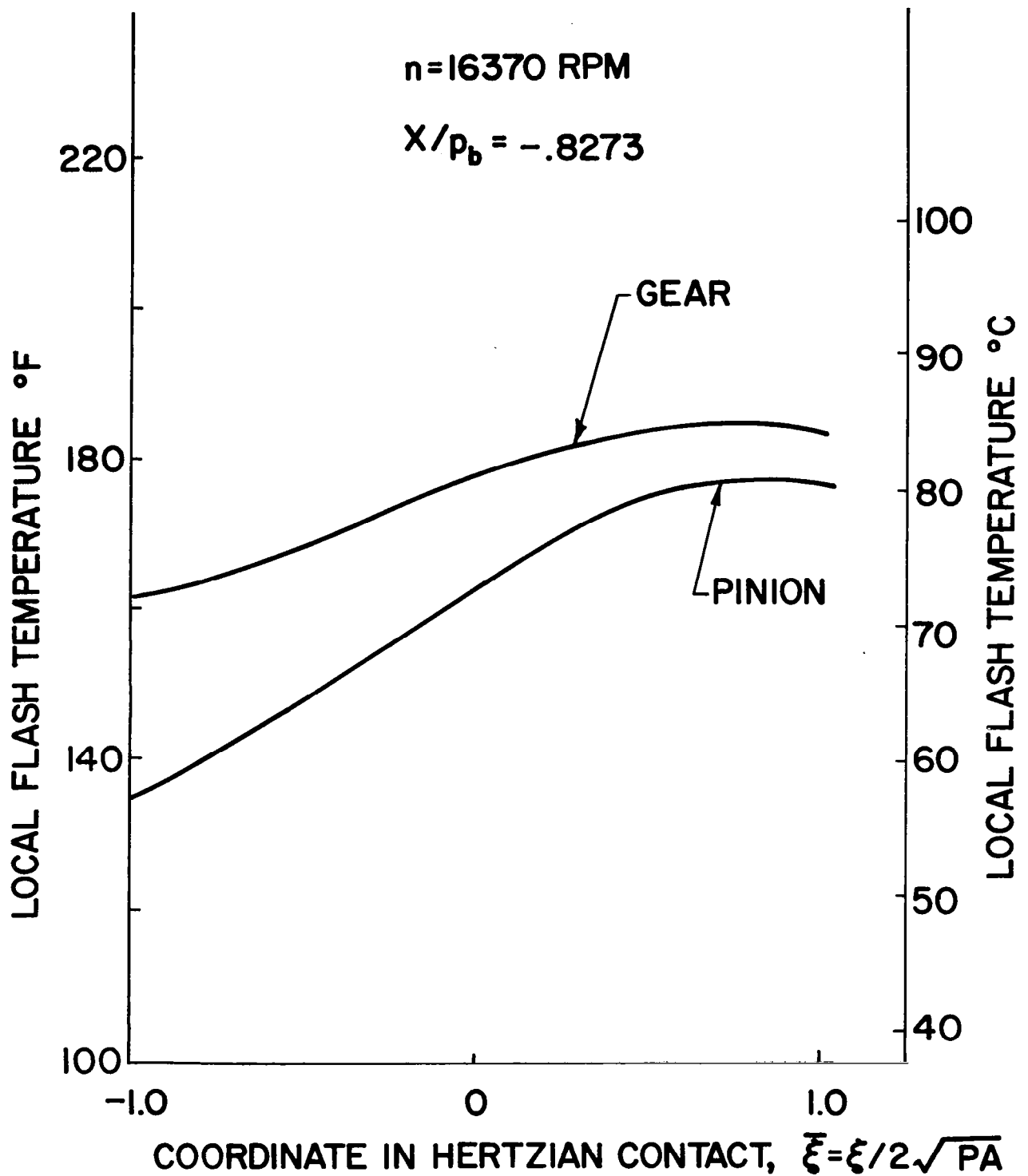
Fig. 8.11(a).   Local Distribution of Flash Temperature Within the
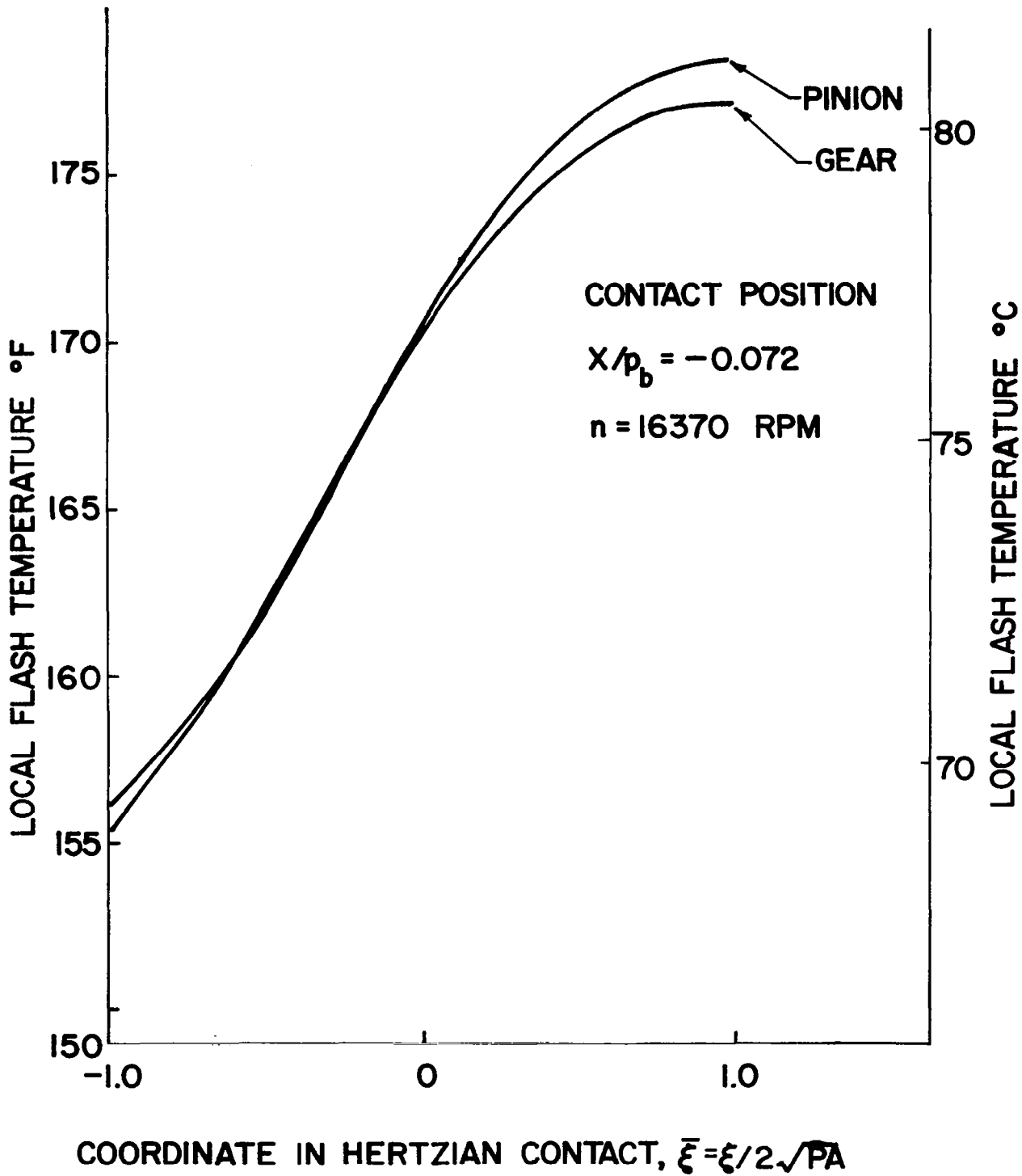Hertzian Contact, (a) $x/p_b = -0.8273$

Fig. 8.11(b). Local Distribution of Flash Temperature Within the
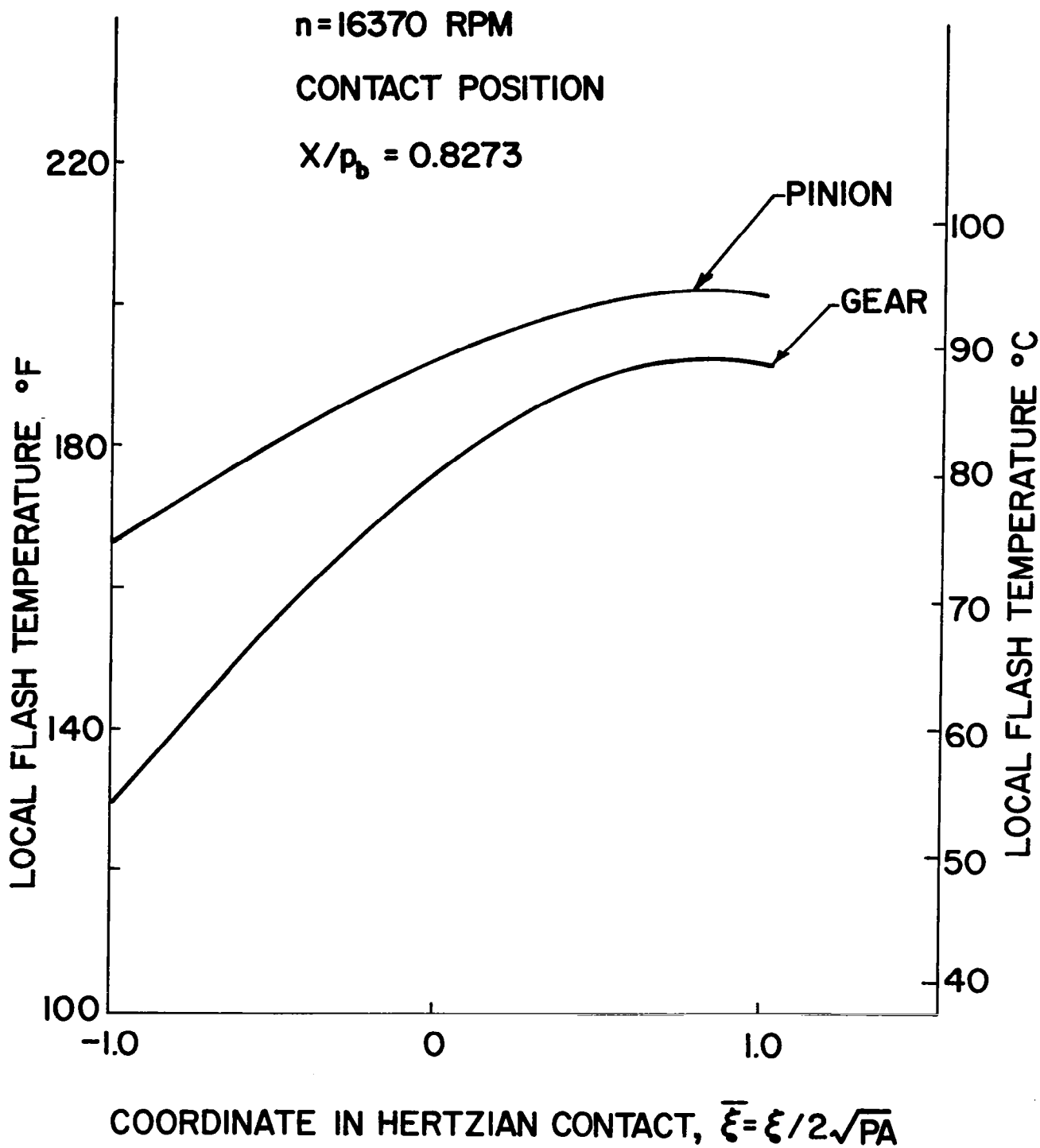Hertzian Contact, (b) $x/p_b = -0.072$

99

Fig. 8.11(c). Local Distribution of Flash Temperature Within the
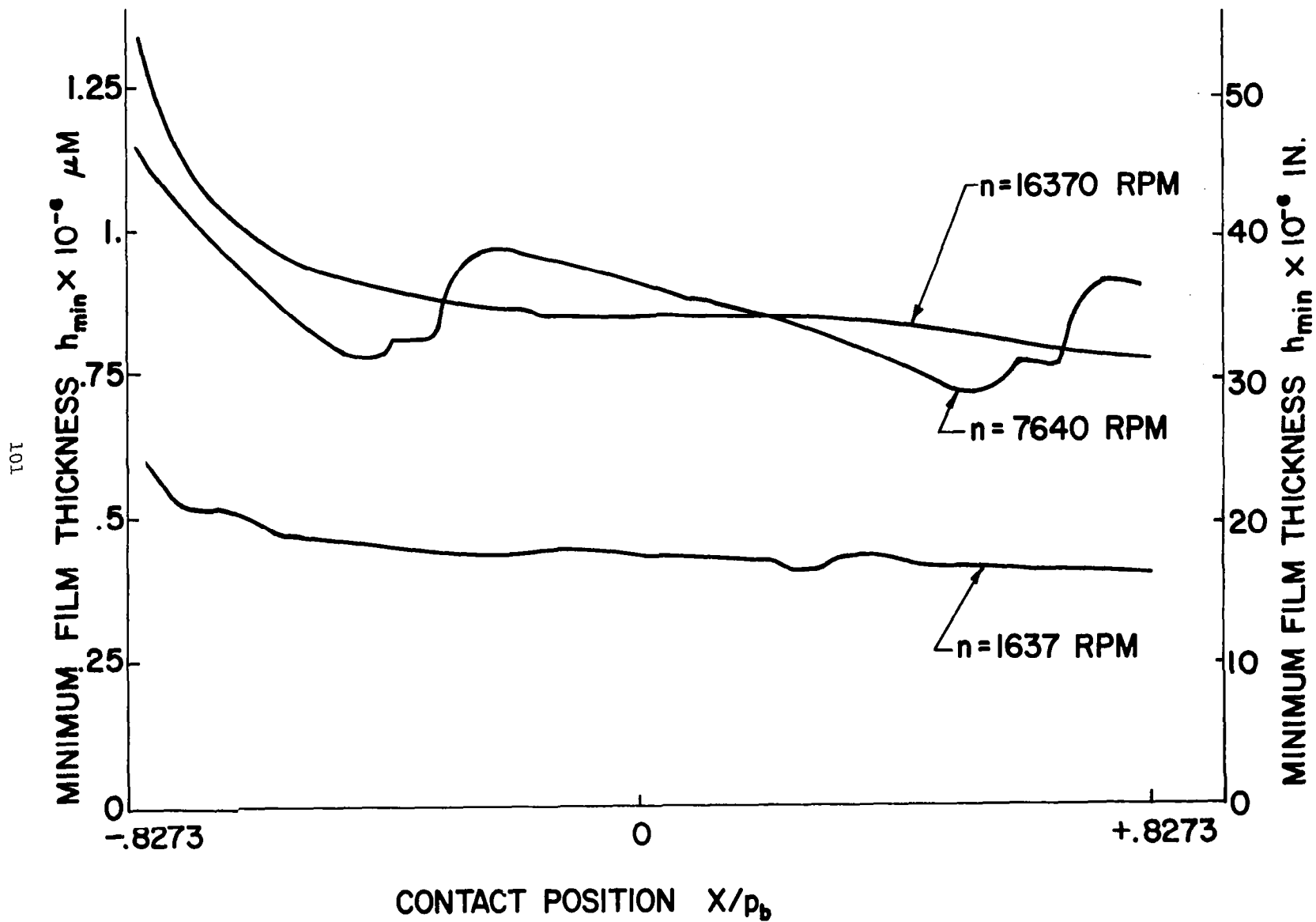Hertzian Contact, (c) x/p_b = 0.8273

Fig. 8.12.   Dynamic Film Thickness Distribution.

8.3.3. Effect of Gear Geometry

The results in the previous section show the detailed distributions along the contact path. In the following sections, one is concerned with the overall performance as affected by the change of geometrical factors. The overall performance is represented by three quantities, the maximum equilibrium surface temperature, the maximum total flash temperature, and the minimum of film thickness. They are chosen to represent the lubrication performance because of their strong influence on the major modes of failure originating from lubrication.

In investigating the effects of gear geometry, the first case considered is the effect of gear face width. Borsoff [Ref. 21] found experimentally that the increase of face width would reduce the specific load carrying capacity (load per unit face width). This phenomenon does not seem to be explainable by Blok's flash temperature theory or by any existing EHD film thickness theory. As shown in Fig. 8.13, the present results indicate that as the face width increases from 0.13 to 0.51 cm (0.05 to 0.2 in.) under the same load there is a corresponding increase in the maximum equilibrium surface temperature as well as in the total flash temperature. The higher surface temperature results in a much reduced minimum film thickness when the face width is increased. This suggests that the experimental trend obtained by Borsoff with regard to the effect of face width can be at least partially accounted for by the present analysis on the basis of its effect on the surface temperature and film thickness.

The effect of gear outside radius is shown in Fig. 8.14. It is seen that when the outside-radius is increased from 4.7 to 6.3 cm (1.85 to 2.35 in.) under a constant load and speed, the total flash tempera-
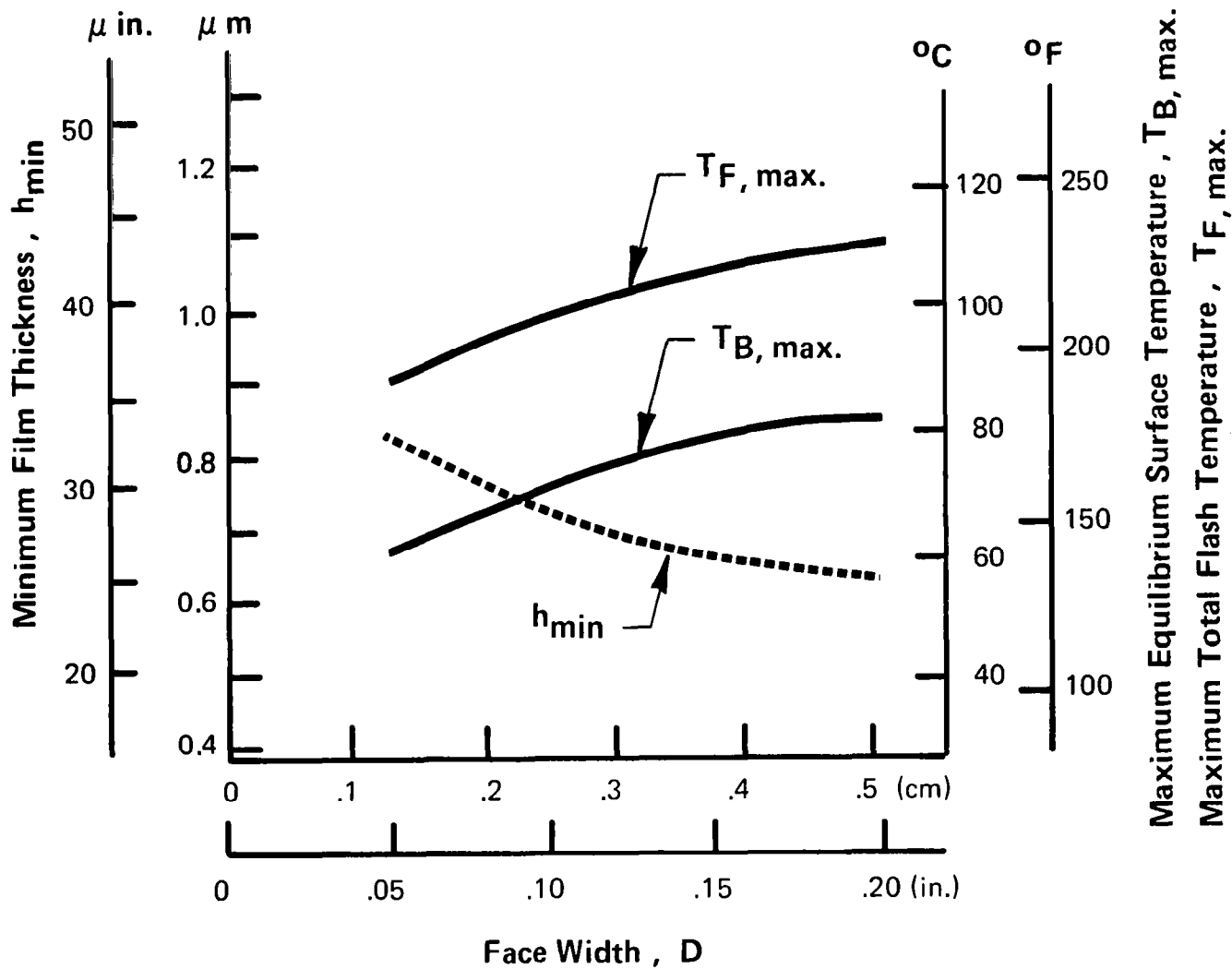
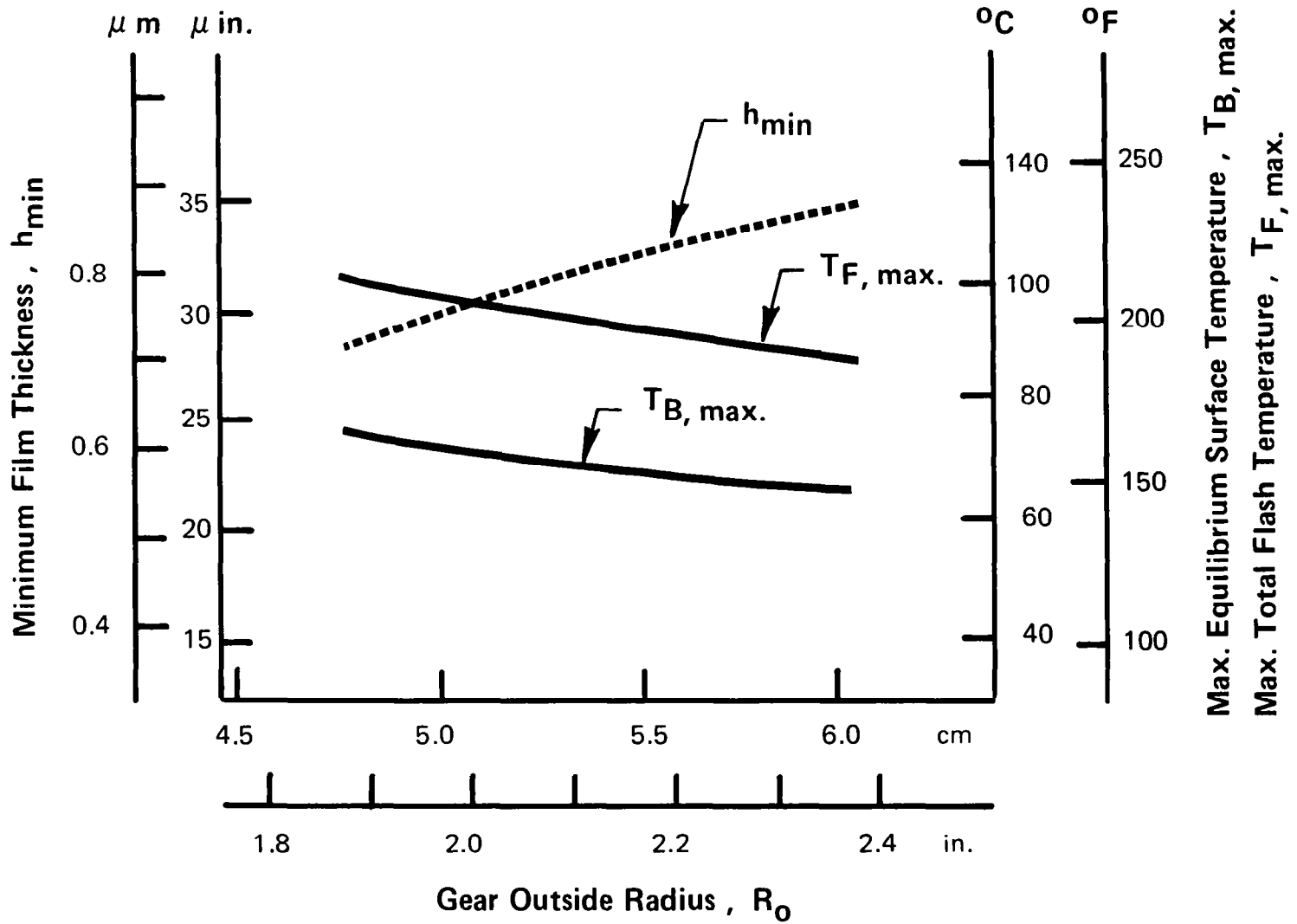Fig. 8.13.   Effect of Face Width on Lubrication Performance

Fig. 8.14.   Effect of Gear Outside Diameter on Lubrication Performance

ture as well as the film thickness are considerably improved. However, one must keep in mind that the improvement in lubrication performance by increasing the size of gears is a rather expensive way to solve the lubrication problem.

The effect of diametral pitch is shown in Fig. 8.15. Since an increase in diametral pitch tends to reduce the dynamic load and the sliding between teeth, the use of gears with a finer pitch yields a lower maximum surface temperature as well as a lower total flash temperature comparing to the corresponding values for coarser gears. The minimum film thickness is also found to be much improved as the diametral pitch changes from 8 to 12. However, it must be kept in mind that the improvement in lubrication performance in this instance can be easily offset by the reduction in flexural strength for gears with a finer pitch.

The effect of a large tip-relief is demonstrated in Figs. 8.16 and 8.17 for the conditions used by Townsend [Ref. 24]. It is seen that both the total flash and equilibrium temperature is greatly reduced in the high-slip region for gears with the tip-relief. This reduction is attributed mainly to the lower heat generation and better load distribution produced by the tip-relief.

Figure 8.18 shows the effect of gear ratio on the lubrication performance. The gear ratio is varied from 1 to 2 by increasing the gear teeth number from 28 to 56. It is seen that the increase in the size tends to improve the cooling effect and hence reduce both the equilibrium temperature and the total flash temperature. The effect on film thickness is even greater because of a larger effective radius in the Hertzian contact.
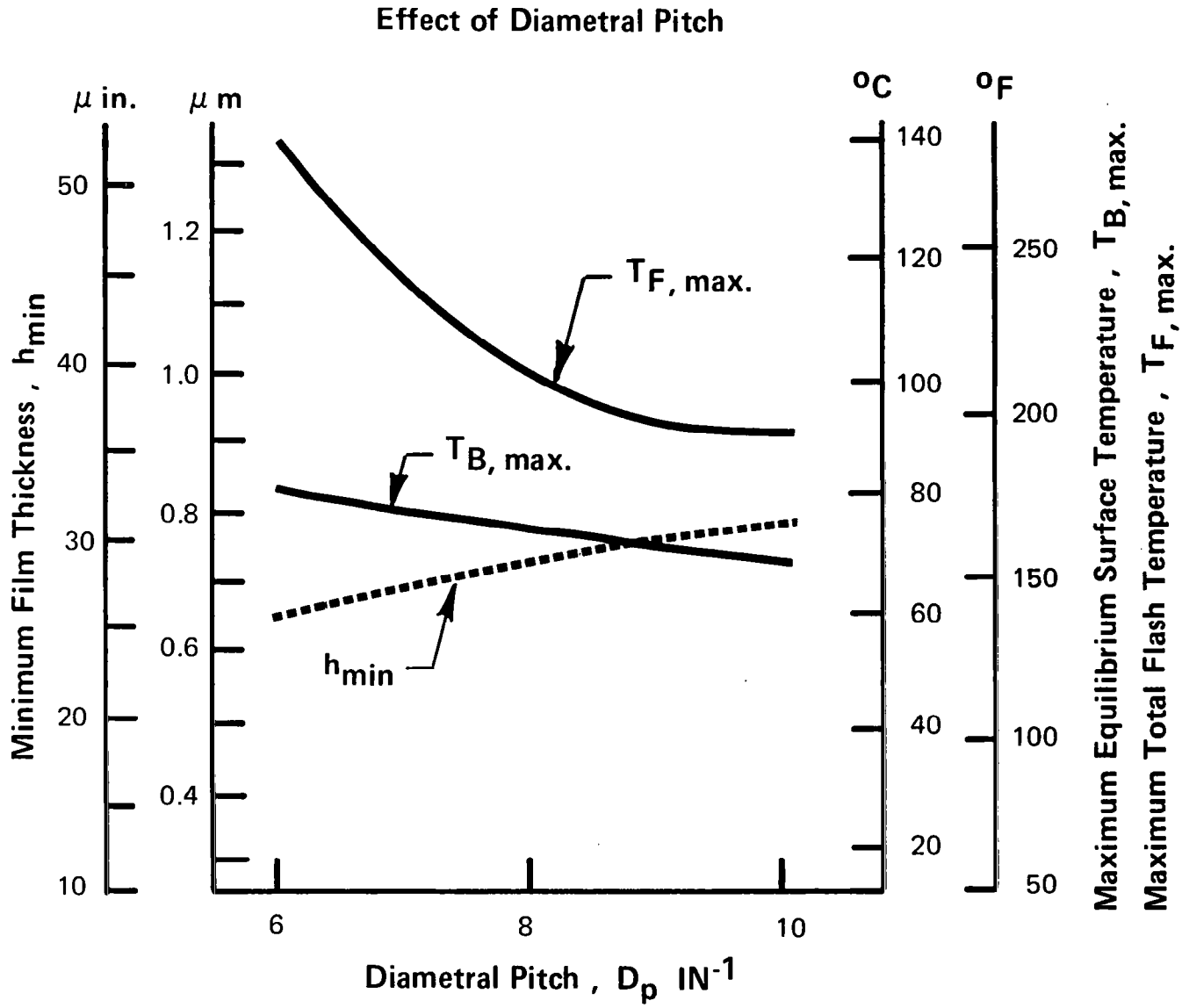
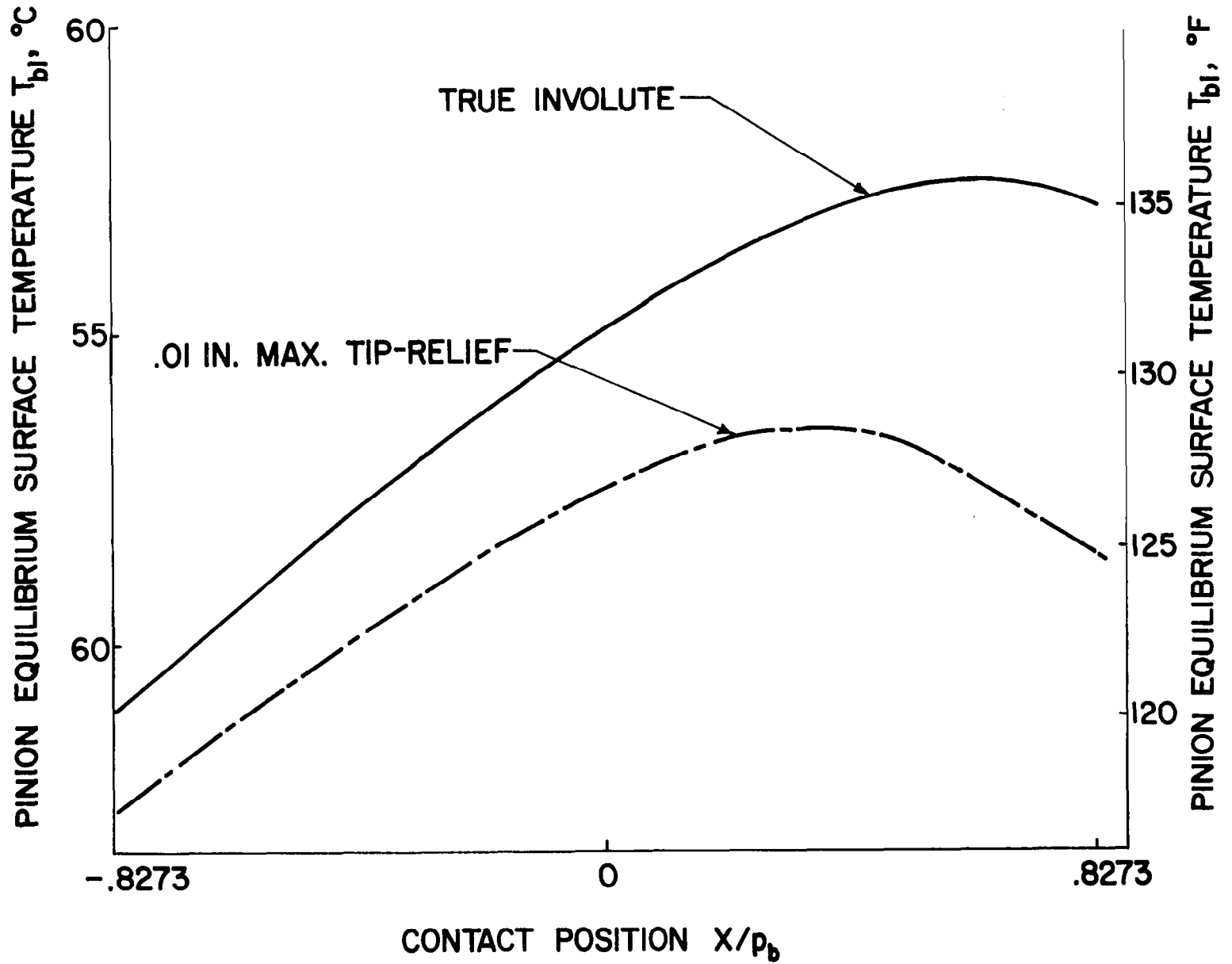Fig. 8.15.   Effect of Diametral Pitch on Lubrication Performance

Fig. 8.16. Effect of a Large Tip-Relief on Pinion Equilibrium
Surface Temperature

Fig. 8.17. Effect of a Large Tip-Relief on Pinion Flash Temperature
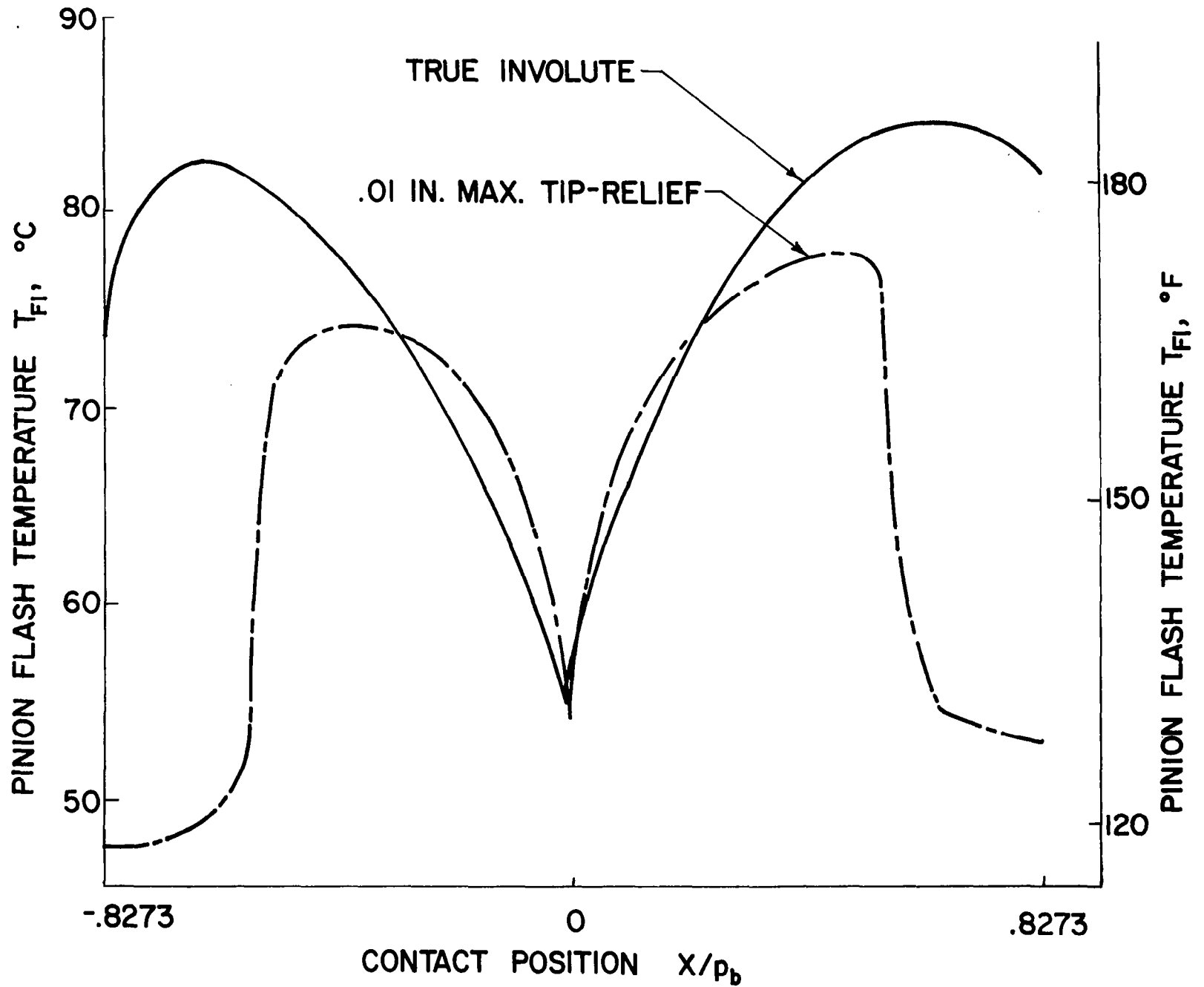
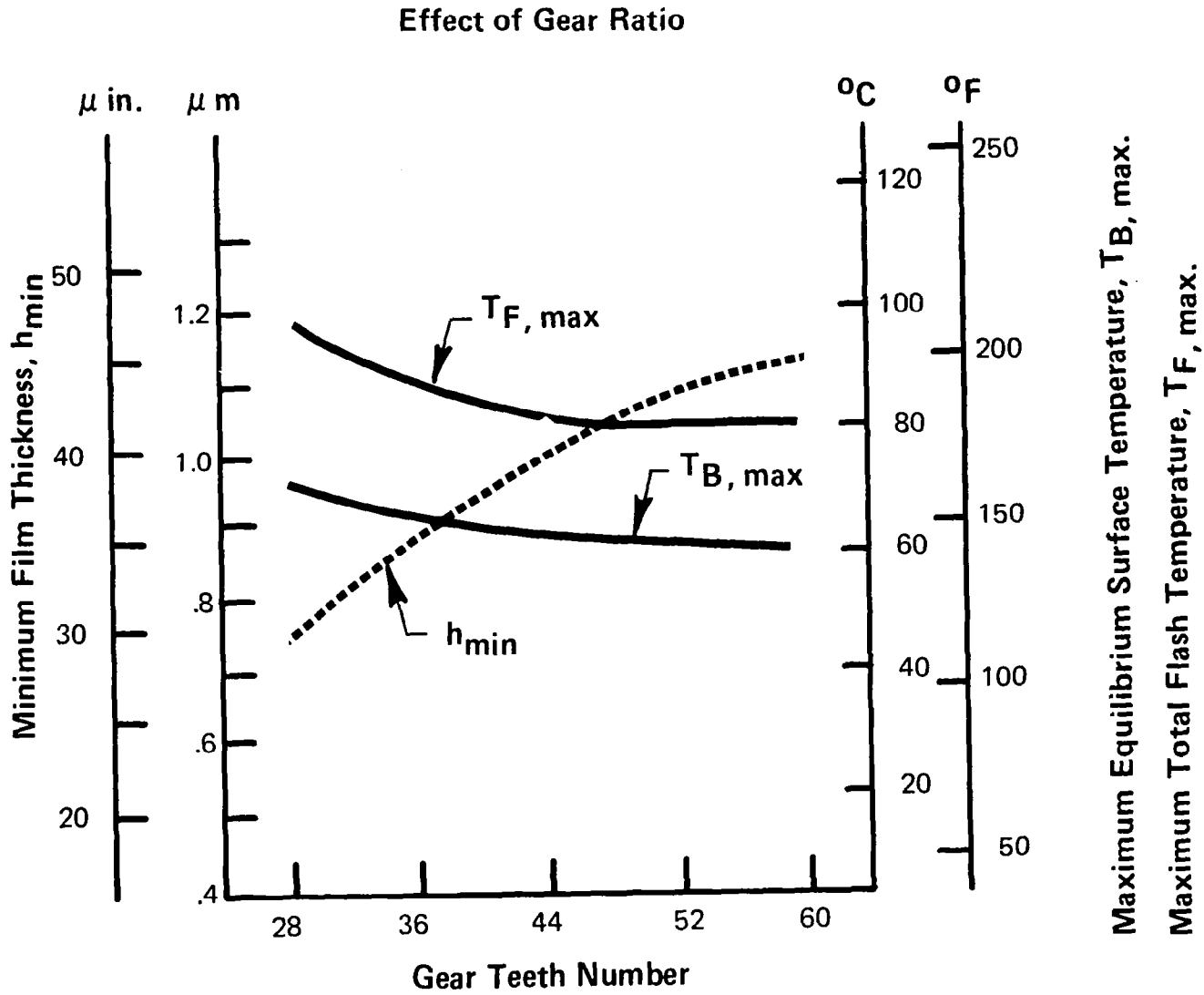Fig. 8.17. Effect of a Large Tip-Relief on Pinion Flash Temperature

Fig. 8.18.   Effect of Gear Ratio on Lubrication Performance.
Pinion Teeth Number = 28.

8.3.4. Effect of Lubricant and Operating Parameters

Aside from the effects of gear geometry, lubricant properties and the gear operating conditions are also known to have an influence on the gear lubrication performance. The effect of lubricant viscosity is shown in Fig. 8.19. When the lubricant viscosity is increased from
(9 x 10^{-6} to 20 x 10^{-6} lb.sec/in^2)
.062 to 0.1379 pa·s , the film thickness is found to have a marked increase, and it is accompanied by a slight decrease in maximum equilibrium and flash temperature on the surface. This indicates that the reduction in load carrying capacity in practice for gears with low viscosity oils is likely caused by the lack of lubricant film in the contact.

The effect of surface convective heat transfer coefficient and the effect of ambient temperature on the lubricant performance are shown separately in Fig. 8.20 and Fig. 8.21. Increasing the heat transfer coefficient or decreasing the operating ambient temperature is shown to have a substantial improvement on the lubrication performance.

Among the effects of operating parameters, perhaps the most interesting one is the speed effect. Fig. 8.22 shows the results on the effect of speed for the same set of gears considered in the preceding sections. It is seen that as the pitch-line speed increases from 21.1
(830 to 2830 in/sec)
to 72.0 m/sec., the minimum film thickness experiences a gradual increase which appears to be sustained throughout the high-speed region. The corresponding flash temperature also shows a slight improvement with speed in spite of a gradual increase in the equilibrium temperature. This trend seems to be in accord with the experimental evidence provided by Borsoff [Ref. 21] and Ku [Ref. 22] in which they concurred

Effect of Lubricant Viscosity
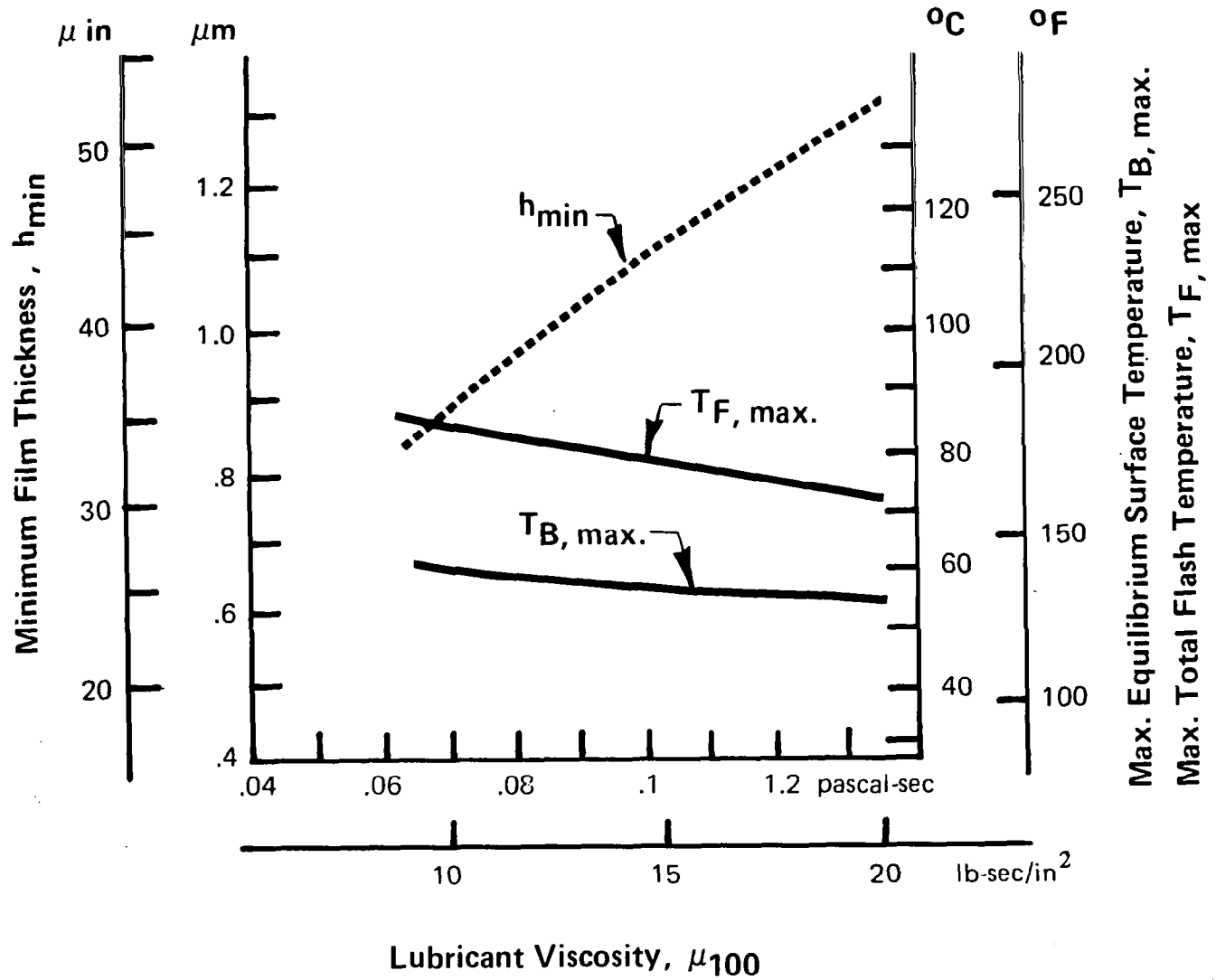

Fig. 8.19. Effect of Lubricant Viscosity on Lubrication Performance, P = 0.7 MN/m (4000 lb/in), D = 0.127 cm (0.05 in.)
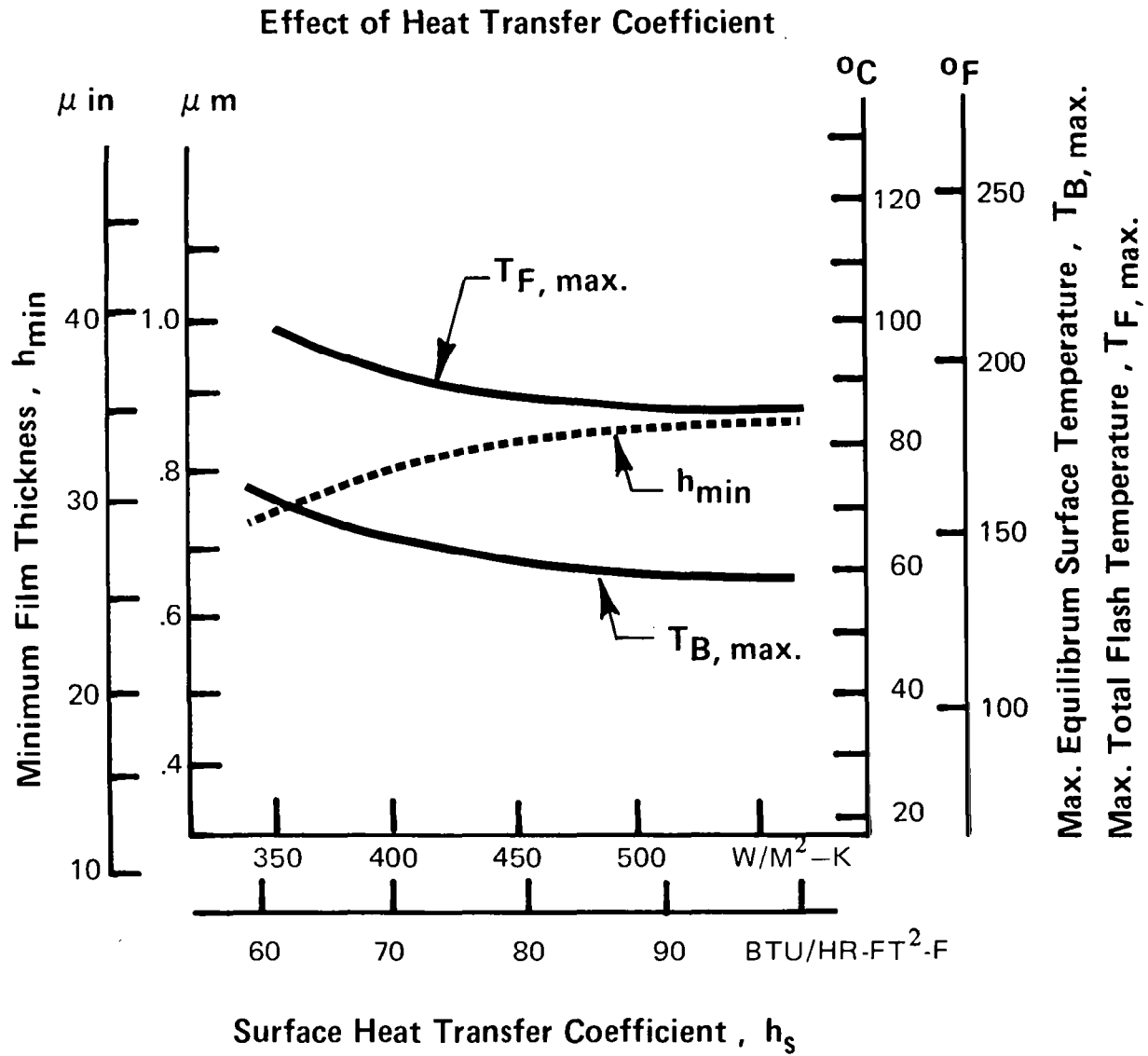
Fig. 8.20.   Effect of Surface Heat Transfer Coefficient on Lubrication
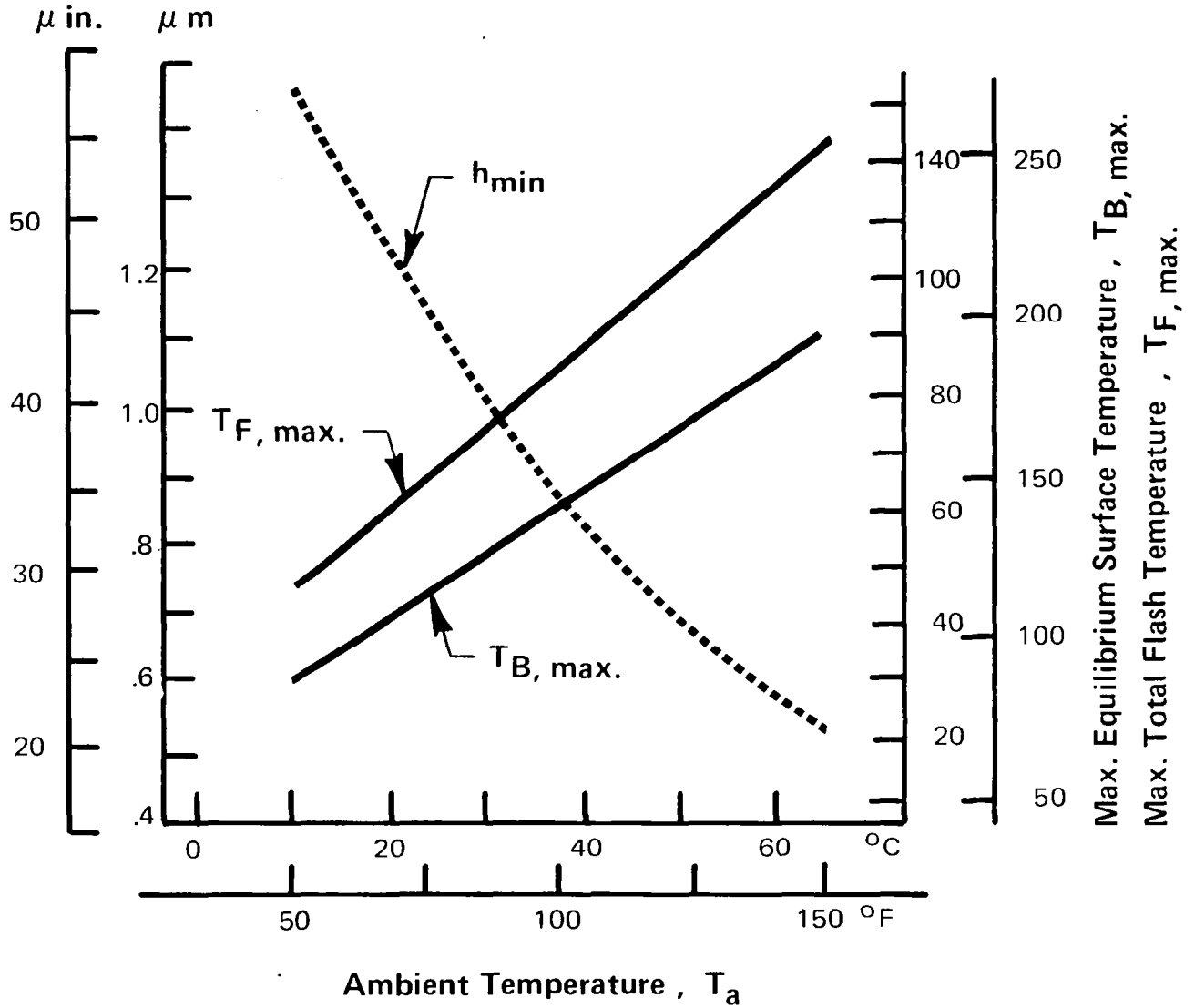   Performance.

Effect of Ambient Temperature

Fig. 8.21: Effect of Ambient Temperature on Lubrication Performance
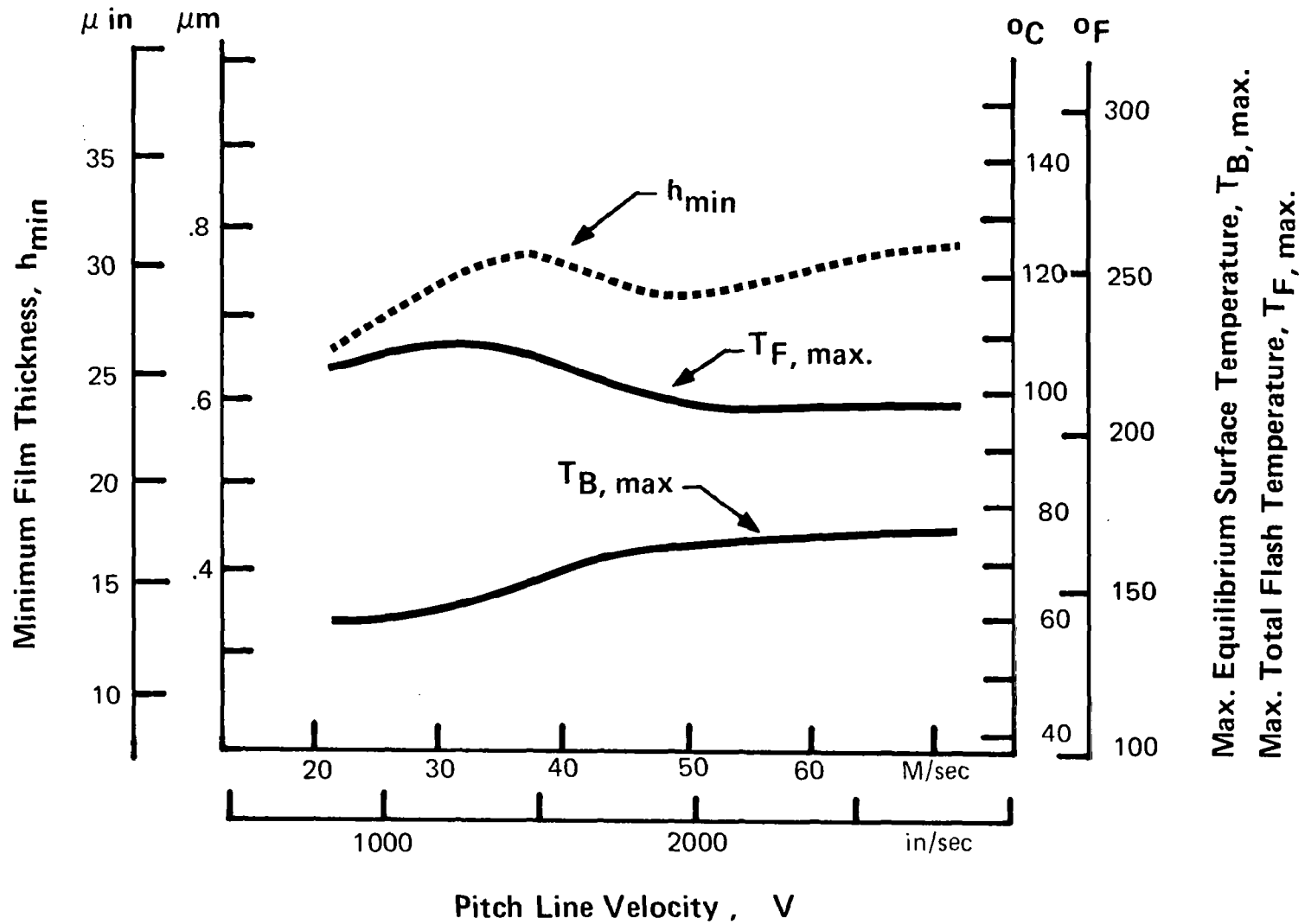
Fig. 8.22.   Effect of Surface Speed on Lubrication Performance

that the scuffing load capacity increases gradually with speed in the
high-speed region.

(4300 lb/in to 6300 lb/in)

The results by varying the tooth load from .753 MN/m to 1.103 MN/m
are plotted in Fig. 8.23. It is seen that the minimum film decrease
linearly with the load, and the equilibrium temperature as well as the
flash temperature increases also linearly with the load.

8.3.5. Dimensionless Design Charts for Equilibrium Surface Temperature

As illustrated in the preceding sections that the lubrication per-
formance is characterized mainly by the minimum film thickness and the total
flash temperature between a pair of teeth throughout the entire cycle of
the engagement. These quantities can be calculated by means of the com-
puter program TELSGE.

However, it was found that at least for the minimum film thickness
there is a simpler method to estimate it without using the computer
program. This is accomplished by first determining the equilibrium
surface temperature through the use of dimensionless charts. The
minimum film thickness then can be estimated by using the well known
EHD film thickness formula due to Dowson and Higginson [Ref. 14].

Extensive examination of the results of equilibrium temperature
reveals that they are essentially governed by a functional relation-
ship among four dimensionless parameters. These are

$$\theta = \frac{k \left(T_{B,max.} - T_A \right)}{U_{S,max.} P_{d,max.} N} \quad - \quad \text{normalized equilibrium temperature}$$

$$B_i = \frac{h_S R_o}{k} \quad - \quad \text{Biot Number}$$

$$\Lambda_f = \frac{R_o}{D} \quad - \quad \text{face width ratio}$$

$$r_G \quad - \quad \text{gear ratio}$$

These dimensionless charts are shown in Fig. 8.24 and Fig. 8.25 for $r_G = 1,2$ respectively. The accuracy of these charts has been checked by using the present computer program to obtain the dimensional surface temperature for a wide range of dimensional input data for those quantities appeared in the above non-dimensional parameters.
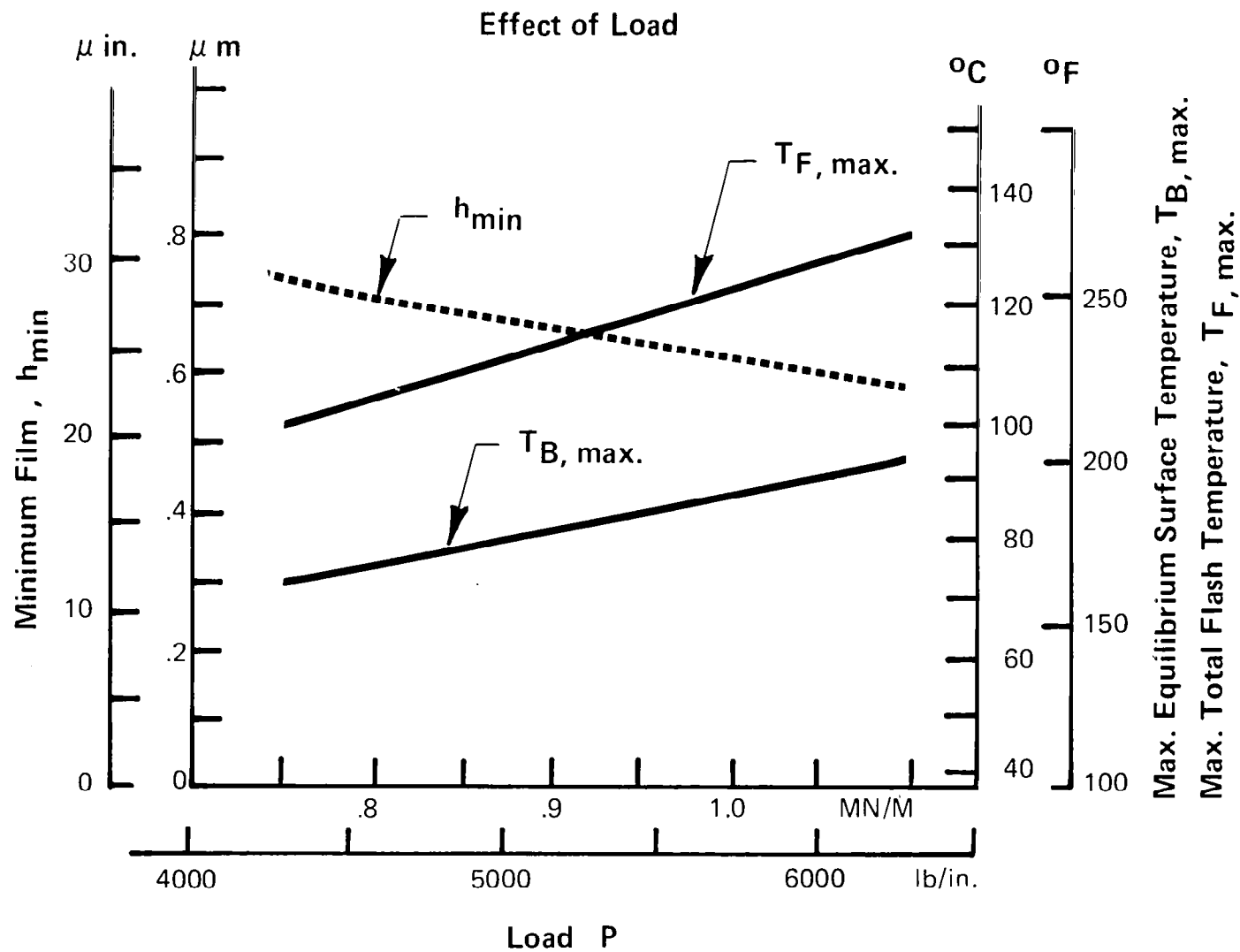
Effect of Load

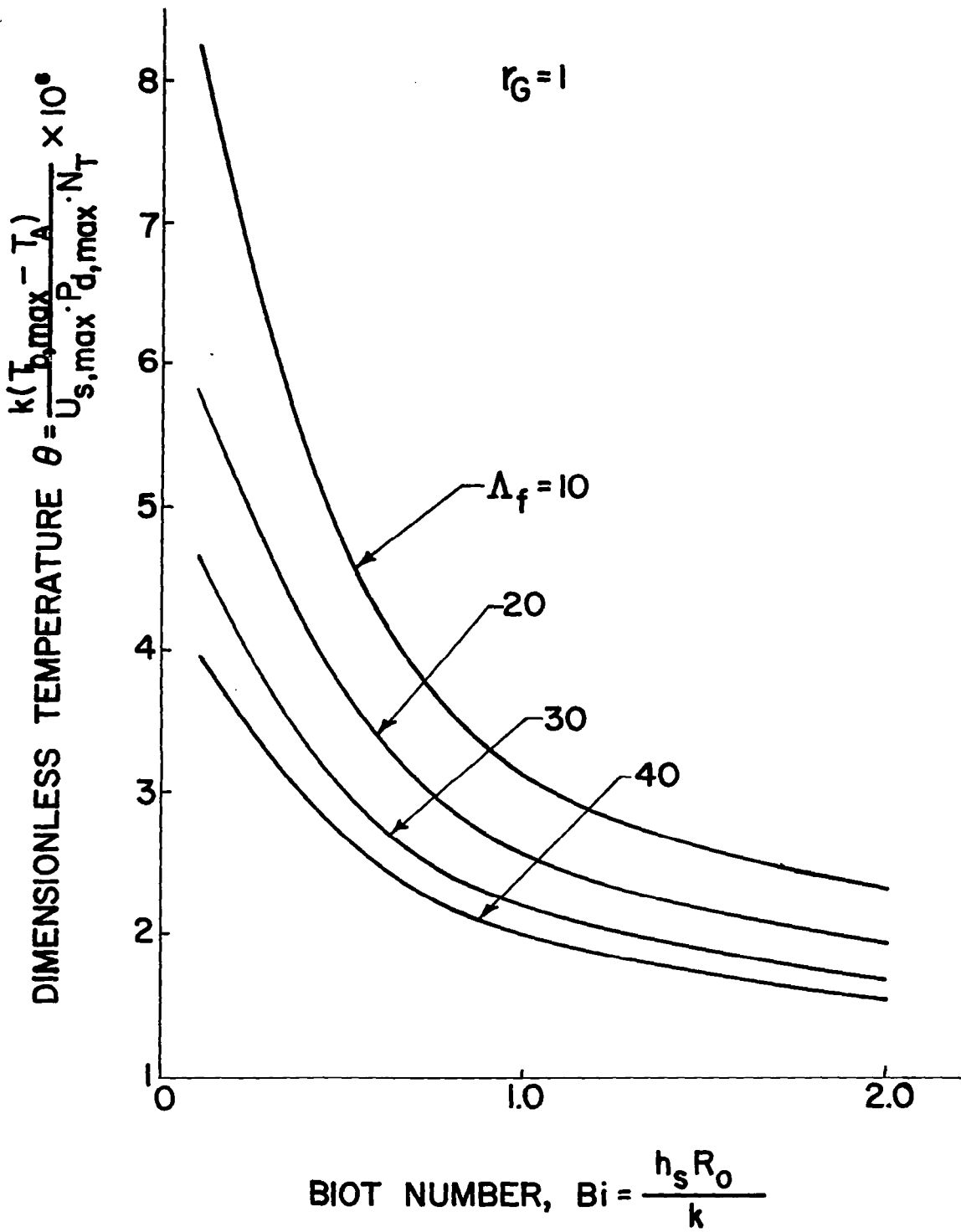Fig. 8.23.   Effect of Load on Lubrication Performance

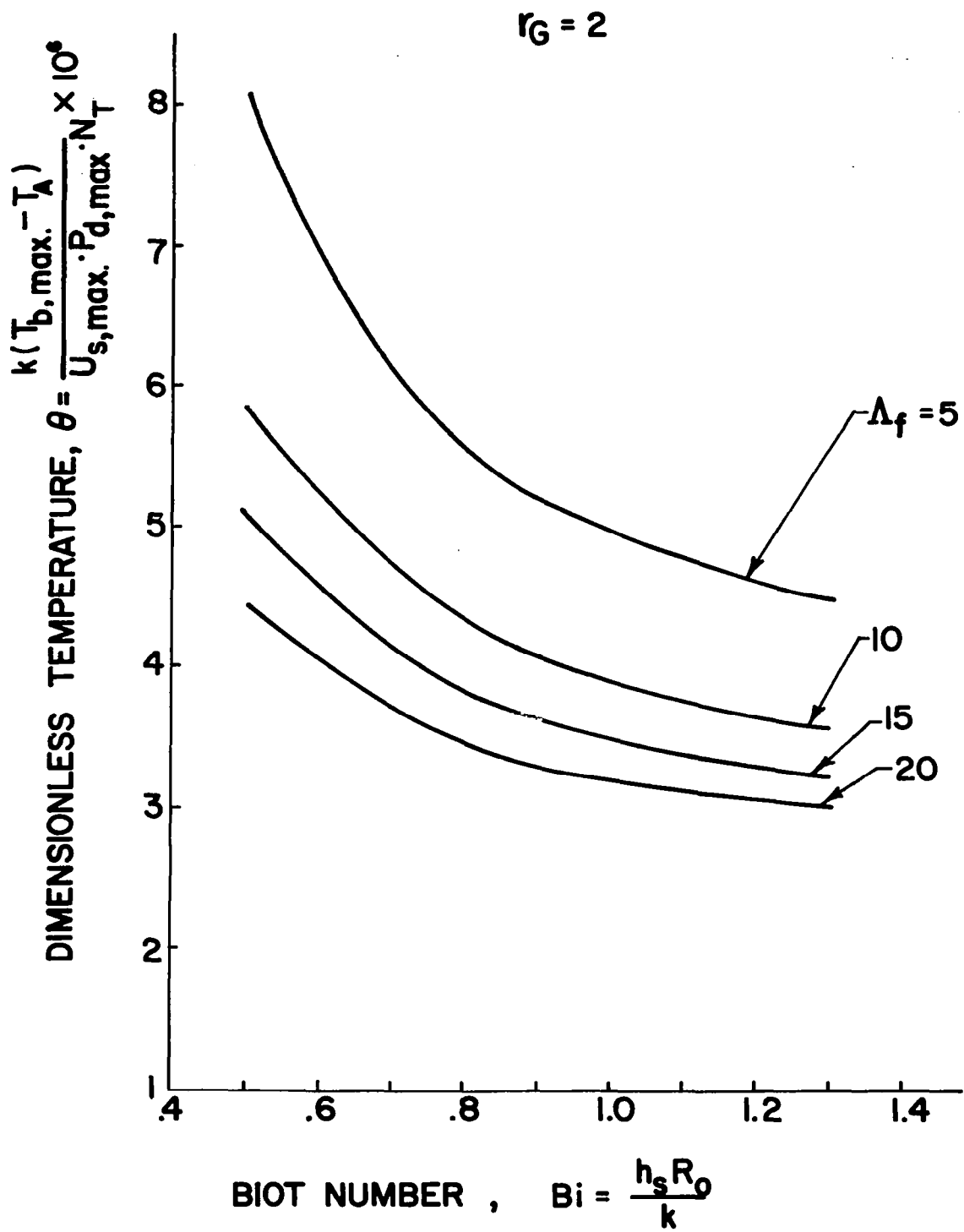Fig. 8.24.   Design Chart for Equilibrium Surface Temperature, $r_G = 1$

Fig. 8.25.   Design Chart for Equilibrium Surface Temperature, $r_G = 2$

119

IX SUMMARY OF RESULTS

An analysis and computer code were developed to predict the variations of dynamic load, surface temperature, as well as the lubricant film thickness along the contacting path during the engagement of a pair of involute spur gears.

The dynamic load is assumed to be not influenced by the lubricant film thickness or by the surface temperature, and, therefore is analyzed independently. The analysis of dynamic load includes the effect of gear inertia, the effect of load sharing of adjacent teeth, and the effect of variable tooth stiffnesses which are obtained by a finite-element method.

The surface temperature at a point along the tooth profile is assumed to be an equilibrium value when it is not in contact with the mating gear and rises suddenly to a flash temperature during the sliding contact. The distribution of the equilibrium temperature is solved by a three-dimensional finite-element heat conduction analysis, and the flash temperature is solved by a simplified energy equation using a limiting shear concept for the heat dissipation. The lubricant film thickness is based on a transient EHD analysis which includes the squeeze-film effect. These mutually dependent quantities are solved simultaneously with an iterative process.

Results of dynamic load were obtained for a pair of gears with dimensions corresponding to that used by Townsend and Zaretsky in their gear experiments. The dynamic load distributions along the contacting path for various speeds show patterns similar to that observed experimentally. Effects of damping ratio, contact ratio, tip relief, and tooth error on the dynamic load were examined.

Gear lubrication performance was evaluated by plotting the maximum equilibrium temperature, the maximum flash temperature, and the minimum film thickness along the contacting path for various geometric and operating parameters. It was found that an increase in diametral pitch or a decrease in face width for the same specific load gives a better lubrication performance. These trends agree qualitatively with results by Borsoff [Ref. 21] and by Baber and Ku [Ref. 22]. Among the operating variables, the lubrication performance is improved most strongly by increasing the inlet lubricant viscosity, by decreasing the ambient temperature, or by increasing the convective heat transfer coefficient on the gear surface. Increasing the pitch line velocity gives a slight improvement in lubrication performance at high speeds. However, the trends do not indicate any signs which can account for the dramatic increase in scuffing load observed by Borsoff at very high speeds.

In addition, two dimensionless charts are presented for predicting the maximum equilibrium surface temperature, which can be used to estimate directly the lubricant film thickness based on well established EHD analysis.

APPENDIX A

THREE DIMENSIONAL INTERPOLATION BY ISOPARAMETRIC MAPPING

The method of isoparametric mapping is widely used in Finite Element Method [Ref. 38]. This method can be used here to interpolate the value of the coefficients in the matrix $[\overline{D}]^S$ as functions of N_T, Λ_f, and B_i.

As shown in Fig. A.1, the region covered are bounded by

$$50 < N_T < 150$$
$$6 < \Lambda_f < 48$$
$$.3 < B_i < 3$$

is divided into four subregions I, II, III and IV for better approximation of the coefficients in $[\overline{D}]^S$. The values used as dividing points in this case are

point a $(\Lambda_f = 6., B_i = 1.)$,   point b $(\Lambda_f = 12., B_i = .3)$

point c $(\Lambda_f = 48, B_i = 1.)$, and   point d $(\Lambda_f = 12., B_i = 3)$.

For a given set of N_T, Λ_f and B_i, each of the coefficients $\overline{D}_{ij}^S$ can be approximated by the following procedures.

1. locate the subregion which contains the given set N_T, Λ_f and B_i.

2. the value of $\overline{D}_{ij}^S$ is approximated by

$$\sum_{k=1}^{20} N_k(\epsilon, \eta, \xi) \left(\overline{D}_{ij}^S\right)_k \tag{A.1}$$

where $\left(\overline{D}_{ij}^S\right)_k$ are the coefficients $\overline{D}_{ij}^S$ calculated for N_T, Λ_f, B_i at note 1 to 20. The numbering of these nodes is shown in Fig. A.2. ϵ, η and ξ are the local coordinates used for N_T, Λ_f and B_i such that the values of ϵ, η and ξ are between -1. and 1. The coordinates transformation relationship are simply

$$\varepsilon = \frac{2N_T - (N_T)_L - (N_T)_U}{(N_T)_U - (N_T)_L} \tag{A.2}$$

$$\eta = \frac{2\Lambda_f - (\Lambda_f)_L - (\Lambda_f)_U}{(\Lambda_f)_U - (\Lambda_f)_L} \tag{A.3}$$

$$\xi = \frac{2B_i - (B_i)_L - (B_i)_U}{(B_i)_U - (B_i)_L} \tag{A.4}$$

where $(\ )_U$ means the upper bound of that variable and

$(\ )_L$ means the lower bound.

$N_k(\varepsilon, \eta, \xi)$ are the shaping functions for the isoparametric mapping where k is the nodal number shown in Fig. A.2. The quadratic function N_k for a typical corner node, such as node 1, is

$$N_k = 0.125 \times (1 + \varepsilon_o)(1 + \eta_o)(1 + \xi_o)(\varepsilon_o + \eta_o + \xi_o - 2) \tag{A.5}$$

for a typical mid-side node such as node 2

$$\varepsilon_2 = 0 , \quad \eta_i = \pm 1 , \quad \xi_i = \pm 1$$

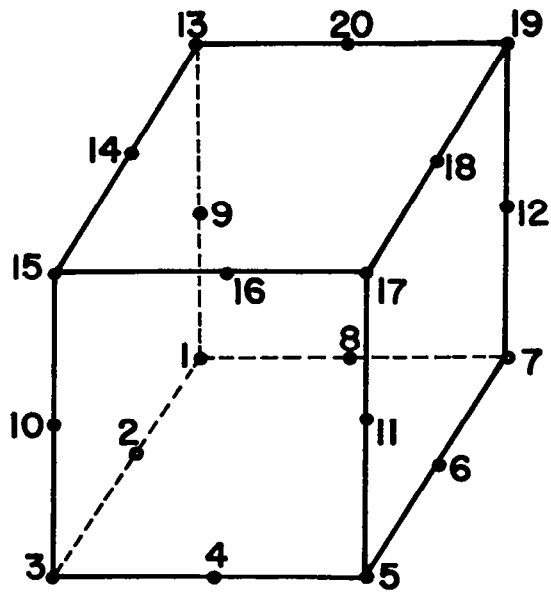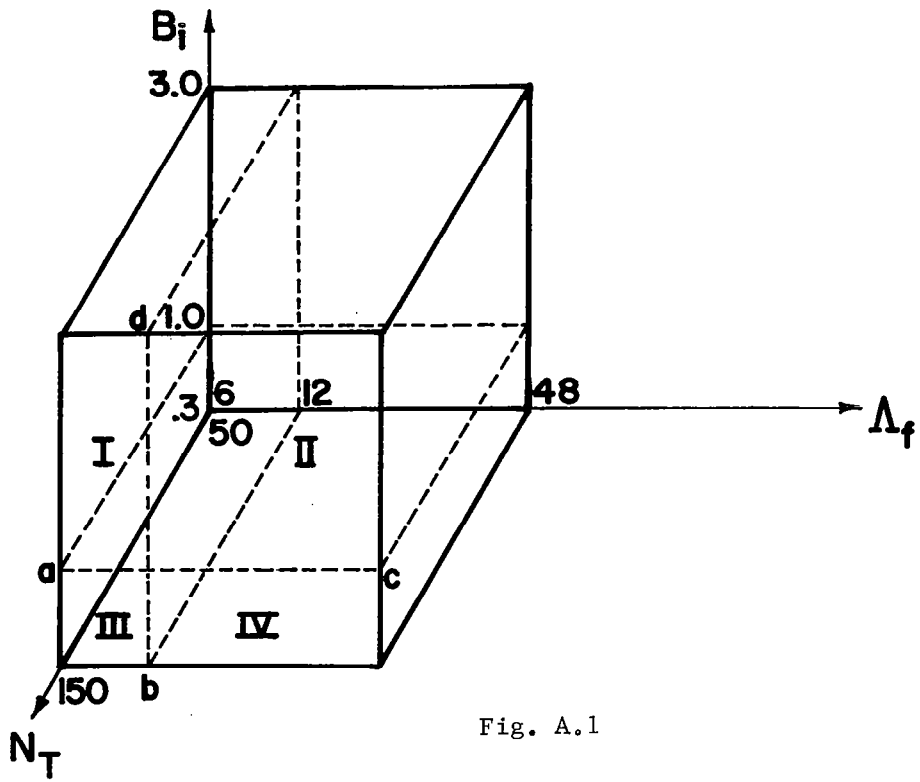$$N_k = 0.25 (1 - \varepsilon^2)(1 + \eta_o)(1 + \xi_o) \tag{A.6}$$

where ε_o, η_o and ξ_o are the generalized variable, for node k

$$\varepsilon_o = \varepsilon \times \varepsilon_k$$

$$\eta_o = \eta \times \eta_k \tag{A.7}$$

$$\xi_o = \xi \times \xi_k$$

Fig. A.1

Fig. A.2

124

APPENDIX

SYMBOLS

a_i	= constant in Eq. (4.15), see Table 4.1
A	= R/R_i
$[A]$	= coefficient matrices in Eqs. (6.14) to (6.16)
b_i	= constants in Eq. (4.15), see Table 4.1
$[\overline{B}]$	= matrix in Eq. (6.33)
B_i	= Biot number = $h_s R_o/k$
C	= a constant for the film thickness formula Eq. (2.1)
C	= $(D/2R_o)^2$
C_o	= damping coefficient per unit face width N-sec/in^2(lb.sec/in^2)
C_r	= contact ratio
$[\overline{C}]$	= matrix in Eq. (6.33)
D_p	= diametral pitch, 1/in.
D	= face width,cm(in.)
$[\overline{D}]$	= 8/19 $[\overline{C}]$ - $[\overline{B}]$
e	= profile error,cm(in.)
E	= Youngs modulus of gear material,N/m^2(psi)
E_b	= P/δ, tooth stiffness per unit tooth width, N/m^2(psi)
E'	= $\left(\dfrac{1-\nu_1^2}{E_1} + \dfrac{1-\nu_2^2}{E_2}\right)^{-1}$, equivalent Youngs Modulus, N/m^2(psi)
G_1,G_2,G_3,G_4	= see Eqs. (4.10), (4.11), (4.12), (4.13)
$\overline{G}_\infty$	= limiting shear modulus, N/m^2(psi)
h	= film thickness, cm(in.)
h_o	= plateau film thickness
h_s	= surface heat transfer coefficient, W/m-K(B/hr.ft^2-F)
H	= h/R_i

I_1, I_2 = see Eqs. (5.17), and (5.18)

J = polar mass moment of inertia per unit face width, $kgm(lb.sec^2)$

J_1, J_2 = see Eqs. (5.19), and (5.20)

k_1, k_2 = thermal conductivity of pinion and gear $W/m^2K(B/ft.hr.F)$

k_s = a parameter used in Ref. 25 to obtain $\bar{G}_\infty$ for continuous shear

K = $E_{b_1}E_{b_2}/E_{b_1} + E_{b_2}$, combined stiffness per unit face width, N/m^2(psi)

K_1, K_2 = see Eqs. (5.21) and (5.22)

k_f = thermal conductivity of the lubricant, $W/m^2K(B/ft.F.hr)$

m = J/R_b^2, reduced mass per unit face width, $kg/m(lb.sec^2/m^2)$

M = $m_1m_2/M_1 + m_2$

n = a length coordinate in the direction of the outward normal to the surface

n_1, n_2, n_3 = exponents used in Eq. (2.1)

N = n/R_o

N = $12\mu_T u/E'R$

N_T = number of teeth

N_i^1, N_j^2 = finite element tensor shaping functions

p = pressure in the Hertzian contact pascal (psi)

P_b = base pitch, cm(in.)

P_c = circular pitch, cm(in.)

P_{Hz} = maximum Hertzian contact pressure pascal (psi)

P = load per unit face width, N/m(lb/in.)

$\bar{P}$ = $-\int \frac{\ln(1-GQ)}{G} d\xi = P/ER_r$

P_d = dynamic load per unit face width, N/m(lb/in.)

P_s = static load, N/m(lb/in.)

q	= heat flux
Q	= $(1-e^{-\alpha P})/G$
Q^*	= $q_{ave.} R_o / (U_{smax.} P_{max.})$
r	= local radius of tooth profile, cm(in.)
R	= $r_1 r_2 / r_1 + r_2$, relative radius, cm(in.)
R_1, R_2	= pitch radius of pinion and gear, cm(in.)
R_b	= base radius, cm(in.)
R_i	= R evaluated at the pitch point, cm(in.)
R_o	= outside radius of pinion and gear, cm(in.)
R_r	= root radius, cm(in.)
$\{R\}$	= see Eq. (6.27) to (6.29)
S	= $\omega R / u$
T	= temperature of lubricant, C(F)
T_a	= ambient temperature, C(F)
T_b^*	= $k(T_b - T_a)/(U_{smax.} P_{max.})$
T_{ij}^*	= value of T_b^* at the node ij
T_{mid}	= temperature at the mid-film, C(F)
u	= rolling velocity, $(u_1 + u_2)/2$, m/sec(in/sec)
u_1, u_2	= velocity along the tangent of the contact for pinion and gear, m/sec(in/sec)
u_s	= sliding velocity of the contact, m/sec(in/sec)
V	= pitch line velocity, m/sec(in/sec)
x,y,z	= coordinates attached to a single tooth segment
$\bar{x}$	= x/R_o
X	= distance between the contact point and the pitch point, cm(in.)
X_R	= $X_1 - X_2$, relative displacement, cm(in.)
$\tilde{X}$	= X/R_i

127

$\bar{y}$ = y/R_o

y_p = intersection of the load vector and the y-axis (see Fig. 3.4), cm(in.)

$\bar{z}$ = z/D

Z_a = length of approach, cm(in.)

Z_r = length of recess, cm(in.)

α = pressure viscosity coefficient, $m^2/N(in^2/lb)$

β = $H_o/\bar{P}$

γ = h_s/k, $cm^{-1}(in^{-1})$

δ = tooth deformation normal to surface, cm(in.)

Δ = period of each gear rotation, sec.

η = dummy variable for integrals in Eqs. (4.10) to (4.14)

θ = angular displacement, degree

θ = inclination angle of the load, degree

Λ = local heat partition function

Λ_f = R_o/F = ratio of radius to face width

μ_T = lubricant viscosity at temperature T, pascal-sec($lb.sec/in^2$)

μ_o = viscosity at the inlet of the contact, pascal-sec($lb.sec/in^2$)

ν = Poisson ratio

ξ = coordinate along the Hertzian contact, cm(in.)

ξ' = dummy variable for ξ, cm(in.)

$\bar{\xi}$ = ξ/R_i

ρ = density of the lubricant, $kg/cm^3(lb.sec^2/in^4)$

ρ_1, ρ_2 = density of pinion and gear, $kg/cm^3(lb.sec^2/in^4)$

τ = ωt

$\tau_{smax.}$ = limiting shear stress, $N/m^2(psi)$

ϕ = pressure angle, degree

ω = time base

ω_1, ω_2 = angular velocity of pinion and gear, rad/sec.

$[\Omega]_1, [\Omega]_2, [\Omega]_{\overline{3}}$ see Eqs. (6.24) to (6.26)

Subscripts and Other Abbreviations

$(\cdot), (\cdot\cdot)$ refer to d/dt in Chapter III

$(\cdot)$ refers to $d/d\tau$ in Chapter IV

1   refer to pinion if not specified

2   refer to gear if not specified

REFERENCES

1. Buckingham, E., "Analytical Mechanics of Gears," McGraw-Hill Book Co., New York, 1949.

2. Tuplin, W. A., "Dynamic Loads on Gear Teeth," Machine Design, Vol. 25, No. 10, 1953, pp. 203.

3. Reswick, J. B., "Dynamic Loads on Spur and Helical Gear Teeth," Trans. ASME, Vol. 77, 1955, pp. 635-644.

4. Tuplin, W. A., "Dynamic Loads on Gear Teeth," Proceedings, International Conference on Gearing, Institution of Mechanical Engineers, London, 1958, pp. 24-42.

5. Attia, A. Y., "Dynamic Loading of Spur Gear Teeth," Journal of Eng. for Ind., Trans. ASME, Series B, Vol. 81, 1959, pp. 1-9.

6. Houser, D. R., and Seireg, A., "Evaluation of Dynamic Factors for Spur and Helical Gears," Journal of Eng. for Ind., Trans. ASME, May 1970, pp. 504-515.

7. Ichimayu, K., and Hirano, I., "Dynamic Behavior of Heavy-Loaded Spur Gears," ASME Paper No. 72-PTG-14, 1972.

8. Ishikawa, J., Hayashi, K., and Yokoyana, M., "Surface Temperature and Scoring Resistance of Heavy-Duty Gears," ASME Paper No. 72-PTG-22, 1972.

9. "Lubrication of Gear Teeth," Engineering, Vol. 102, 1916, p. 109.

10. McEwen, E., "The Effect of Variation of Viscosity with Pressure on the Load Carrying Capacity of Oil Films Between Gear Teeth," Journal of Inst. Pet., Vol. 38, 1952, p. 646.

11. Daring, D. W., and Radzimovsky, E. I., "Lubricating Film Thickness and Load Capacity of Spur Gears: Analytical Investigation," ASME Paper No. 63-WA-85, 1963.

12. Adkins, R. W., and Radzimovsky, E. I., "Lubrication Phenomena in Spur Gears: Capacity, Film Thickness Variation and Efficiency," Journal of Basic Eng'g., Series D, Sept. 1965, pp. 655-665.

13. Radzimovsky, E. I., and Vathayanom, B., "Influence of the Tooth Surface Deformation upon the Capacity of Hydrodynamically Lubricated Spur Gears," ASME Paper No. 66-Lubs-12, 1966.

14. Dowson, D., and Higginson, G. R., "Elastohydrodynamic Lubrication - The Fundamentals of Roller and Gear Lubrication," Pergamon Press, London, 1966.

15. Gu, A., "Elastohydrodynamic Lubrication of Involute Gears," ASME Paper No. 72-PTG-34.

16. Blok, H., "Theoretical Study of Temperature Rise at Surfaces of Actual Contact Under Oiliness Lubricating Conditions," Proc. Gen. Disc. Lubrication, Inst. Mech. Engrs., Pt. 2, 1973, pp. 222-235.

17. Jaeger, J. C., "Moving Sources of Heat and Temperature at Sliding Contacts," Journal of Proc. Roy. Soc. N.S.W. 76, 1942, pp. 203-224.

18. Archard, J. F., "The Temperature of Rubbing Surfaces," Wear 2, 1958-59, pp. 438-455.

19. Cameron, A., Gordon, A. N., and Symm, G. T., "Contact Temperatures in Rolling Sliding Surfaces," Proceedings of Royal Society, A286, 1965, pp. 45-61.

20. Francis, H. A., "Interfacial Temperature Distribution within a Sliding Hertzian Contact," Trans. ASLE, Vol. 14, 1970, pp. 41-54.

21. Borsoff, V. N., "On the Mechanism of Gear Lubrication," Trans. ASME, Journal of Basic Eng'g., Vol. 80D, 1959, pp. 79-93.

22. Ku, P. M., and Baber, B. B., "The Effect of Lubricants on Gear Tooth Scuffing," ASLE Trans., Vol. 2, No. 2, Oct. 1959.

23. Neiman, G., Rettig, H., and Botsch, H., "The Effect of Different Lubricants on Pitting Resistance of Gears," Proceedings of Institution of Mechanical Engineers, Vol. 179, Pt. 3D, 1964-65, pp. 192-200.

24. Townsend, D. P., and Zaretsky, E. V., "A Life Study of AISIM-50 and Super Nitralloy Spur Gears With and Without Tip Relief," ASME Paper No. 73-Lub-30, 1973.

25. Dyson, A., "Frictional Traction and Lubricant Rheology in Elasto-hydrodynamic Lubrication," Philosophical Transactions of the Royal Society of London, Series A, Vol. 266, 1970, pp. 1-33.

26. Vichard, J. P., "Transient Affects in the Lubrication of Hertzian Contacts," Journal of Mech. Eng'g. Sci., Vol. 13, No. 3, 1971.

27. Attia, A. Y., "Deflection of Spur Gears Teeth Cut in Thin Rims," Journal of Eng'g for Ind., Nov. 1964, p. 333.

28. Chabert, G., Dan Tran, T., and Mathis, R., "An Evaluation of Stresses and Deflection of Spur Gear Teeth Under Strain," Journal of Eng'g for Ind., Feb. 1974, pp. 85-93.

29. Trachman, E. D., "The Rheological Effects on Friction in Elasto-hydrodynamic Lubrication," Ph.D. Thesis, Northwestern University, 1971.

30. Crook, A. W., "The Lubrication of Rollers, IV. Measurements of Friction and Effective Viscosity," Philosophical Transactions of the Royal Society of London, Series A, Vol. 255, 1963, pp. 281-312.

31. Smith, F. W., "Lubricant Behavior in Concentrated Contact - Some Rheological Problems," ASLE Transactions, Vol. 3, 1960, pp. 18-25.

32. Johnson, K. L.,and Cameron, R., "Shear Behavior of Elastohydrodynamic Oil Films at High Rolling Contact Pressure," Proc. of the Inst. of Mech. Eng'g., Vol. 182, Pt. 16, 1967, pp. 307-319.

33. Barlow, A. J., and Lamb, J., Matheson, A. J., Padmini, P. R. K. L., and Richter, J., "Viscoelastic Relaxation of Supercooled Liquids. I," Proc. of the Royal Soc. of London, Series A, Vol. 298, 1967, pp. 467-480.

34. Hutton, J. F., "Viscoelastic Relaxation Spectra of Lubricating Oils and Their Component Fractions," Proc. of the Royal Soc. of London, Series A, Vol. 304, 1968, pp. 65-80.

35. Plint, M. A., "Traction in Elastohydrodynamic Contacts," Proc. of the Inst. of Mech. Eng'g., Vol. 182, Pt. 1, 1967, pp. 300-306.

36. Cheng, H. S., "Calculation of Elastohydrodynamic Film Thickness in High Speed Rolling and Sliding Contacts," Mechanical Technology Inc., Technical Report 67TR24.

37. Kanwal, R. P., "Linear Integral Equations," Academic Press, 1971.

38. Zienkiewicz, O. C., "The Finite Method in Engineering Science," McGraw-Hill, 1972.

1. Report No. NASA CR-3241	2. Government Accession No.	3. Recipient's Catalog No.
4. Title and Subtitle THERMAL ELASTOHYDRODYNAMIC LUBRICATION OF SPUR GEARS		5. Report Date February 1980
		6. Performing Organization Code
7. Author(s) K. L. Wang and H. S. Cheng		8. Performing Organization Report No. None
		10. Work Unit No.
9. Performing Organization Name and Address Northwestern University Evanston, Illinois 60201		
		11. Contract or Grant No. NGR 14-007-084
		13. Type of Report and Period Covered Contractor Report
12. Sponsoring Agency Name and Address National Aeronautics and Space Administration Washington, D.C. 20546		
		14. Sponsoring Agency Code

15. Supplementary Notes

16. Abstract

An analysis and computer program called TELSGE were developed to predict the variations of dynamic load, surface temperature, and lubricant film thickness along the contacting path during the engagement of a pair of involute spur gears. The analysis of dynamic load includes the effect of gear inertia, the effect of load sharing of adjacent teeth, and the effect of variable tooth stiffnesses which are obtained by a finite-element method. Results obtained from TELSGE for the dynamic load distributions along the contacting path for various speeds of a pair of test gears show patterns similar to that observed experimentally. Effects of damping ratio, contact ratio, tip relief, and tooth error on the dynamic load were examined. In addition, two dimensionless charts are included for predicting the maximum equilibrium surface temperature, which can be used to estimate directly the lubricant film thickness based on well established EHD analysis.

17. Key Words (Suggested by Author(s)) Gears; Spur gears; Analysis; Temperature; Dynamic load	18. Distribution Statement Unclassified - unlimited STAR Category 37	
19. Security Classif. (of this report) Unclassified	20. Security Classif. (of this page) Unclassified	21. No. of Pages 135	22. Price* A07